AD-A128 986 ADAPTIVE TECHNIQUES TO CORRECT FOR EFFECTS OF IONOSPHERIC REFRACTION IN N..(U) REGIS COLL RESEARCH CENTER WESTON MA M LEE ET AL. 03 FEB 83 1/1

UNCLASSIFIED AFGL-TR-83-0051 F19628-80-C-0016 F/G 12/1 NL

END

FILMED

DTIC

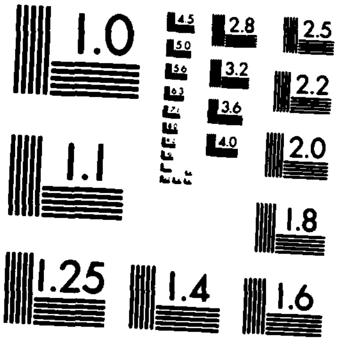

MICROCOPY RESOLUTION TEST CHART
NATIONAL BUREAU OF STANDARDS-1963-A

(12)

AFGL-TR-83-0051

ADAPTIVE TECHNIQUES TO CORRECT FOR EFFECTS OF IONOSPHERIC REFRACTION IN NAVIGATION, SURVEILLANCE AND COMMUNICATION SYSTEMS

Min-Chang Lee
D. E. Donatelli

Regis College Research Center
235 Wellesley Street
Weston, MA. 02193

Final Report
1 February 1980 - 31 January 1983

3 February 1983

Approved for public release; distribution unlimited

AIR FORCE GEOPHYSICS LABORATORY
AIR FORCE SYSTEMS COMMAND
UNITED STATES AIR FORCE
HANSCOM AFB, MASSACHUSETTS 01731

Unclassified

SECURITY CLASSIFICATION OF THIS PAGE (*When Data Entered*)

REPORT DOCUMENTATION PAGE

READ INSTRUCTIONS BEFORE COMPLETING FORM

1. REPORT NUMBER AFGL-TR-83-0051	2. GOVT ACCESSION NO. A128986	3. RECIPIENT'S CATALOG NUMBER
4. TITLE (*and Subtitle*) Adaptive Techniques to Correct for Effects of Ionospheric Refraction in Navigation, Surveillance and Communication Systems.		5. TYPE OF REPORT & PERIOD COVERED Final report 1 Feb 1980 - 31 Jan 1983
		6. PERFORMING ORG. REPORT NUMBER
7. AUTHOR(*s*) Min-Chang Lee, D.E.Donatelli		8. CONTRACT OR GRANT NUMBER(*s*) F19628-80-C-0016
9. PERFORMING ORGANIZATION NAME AND ADDRESS Regis College Research Center 235 Wellesley Street Weston, MA., 02193		10. PROGRAM ELEMENT, PROJECT, TASK AREA & WORK UNIT NUMBERS 62101F 464304CD
11. CONTROLLING OFFICE NAME AND ADDRESS Air Force Geophysics Laboratory Hanscom AFB, MA 01731 Contract Monitor: John A. Klobuchar/PHY		12. REPORT DATE 03 Feb 1983
		13. NUMBER OF PAGES 66
14. MONITORING AGENCY NAME & ADDRESS(*if different from Controlling Office*)		15. SECURITY CLASS. (*of this report*) Unclassified
		15a. DECLASSIFICATION/DOWNGRADING SCHEDULE

16. DISTRIBUTION STATEMENT (*of this Report*)

Approved for public release; distribution unlimited.

17. DISTRIBUTION STATEMENT (*of the abstract entered in Block 20, if different from Report*)

18. SUPPLEMENTARY NOTES

19. KEY WORDS (*Continue on reverse side if necessary and identify by block number*)

Ionospheric variability, Time delay, Range error, Multiplicative and additive prediction functions, Total electron contents (TEC), Ion lines, Plasma lines, Upper hybrid modes, Field-aligned ionospheric irregularities, Parametric instabilities, Beating current at zero frequency, Differential Ohmic heating, Ponderomotive force, Nonlinear Lorentz force, Faraday polarization fluctuations

20. ABSTRACT (*Continue on reverse side if necessary and identify by block number*)

The following research work has been ~~attacked:~~ performed: (1) adaptive procedures to correct ionospheric variability in time delay and range error measurements of radio waves (2) seasonal and diurnal studies of total electron contents (TEC) at Ascension Island (3) effects of ionospheric modification caused by high power, HF radio waves (4) Faraday polarization fluctuations (FPF) of satellite signals in transionospheric propagation. Multiplicative and additive prediction functions are used as adaptive procedures to estimate and compare their effectiveness in correcting ionospheric variability in time delay and range

DD FORM 1 JAN 73 1473 EDITION OF 1 NOV 65 IS OBSOLETE

Unclassified

SECURITY CLASSIFICATION OF THIS PAGE (*When Data Entered*)

19. Key words (continued)
(FPF), Transionospheric propagation, Phase shift, Birefringent medium, power-law type and gaussian type of ionospheric irregularities, Single and multiple-scattering processes.

20 Abstract (continued)
error measurements of radio waves. Post-sunset TEC enhancement and sudden sharp changes in the TEC are the two striking characteristic features of the night-time ionosphere at Ascension Island. Some nonlinear phenomena, caused by powerful, HF radio waves in the ionosphere, are analyzed theoretically, such as ion line enhancement, the excitation of upper hybrid modes or field-aligned plasma lines, and field-aligned non-oscillatory ionospheric irregularities. A mechanism has been proposed to explain the FPF of satellite signals in HF and VHF bands in their trans-ionospheric propagation.

Accession For
NTIS GRA&I ☑
DTIC TAB ☐
Unannounced ☐
Justification

By
Distribution/
Availability Codes

Dist	Avail and/or Special
A	

Table of Contents

Outline of the Final Report

The research work, which has been accomplished at the Regis College Research Center for AFGL contract F19628-80-C-0016, includes (1) adaptive procedures to correct ionospheric variability in time delay and range error measurements of radio waves (2) seasonal and diurnal studies of total electron contents (TEC) at Ascension Island (3) effects of ionospheric modification caused by high power, HF radio waves (4) Faraday polarization fluctuations (FPF) of satellite signals in transionospheric propagation.

Multiplicative and additive prediction functions are used as adaptive procedures to correct ionospheric variability in time delay and range error measurements of radio waves. The adaptive algorithms employ real time measurements to reduce rms errors in ionospheric predictions. It is found that significant reductions in rms errors are achieved in daytime, at solar maximum, when time delay and range errors are greatest, using a multiplicative prediction function.

TEC data recorded at Ascension Island from September 22,1978 through December 21,1980 have been analyzed, displaying two characteristic features of the night-time ionosphere. They are (1) a post-sunset enhancement which lasts for several hours, and follows a rapid decrease unattributable to the usual ionospheric decay processes, and (2) the sudden sharp changes in the TEC along the ray path of satellite signals, that are often superimposed on those enhancements and, to a lesser degree, on the subsequent normal night-time ionosphere. F layer dynamo theory and generation of ionospheric bubbles are invoked to interpret these observations.

Many unexpected, nonlinear plasma processes can be triggered in the ionosphere by a powerful, HF radio wave near the F peak. Selected for studies are the following: ion line enhancement, the excitation of upper hybrid modes or field-aligned plasma lines, and the induced field-aligned ionospheric irregularities with a broad scale-length range. Various parametric instabilities are responsible for these phenomena. Beating current at zero frequency is also an important nonlinearity in producing field-aligned high-frequency modes (upper hybrid waves) and large-scale non-oscillatory modes (irregularities) in addition to the differential Ohmic heating force and the nonlinear Lorentz force. In the analysis of non-oscillatory modes, it is more reasonable to employ four-wave than to use three-wave interaction process. A criterion has been established, allowing the excitation of upper hybrid waves by radio waves with ordinary rather than extraordinary polarization. Ionospheric inhomogeneity can be shown to impede generally the excitation of plasma instabilities and consequently suppress the growth of the induced ionospheric irregularities. The thresholds of various parametric instabilities concerned are rather low as compared to the power typically used in the ionospheric heating experiments.

Faraday polarization fluctuations (FPF) of beacon satellite signals origin in the differential phase shift and the differential changes in logarithmic amplitudes of ordinary and extraordinary modes when a linearly polarized radio wave propagates in a birefringent medium (i.e., the ionosphere). FPF has been observed for signals transmitted from either low-flying orbitting satellites or geostationary satellites in the HF and VHF bands. Ionospheric irregularities are identified to be the scatterers of satellite signals in trans-ionospheric propagation, that lead to the FPF. Ionospheric irregularities of power-law type and quasi-Gaussian type correspond respectively to the early phase and the late phase of ionospheric disturbances. It is shown that power-law type irregularities can cause the FPF of satellite signals with frequencies up to, approximately, 250 MHz under the typical ionospheric conditions at Ascension Island. In contrast, Gaussian type irregularities can only effect the HF satellite signals, e.g., 20 MHz. Although the saturation of amplitude scintillation of radio waves is due to the multi-scattering process, it is accurate enough to use the single-scattering process to describe the physics of FPF even in the VHF band.

Radio Science, Volume 16, Number 2, pages 261-269, March-April 1981

Time cells for adaptive prediction of total electron content

D. E. Donatelli

Regis College Research Center, Weston, Massachusetts 02193

R. S. Allen

Air Force Geophysics Laboratory, Hanscom Air Force Base, Massachusetts 01731

(Received March 20, 1980; revised October 2, 1980; accepted October 6, 1980.)

Adaptive procedures, using multiplicative and additive prediction functions of the standard deviation of the observations, are analyzed to estimate and compare their effectiveness in correcting for ionospheric variability in time delay and range measurements. The adaptive algorithms use real time measurements to reduce rms errors in ionospheric predictions. Total electron content data from Hamilton, Massachusetts, for 1969-1976 are used to evaluate diurnal, seasonal, and solar cycle impact on radar, navigation, and communication systems. Time cells are defined from the growth rate of rms residual error. Significant reductions in rms error are achieved in daytime, at solar maximum, when time delay and range errors are greatest, using a multiplicative prediction function.

INTRODUCTION

The potential precision of radar, navigation, and communication systems may be increased through advances in device technology, but daily variability of the ionosphere continues to be a constraint on achievable system performance. Numerical maps that provide monthly median correction for ionospheric effects have been derived from a worldwide climatology of ionospheric parameters; their use alone reduces the monthly rms residual error to about 20-25% of the median correction in daytime and 30-35% at night [*DuLong*, 1977]. Many precision systems cannot tolerate the individual departures of 50-200% that are averaged away in monthly statistics. For these systems, adaptive prediction algorithms are presented using field measurements to provide real time correction of ionospheric effects.

The local ionosphere in a system coverage area may be monitored through measurements of ionospheric parameters, such as the critical frequency of the F region ($fOF2$), total electron contect (TEC), the gradient in the lower F region, or through measurements derived from the system itself. Since some system users may not have the capability of implementing the computer models based on worldwide climatology, they may use locally monitored TEC or $fOF2$ to estimate monthly median behavior and short-term persistence effects by producing means of several days to predict the subsequent hourly, daily, and weekly response of their system to the current state of the ionosphere.

Adaptive prediction algorithms have been examined using $fOF2$ data [*Wilkinson*, 1979] and TEC data [*Donatelli and Allen*, 1978; *Leitinger et al.*, 1978; *Donatelli and Allen*, 1979]. These include TEC as derived from measurements of Doppler shift using passes of the Navy Navigation Satellites (NNSS) and from Faraday rotation measurements using VHF beacons from geostationary satellites. The procedures apply to any type of synoptic data, and rely on a reasonable prediction of the monthly mean of the observations, the standard deviation, and an assumption on the correlation of the observations in the time cell being considered. Two basic approaches will be comparatively analyzed: the first is a multiplicative prediction function, and the second, an additive prediction function. The second approach has been analyzed in detail by *Gautier and Zacharisen* [1965] with respect to $fOF2$ data and by *DaRosa* [1974] with respect to TEC. An evaluation of an adaptive procedure using a multiplicative function to update a monthly mean refraction correction with real time measurements of TEC is presented here. The temporal growth of the rms residual error, within a time cell extending

Paper number 80S1420.
0048-6604/81/0304-1420$01.00

from a reference time with residual error defined as zero, to an upper limit defined to lie within the error budget of a particular system, is examined.

The ionospheric time delay of a radio wave is directly proportional to the electron content along the ray path, such that the results presented here in TEC may be translated by the user to system parameters as follows:

Time delay [*Davies*, 1966]:

$$\Delta T = \frac{40.3}{cf^2} \times \text{TEC} \quad \text{(sec)}$$

Range error:

$$\Delta R = c\Delta T = \frac{40.3}{f^2} \times \text{TEC} \quad \text{(m)}$$

where f is the frequency of the radio signal in megahertz, c is the speed of light in a vacuum in meters per second, and TEC is in units of electrons per square meter times 10^{16}.

ANALYSIS

The basis for the procedure is the assumption that major components of daily variability in the ionosphere can be described as large-scale, large-magnitude, slowly varying fluctuations and are, therefore, reasonably correlated in time. These fluctuations result from daily variables such as solar activity, magnetic activity, lunar tides, neutral winds that could produce multiplicative or additive effects on the ionosphere. The rms error using the adaptive procedure is

$$\chi_t^2 = \frac{\Sigma(O_t - P_t)^2}{N} \tag{1}$$

by expanding

$$\chi_t^2 = \sigma_t^2 + \mu_t^2 + \frac{\Sigma}{N}(P_t^2 - 2O_tP_t)$$

where O_t is the observation at the time when the correction is applied, P_t is the prediction at the time of correction using the observation from the reference time, σ_t is the standard deviation of the observations:

$$\sigma_t^2 = (\Sigma/N)(O_t - \mu_t)^2 = \frac{\Sigma}{N}O_t^2 - \mu_t^2$$

N is the number of observations, and t is the time of the applied correction. The predicted value is defined by the function being considered, i.e.,

Case 1, multiplicative function:

$$P_t = a_1 \frac{O_{t_0}}{\mu_{t_0}} \mu_t \tag{2a}$$

Case 2, additive function:

$$P_t = \mu_t + a_2(O_{t_0} - \mu_{t_0}) \tag{2b}$$

where μ is the observed mean, t_0 is the reference time, and a_1 and a_2 are constants to be determined. Substituting for P_t in (1), the residual error is:

Case 1:

$$\chi_t^2 = \sigma_t^2 + \mu_t^2 + a_1^2 \frac{\mu_t^2}{\mu_{t_0}^2}(\sigma_{t_0}^2 + \mu_{t_0}^2)$$

$$- 2a_1 \frac{\mu_t}{\mu_{t_0}}(\sigma_t\sigma_{t_0}\rho_t + \mu_t\mu_{t_0}) \tag{3a}$$

Case 2:

$$\chi_t^2 = \sigma_t^2 + a_2^2\sigma_{t_0}^2 - 2a_2\sigma_t\sigma_{t_0}\rho_t \tag{3b}$$

where ρ_t is the correlation coefficient:

$$\rho_t = \frac{\Sigma(O_t - \mu_t)(O_{t_0} - \mu_{t_0})}{(\Sigma(O_t - \mu_t)^2\Sigma(O_{t_0} - \mu_{t_0})^2)^{1/2}}$$

$$= \frac{\mu_t\mu_{t_0}}{\sigma_t\sigma_{t_0}}\left(\frac{\Sigma O_tO_{t_0}}{N\mu_t\mu_{t_0}} - 1\right)$$

Differentiating χ_t with respect to a_1 and a_2, setting equal to zero, and solving for a_1 and a_2

Case 1:

$$a_1 = \frac{\sigma_t^2\alpha_t\rho_t + \mu_t^2}{\sigma_t^2\alpha_t^2 + \mu_t^2}$$

Case 2:

$$a_2 = \frac{\rho_t}{\beta_t}$$

where α_t and β_t are defined as

$$\alpha_t = \frac{\sigma_{t_0}}{\mu_{t_0}}\frac{\mu_t}{\sigma_t}$$

$$\beta_t = \frac{\sigma_{t_0}}{\sigma_t}$$

By substituting for a_1 and a_2 in (3a) and (3b), respectively, the minima for χ_t are obtained:

Case 1:

$$\chi_t^2 = \sigma_t^2 \left\{ 1 - \rho_t^2 + \frac{\mu_t^2(\alpha_t - \rho_t)^2}{\sigma_t^2 \alpha_t^2 + \mu_t^2} \right\} \qquad (4a)$$

Case 2:

$$\chi_t^2 = \sigma_t^2(1 - \rho_t^2) \qquad (4b)$$

Equation (4*b*) is the result obtained by *Gautier and Zacharisen* [1965]. Equation (4*a*) reduces to (4*b*) if $\alpha_t = \rho_t$.

To reduce the average monthly residual error such that $\chi_t \leq c\sigma_t$, where c is the degree of reduction desired, the implied condition for case . is:

$$1 - \rho_t^2 + (\alpha_t - \rho_t)^2 \left(\frac{\mu_{t_0}^2}{\sigma_{t_0}^2 + \mu_{t_0}^2} \right) \leq c^2 \qquad (5a)$$

which, for $\alpha_t = \rho_t$, reduces to the condition for case 2:

$$1 - \rho_t^2 \leq c^2 \qquad (5b)$$

If $\alpha_t \neq \rho_t$, the quality of the prediction degrades proportional to the difference between α_t and ρ_t.

To minimize the error, the correlation coefficient must be known. If ρ_t is not known, a_1 and a_2 cannot be defined. Therefore, to provide an operational definition for P_t, a_1 and a_2 in (2*a*) and (2*b*) are arbitrarily set equal to one. Then (3*a*) and (3*b*) can be written as

Case 1:

$$\chi_t^2 = \sigma_t^2 [1 - \rho_t^2 + (\alpha_t - \rho_t)^2] \qquad (6a)$$

Case 2:

$$\chi_t^2 = \sigma_t^2 [1 - \rho_t^2 + (\beta_t - \rho_t)^2] \qquad (6b)$$

Comparing (6*a*) with (4*a*) and (6*b*) with (4*b*) it is seen that in case 1, χ_t^2 increases by elimination of the factor $(\mu_{t_0}^2)/(\sigma_{t_0}^2 + \mu_{t_0}^2)$ in the third term of (4*a*), and case 2 increases by addition of a third term, $(\beta_t - \rho_t)^2$. The limiting condition for case 1 is

$$1 - \rho_t^2 + (\alpha_t - \rho_t)^2 \leq c^2 \qquad (7)$$

which defines limits for α_t and ρ_t:

$$\alpha_t \leq \rho_t \pm [\rho_t^2 - (1 - c^2)]^{1/2} \qquad (8)$$

Since α_t is always real and positive, the condition $\rho_t^2 \geq 1 - c^2 \geq 0$ must always be satisfied. By definition, $c \leq 1$; therefore $0 < \alpha_t < 2\rho_t$. (The analysis for case 2 is identical to case 1 with β_t substituted for α_t.) For example, if $c = 0.5$, which implied a 50% reduction in residual error, $\rho_t \geq 0.866$ is required. However, if $\rho_t = 0.5$, a reduction in residual error of more than 10% is possible if $\alpha_t(\beta_t) \approx \rho_t$.

The TEC data used to evaluate this procedure were reduced from measurements of the Faraday rotation of signals from the beacon of the ATS 3 geostationary satellite observed at Hamilton, Massachusetts, during the 1969–1976 period covering the maximum and minimum of the last solar cycle. The location of the 420-km subionosphere point [*Titheridge,* 1972] along the ray path from Hamilton is 39°N, 289°E. These data provide a basis for evaluation of average solar cycle behavior, since this solar cycle closely approximates the average of the past 20 solar cycles with $\bar{R}_z = 100$, $\bar{S} = 155$ at maximum, and $\bar{R}_z = 10$, $\bar{S} = 71$ at minimum, where $\bar{R}_z$ and $\bar{S}$ are the 12-month running mean sunspot number and solar flux at 2800 Mhz, respectively. To estimate TEC for other values of $\bar{R}_z$ (or $\bar{S}$), it is possible to interpolate to a reasonable approximation by assuming a linear relationship between $\bar{R}_z$ (or $\bar{S}$) and TEC [*DuLong,* 1977].

By using the definition of α_t and setting $\rho_t = 1$, the potential of an adaptive procedure using a

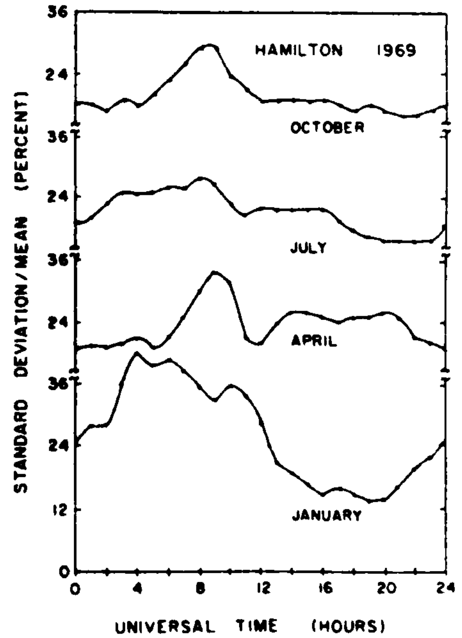

Fig. 1. Diurnal curves of percentage standard deviation in TEC for the months of January, April, July, and October 1969 at Hamilton, Massachusetts.

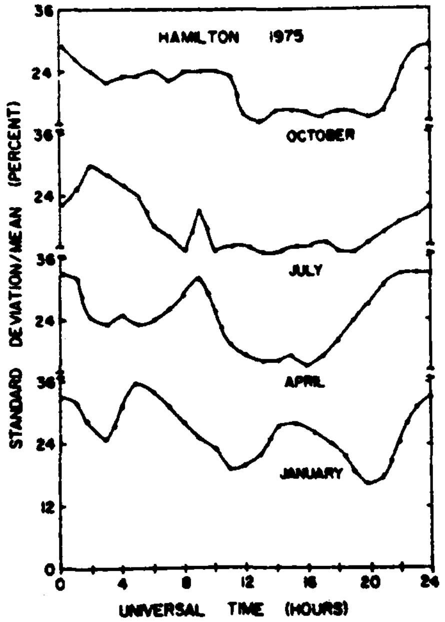

Fig. 2. Same as for Figure 1 but for 1975.

multiplicative function can be estimated with knowledge of the percentage standard deviation for the reference time and the time of applied correction (6*a*). This percentage was calculated for each month of data and is shown in Figures 1 and 2 for the months of January, April, July, and October 1969 and 1975, respectively, representing diurnal, seasonal, and solar cycle effects.

The growth of the percentage error in time at any location may be estimated by taking progressive ratios along the curve from some choice of reference time on that curve. When $\alpha_t = c$, the limit of a time cell is defined, since the residual error will then equal the monthly mean error.

One of the limitations on time cell extent, apparent from these curves, is that large errors may be generated when a scaling factor from nighttime is used across the sunrise terminator to adapt daytime predictions. This has a greater effect at solar minimum, since the percentage variability fluctuates more radically at this time, a reflection of the lower mean values at solar minimum where a small absolute variation in TEC will produce a large percentage variation, particularly at nighttime. In general, extended time cells are possible at solar maximum but must be greatly reduced at solar minimum. However, the remaining variability in TEC units ((electrons/m^2) × 10^{16}), χ_t, is still less at solar minimum.

When an additive function is considered, the potential of the adaptive technique may be estimated using Figures 3 and 4. These are the curves for the standard deviation in TEC units corresponding to the percentage curves of Figures 1 and 2. Again, the process is considered for $\rho = 1$, where the error χ_t is defined by (6*b*), and is estimated in TEC units by taking ratios between points, analogous to Figures 1 and 2. From these figures it appears that additive functions may well describe nighttime and solar minimum conditions but would be less descriptive of daytime conditions at solar maximum.

RESULTS

Since the ionospheric impact on systems is most severe in daytime, at solar maximum, the adaptive procedure applying a multiplicative function is examined using the assumption that within the data base the correlation is expected to monotonically decrease to zero with time, and negative correlation is not considered. The procedure is initiated by obtaining a measurement of TEC at reference time O_{t_0}, determining a scaling factor from the ratio

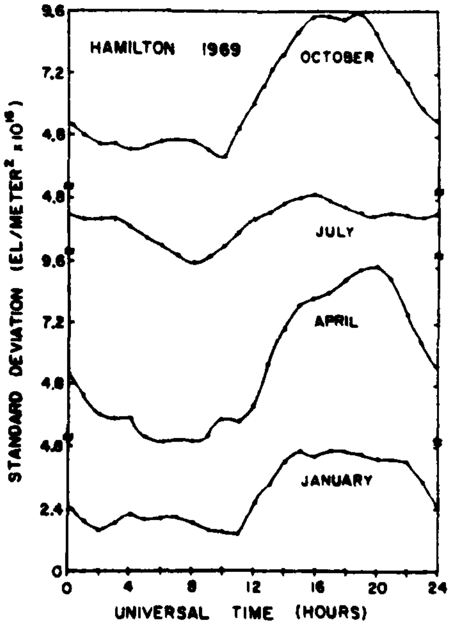

Fig. 3. Diurnal curves of standard deviation in TEC for the months of January, April, July, and October 1969 at Hamilton, Massachusetts.

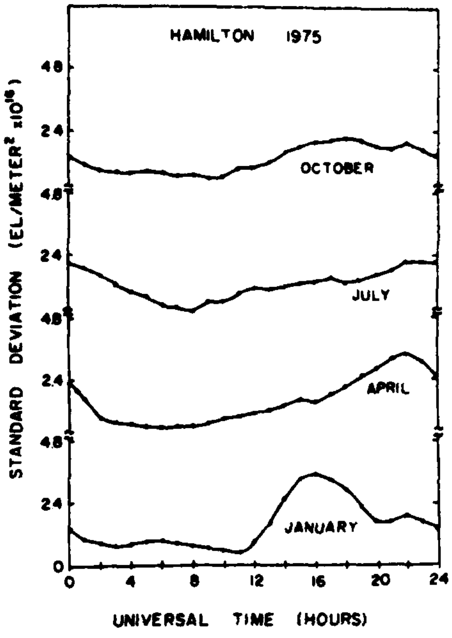

Fig. 4. Same as for Figure 3 but for 1975.

of the observation to the baseline prediction for the reference point M_{t_0} and scaling the baseline map for a succeeding time period. The adapted prediction P_t at a later time is then $P_t = (O_{t_0}/M_{t_0})M_t$, where M_t is the baseline prediction at the later time. As noted previously, the actual monthly mean is used for the baseline prediction to remove any model dependent error from the ensuing results. Thus from case 1, $P_t = (O_{t_0}/\mu_{t_0})\mu_t$.

The TEC data are reduced at 15-min intervals. The adapted prediction is applied at these intervals over several hours. Comparisons are made with the corresponding observations and the rms error χ_t is computed each month at each 15-min increment from the same reference times each day. The results for January 1969 are presented in Figure 5, including a comparison of results using the actual monthly mean, Figure (5*a*), and a model predicted mean based on ionospheric climatology [*Barghausen et al.*, 1969], Figure 5*b*. The outer scale on the figures is the mean and is 4 times greater than the inner scale, which is the standard deviation with respect to the mean and the rms error of the adapted prediction with respect to the observations. Although there is up to 20% difference between the predicted and the observed mean, the standard deviation with respect to each mean is comparable, indicating that without adaption, the monthly climatology prediction is as useful as the mean itself.

The growth of the rms error of the adapted prediction χ_t is described by the thin lines originating at 2-hr intervals, with $\chi_t = 0$. In (5*a*), χ_t extends in time from $t = t_0$ to $t = t_0 + 3$ hr; in (5*b*), from $t = t_0$ to $t = t_0 + 12$ hrs. The scaling factor has been determined by the observation at $t = t_0$ and held constant over the 3- and 12-hr time cell; only the scaling of the mean μ_t and the predicted mean M_t is progressed with time (Figures 5*a* and 5*b*, respectively).

The dashed lines define the residual error for a 3-hr time cell (χ_{t_0+3h}) and indicate that a scaling factor that is 3 hr old is useful throughout the daytime hours, unless it was determined prior to sunrise and used thereafter. The difference between χ_{t_0+3h} in (5*a*) and (5*b*) is the model dependent error, most evident in the sunrise area. Comparing these curves with the standard deviation of the observed σ_t and predicted mean S_t, it is apparent that the time cell in which the adapted prediction is useful is bound by the reference time on one end and the succeeding solar terminator on the other.

An analysis of χ_t for case 1, showing the effect of the model bias, can be found in appendix A; *Gautier and Zacharisen* [1965] have presented an equivalent analysis for case 2. It has been assumed that the data follows a normal distribution. In reality, however, it is somewhat skewed toward higher values in daytime, such that a model that predicts a slightly greater mean than that observed will often succeed in reducing the monthly variance at that time.

The performance of this adaptive technique is summarized in Table 1 using the archive data of TEC from Hamilton, Massachusetts, for 1969 through 1976. The daytime and nighttime maxima of the mean, standard deviation, and three time cells, averaged over season, at both solar maximum and minimum, in TEC units, (electrons/m²) × 10^{16}, are compared. The table shows that an adapted prediction can reduce the residual error, on average, by 60% in a 1-hr time cell and still as much as 30% in a 3-hr time cell for daytime solar maximum. Detailed results may be found in *DuLong* [1977].

The time cell is theoretically determined by the correlation time of fluctuations in TEC. Since the basic data for this study were reduced at 15-min intervals, fluctuations with periods less than 30 min are not observable. Their amplitude is assumed to

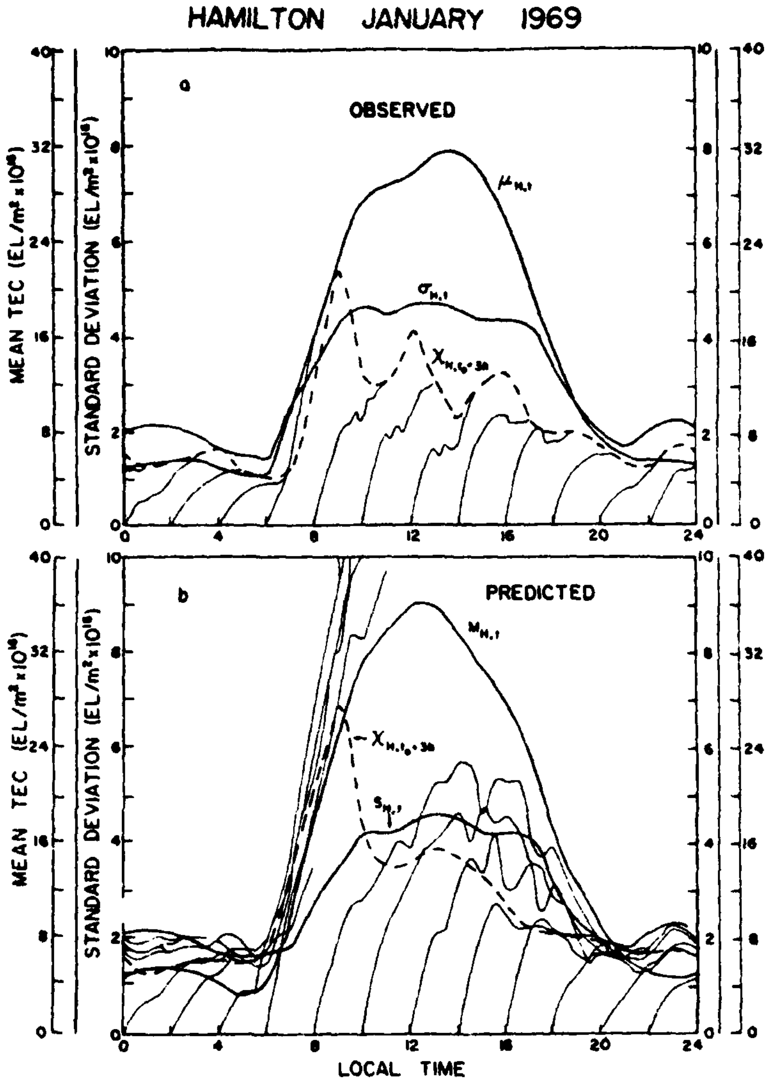

Fig. 5. (*a*) Comparison in TEC for January 1969 at Hamilton, Massachusetts, of the observed mean, standard deviation, rms error of a 3-hr time cell, and error growth in time using an adapted prediction up to 3 hrs after a reference time. (*b*) Similar to 5*a* but using a model prediction of mean TEC. The error growth in time using the adapted prediction is shown for 12 hr after the reference time.

be much smaller than the longer-period variations that are being tracked here. The present simple adaptive technique, predicting a persistence of 15 min to 3 hr, tends to mitigate against just those long-period TEC variations, which seem to be a major component at solar maximum, with a residual of the same absolute magnitude as the residual at solar minimum. This suggests that short-period variations of TEC predominate at solar minimum and are still present with comparable amplitude at solar maximum, masked by the characteristic larger-scale variations.

During sunrise and sunset periods, the effects of production and loss create gradients that dominate all other fluctuations. Similar gradients occur during magnetic disturbance, particularly in the region of the auroral zone and the trough in high and mid-latitudes. The rate at which these changes occur should determine the time cells for these periods. This is illustrated in Figure 6. In Figure

TABLE I. Summary of effectiveness of various time cells in reducing prediction error.

	Winter		Vernal Equinox		Summer		Autumnal Equinox	
	Day	Night	Day	Night	Day	Night	Day	Night
			Solar Maximum ($\bar{R}_z$ = 110; $\bar{S}$ = 155)					
μ_t	34.4	5.7	44.8	8.2	25.4	8.2	41.1	6.7
σ_t	6.0	1.8	7.8	2.5	4.0	2.2	7.8	2.2
χ_{t_0+3h}	4.0	1.5	4.5	1.5	2.7	1.5	4.0	1.8
χ_{t_0+1h}	2.2	1.0	2.5	1.0	1.6	1.2	1.6	0.7
χ_{t_0+30m}	1.5	0.6	1.5	0.6	1.2	0.6	1.3	0.6
			Solar Minimum ($\bar{R}_z$ = 10; $\bar{S}$ = 71)					
μ_t	10.5	1.5	10.5	1.5	9.0	2.1	11.2	2.1
σ_t	1.8	0.6	2.5	0.6	1.5	0.5	1.5	0.6
χ_{t_0+3h}	1.8	0.9	2.1	0.5	1.5	0.5	2.1	0.6
χ_{t_0+1h}	1.2	0.3	1.2	0.1	0.6	0.3	1.2	0.3
χ_{t_0+30m}	0.9	0.1	0.6	0.1	0.4	0.1	0.6	0.1

Symbols represent the following, in TEC units: μ_t, the mean value of TEC; σ_t, the rms deviation of TEC from the mean, representing day-to-day variability of the ionosphere; χ_{t_0+3h}, the residual error using an adapted prediction in a 3-hr time cell; χ_{t_0+1h}, the residual error using an adapted prediction in a 1-hr time cell; χ_{t_0+30m}, the residual error using an adapted prediction in a 30-min time cell.

(6*a*) the observed TEC for the day O_t is compared with the prediction for the month μ_t and the adapted prediction for a 30-min time cell, P_{t_0+30m} and a 3-hr time cell, P_{t_0+3h}. The difference between the observed TEC and the predictions in each case are shown in Figure (6*b*). The error using the 3-hr time cell $|O_{t_0+3h} - P_{t_0+3h}|$ is equivalent in magnitude to that using the monthly mean $|O_t - \mu_t|$, but large excursions have been introduced at time periods when they would otherwise not exist. The adapted prediction using a 30-min time cell, P_{t_0+30m}, provides a 60% reduction in the maximum error despite the steep gradients in TEC on this disturbed day.

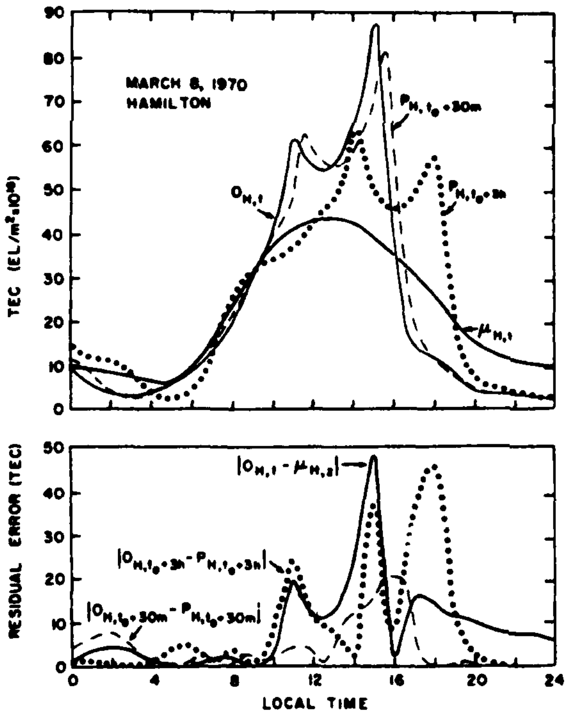

Fig. 6. (*a*) TEC on a magnetically disturbed day compared to the observed TEC, the mean, and the adapted predictions for the day using 30-min and 3-hr time cells. (*b*) Residual error in TEC using the predictions of 6*a* for the day.

CONCLUSION

When using adapted predictions, it must first be determined whether the dominant features are described by additive or multiplicative functions. For instance, for a system propagating through the auroral region, large changes of TEC related to precipitating particles may be dominant sources of error that are best treated as additions to a background ionosphere, whereas for a system at midlatitude, large changes of TEC related to changes in neutral composition might best be treated as a multiple of the expected ionosphere. From this analysis it was shown that the rms error using an additive function is dependent on the absolute difference in the standard deviation of the two points under consideration. For the multiplicative function the absolute difference in percentage standard deviation with respect to the mean is the relevant parameter. Examination of these parameters indicated that for the solar maximum period, when the ionospheric impact on systems is most severe, multiplicative functions best describe the dominant features. An evaluation for an adaptive procedure that corrects for these features has been presented. The procedure is successful if the condition $1 \geq \rho_t > (\alpha_t/2) \geq 0$ exists, where ρ_t is the correlative coefficient at the time of applied correction and α_t is the ratio of the percentage rms deviation at the reference time to that at the time of applied correction.

In daytime an improvement of 50% is readily achievable, at solar maximum within a 3-hr time cell and at solar minimum within a 1-hr time cell. At nighttime, the percentage rms deviation is usually greater than daytime, but the absolute deviation is less; therefore the need for correction is not as critical. However, if adapted predictions are used, a scaling factor obtained at nighttime should not be projected across the sunrise terminator, as the rapid change in percentage rms deviation during the sunrise growth period introduces errors. The sunset decay period is less critical, since the percentage deviation usually increases at nighttime. This implies that α_t would then decrease, allowing a greater range for ρ_t, thereby increasing the probability that the requirement $\rho_t > (\alpha_t/2)$ will be met.

It is seen that time cells with an extent of several hours are operationally useful at solar maximum. At solar minimum the absolute value of the rms deviation is low; therefore the need for correction is again less critical. For example, the residual error, using a 1-hr time cell at solar maximum, is equivalent to the average monthly variance at solar minimum, indicating the adaptive procedure succeeds in reducing the error at solar maximum to the lower impact solar minimum levels.

APPENDIX A

For actual system use, the monthly mean ionospheric behavior would be predicted by a numerical model derived from worldwide climatology. Any model has some inherent bias, which may have little consequence on rms error when the primary concern is predicting the mean behavior; but, as shown in Figure 5(b), this bias can affect the adaptive procedure. The following derivation will provide some perspective on the import of this bias.

The rms error is defined as

$$\chi_t^2 = \frac{\Sigma}{N}(O_t - P_t)^2 \tag{A1}$$

where P_t is the prediction of the adaptive procedure. For the case of a multiplicative function

$$P_t = \frac{O_{t_0}}{M_{t_0}} M_t \tag{A2}$$

where M is the mean as predicted by the model and the subscripts t_0 and t denote the reference time and the time of applied correction, respectively. Substituted in (A1) and expanded in terms of σ_t, σ_{t_0} and ρ_t, then

$$\chi_t^2 = \sigma_t^2 + \mu_t^2 + \frac{M_t^2}{M_{t_0}^2}(\sigma_{t_0}^2 + \mu_{t_0}^2) - 2\frac{M_t}{M_{t_0}}(\sigma_t \sigma_{t_0} \rho_t + \mu_{t_0} \mu_t) \tag{A3}$$

Now defining the model bias B such that

$$B_{t_0} = \frac{M_{t_0}}{\mu_{t_0}}$$

$$B_t = \frac{M_t}{\mu_t}$$

and substituting B_{t_0} and B_t, the results analogous to (6) are

$$\chi_t^2 = \sigma_t^2 \left\{ 1 - \rho_t^2 + \left(\frac{B_t}{B_{t_0}} \alpha_t - \rho_t \right)^2 \right\} + \mu_t^2 \left(1 - \frac{B_t}{B_{t_0}} \right)^2 \tag{A4}$$

It can be seen immediately that if $B_t = B_{t_0}$, that is, if the model bias does not vary between the times being considered, use of the model will be as effective as the use of the observed mean in the adaptive procedure. However, empirical models are biased by their data base, implying preferred times when the bias is less variable, and therefore of less importance.

Acknowledgments. The author would like to thank J. Klobuchar of the Air Force Geophysics Laboratory for the use of the TEC data. This work was supported by U.S. Air Force contract F19628-76-C-0255.

REFERENCES

Barghausen, A. F., J. W. Finney, L. L. Proctor, and L. D. Schultz (1969), Predicting long-term operational parameters of high-frequency sky-wave telecommunications systems, *ESSA Tech. Rep. ERL 110-ITS-78*, Washington, D. C.

DaRosa, A. V. (1974), Recent results from satellite beacon measurements, *Space Res.*, *XIV*, 209-226.

Davies, K. (1966), *Ionospheric Radio Propagation*, pp. 98 and 250, Dover, New York.

Donatelli, D. E., and R. S. Allen (1978), Temporal variability of ionospheric refraction correction, in *Proceedings of the Symposium on the Effect of the Ionosphere on Space and Terrestrial Systems*, edited by J. M. Goodman, pp. 490-496, U.S. Government Printing Office, Washington, D. C.

Donatelli, D. E., and R. S. Allen (1979), Ionospheric refractive correction using an adaptive procedure, in *Solar-Terrestrial Predictions Proceedings, IV, SD 003-017-00479-1*, pp. D1-65–D1-80, U.S. Government Printing Office, Washington, D.C.

DuLong, D. D. (1977), Reduction of the uncertainty of radar range correction, *NTIS ADA 046166*, Nat. Tech. Inform. Serv., Springfield, Va.

Gautier, T. N., and D. H. Zacharisen (1965), Use of space and time correlations in short-term ionospheric predictions, *IEEE Conf. Rec. Ann. IEEE Commun. Conv., 1st*, 671-676.

Leitinger, R., R. S. Allen, D. E. Donatelli, G. K. Hartmann (1978), Adaptive mapping of ionospheric features, in *Proceedings of the Symposium on the Effect of the Ionosphere on Space and Terrestrial Systems*, edited by J. M. Goodman, pp. 530-537, U.S. Government Printing Office, Washington, D. C.

Titheridge, J. E. (1972), Determination of ionospheric electron content from the Faraday rotation of geostationary satellite signals, *Planet. Space Sci.*, *20*, 353-369.

Wilkinson, P. J. (1979), Prediction limits for *f0F2*, in *Solar-Terrestrial Predictions Proceedings, IV*, Prediction Group Reports, *SD* 003-023-00041-9, pp. 259-278, U.S. Government Printing Office, Washington, D. C.

Proceedings of Ionospheric Effect Symposium, Alexandria, Virginia

ENHANCEMENTS AND SHARP DEPLETIONS OF TOTAL ELECTRON CONTENT IN THE NIGHTTIME EQUATORIAL IONOSPHERE

D.E. Donatelli and P.M. Walsh
Regis College Research Center
Weston, Massachusetts 02193

R.S. Allen and J.A. Klobuchar
Air Force Geophysics Laboratory
Hanscom Air Force Base, Massachusetts 01731

INTRODUCTION

Over the past decade there has been a synthesis in the understanding of nighttime processes in the equatorial ionsphere using contributions from such varied observational techniques as incoherent radar backscatter, radio scintillations, optical emissions and in-situ measurements (Basu and Kelly, 1979; Fejer and Kelly, 1980 and references therein). Considerations from aeronomy, plasma physics and numerical simulations (Ossakow et al, 1979) illustrate, to a larger extent, the unity of the diverse observations. Utilizing the fact that most of the contribution to TEC comes from the vicinity of the F-regionpeak, TEC observations are able to contribute to present understanding of the equatorial ionosphere.

The equatorial ionosphere has been continuously monitored for over two years from Ascension Island (Lon. 15° W., Lat. 8° S.,) through measurements of total electron content (TEC) using the Faraday rotation of 136 Mhz signals from the geostationary satellite SIRIO. Two characteristic features of the nighttime ionosphere will be discussed here: a post-sunset enhancement which lasts for several hours, and follows a rapid sunset decrease unattributable to the usual ionospheric decay processes; and the sudden sharp changes in the electron content along the ray path that are often superimposed on these enhancements and, to a lesser degree, on the subsequent "normal" nighttime ionosphere.

Similar measurements have been used previously in the equatorial region. Hunter (1969) in Nairobi and Koster (1972) in Ghana have reported: rapid sunset decreases in Faraday rotation, primarily emphasized in the Ghana data; and post-sunset enhancements which may equal or exceed daytime levels, greatly emphasized in the Nairobi observations.

The sudden, sharp variations, to be defined here as superimposed "structures", are most often seen as depletions in TEC. Similar features are shown by Tsunoda and Towle (1979) to be associated with radar backscatter plumes. Kaushika and de Mendonca (1974) and Aarons and Whitney (1980) have shown that sharp variations in TEC are coincident with scintillation patches. Yeh et al., (1979) tie these structures to F-region depletions measured by in-situ probes and the plasma "bubbles" of theoretical studies. The variation in occurence of thse structures, both seasonally and diurnally, within the 27 months of observations are examined here.

OBSERVATIONS

The data base for this study consists of over two years of continous measurements of TEC, from September 22, 1978 through December 21, 1980. The ray path to the SIRIO satellite from Ascension Island is directly north at an elevation angle of 80°. A schematic representation of the geographic and magnetic relationships is shown in figure 1. It is seen that field-aligned, plasma density structures in the F-region that cross this ray path map to altitudes of 600 to 1000 km. above the magnetic equator. The observation period is near the maximum of the present solar cycle; topside density measurements in the evening sector over the Atlantic Ocean near the maximum of the last solar cycle at altitudes greater than 600 km. (Burke et al, 1979), suggest that TEC measurements should be highly structured at Ascension Island.

Figures 2 and 3 contain examples of nighttime TEC as a function of UT, illustrating daily and seasonal variability. Data from figure 2 (3) come from five (six) consecutive days near the June (December) solstice. Local time lags UT by one hour. Ground sunset occurs at about 1845UT (1915UT).

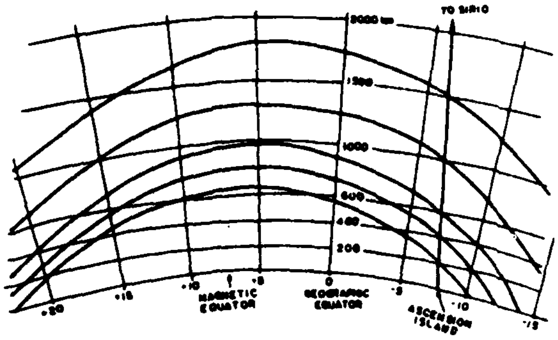

Figure 1. Schematic of Ascension Island- SIRIO ray path relationship to field lines over the magnetic equator.

A quiet, well-behaved ionosphere is expected during June at Ascension Island and found on the 10, 11, and 13 of June 1980. On some nights (June 10 and 13) the decay that begins during the sunset period persists as a gradual decrease over the entire night with only small hour-to-hour variations. On other nights (June 9, 11, and 12) there is a post-sunset increase in TEC peaking about 3 to 4 hours after sunset. Often this local maximum exceeds daytime TEC values. After the maximum, TEC usually decays to its expected pre-dawn minimum. Even during this period, however, there are examples of sudden, sharp variations in TEC. Depletions of ~15%, accompanied by intense scintillation, appear on nights (June 9 and 12) with a particularly large post-sunset enhancement. These structures have distinct boundaries which suggest east-west dimensions of 300 to 500 km, as discussed below.

The examples of figure 3 are from December 1980. Unlike June, the atypical case is the night (December 18) of no superimposed structure or scintillation activity. On all other evenings there are post-sunset enhancements of large amplitude and 2 to 3 hours duration, the largest occurring on the 17th. This day had several structures in TEC which appear as depletions, and a large finger like enhancement. If this enhancement is part of the background the depletions are ≥ 30%. These structures appear as early as 2100 UT (December 13 and 17) or as late as 0100 UT (December 16). The first structure tends to have sharp boundaries in time. Structures appearing thereafter are less distinctly bounded, suggesting either a decay process or the existence of two or more structures long the ray path.

In the examples presented here, TEC could be measured continuously throughout the day including the rapidly changing evening periods. This is not always the case. On many evenings in September through March period, fluctuations in Faraday rotation occur so rapidly that the polarization angle, and thereby TEC, are indeterminate. This occurs most often with the first appearance of structure, infrequently in the late night period.

The nocturnal and seasonal variability are summarized in the histograms of figure 4. Each histogram is a plot of the percentage of nights in which structures were observed within each 12-minute time cell during the monthly period beginning with the 22nd day of each month. There is a sharp increase (decrease) in the frequency of occurrence near the September (March) equinox with a broad maximum (minimum) between equinoxes. There is a hint of solar cycle dependences in the increased frequency of occurrence for the September 1979 to March 1980 period. This behavior is similar to that for scintillation activity discussed by Aarons et al (1980) for the 0° to 70°

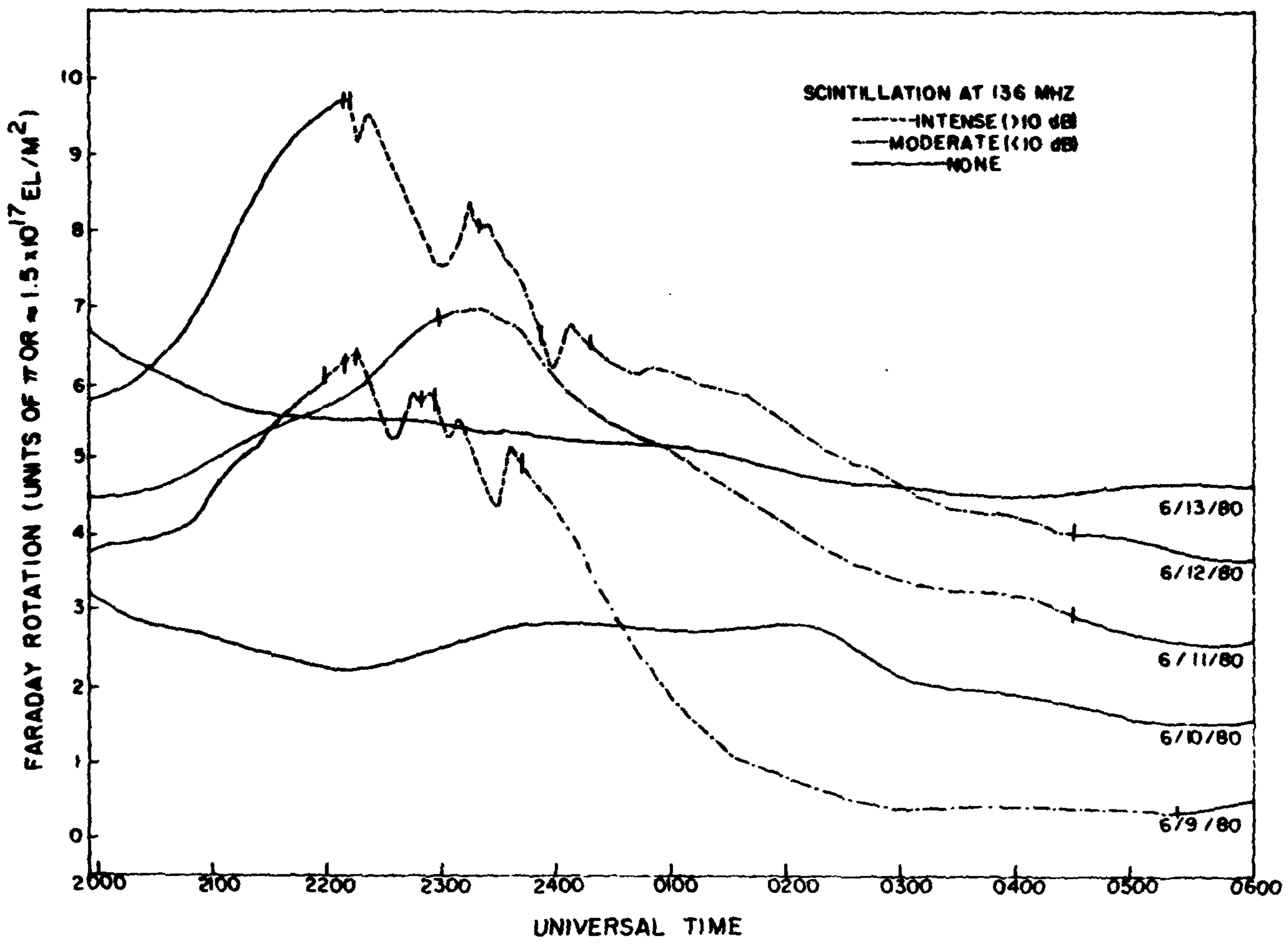

Figure 2. Measurements of nighttime TEC for five consecutive days in June 1980.

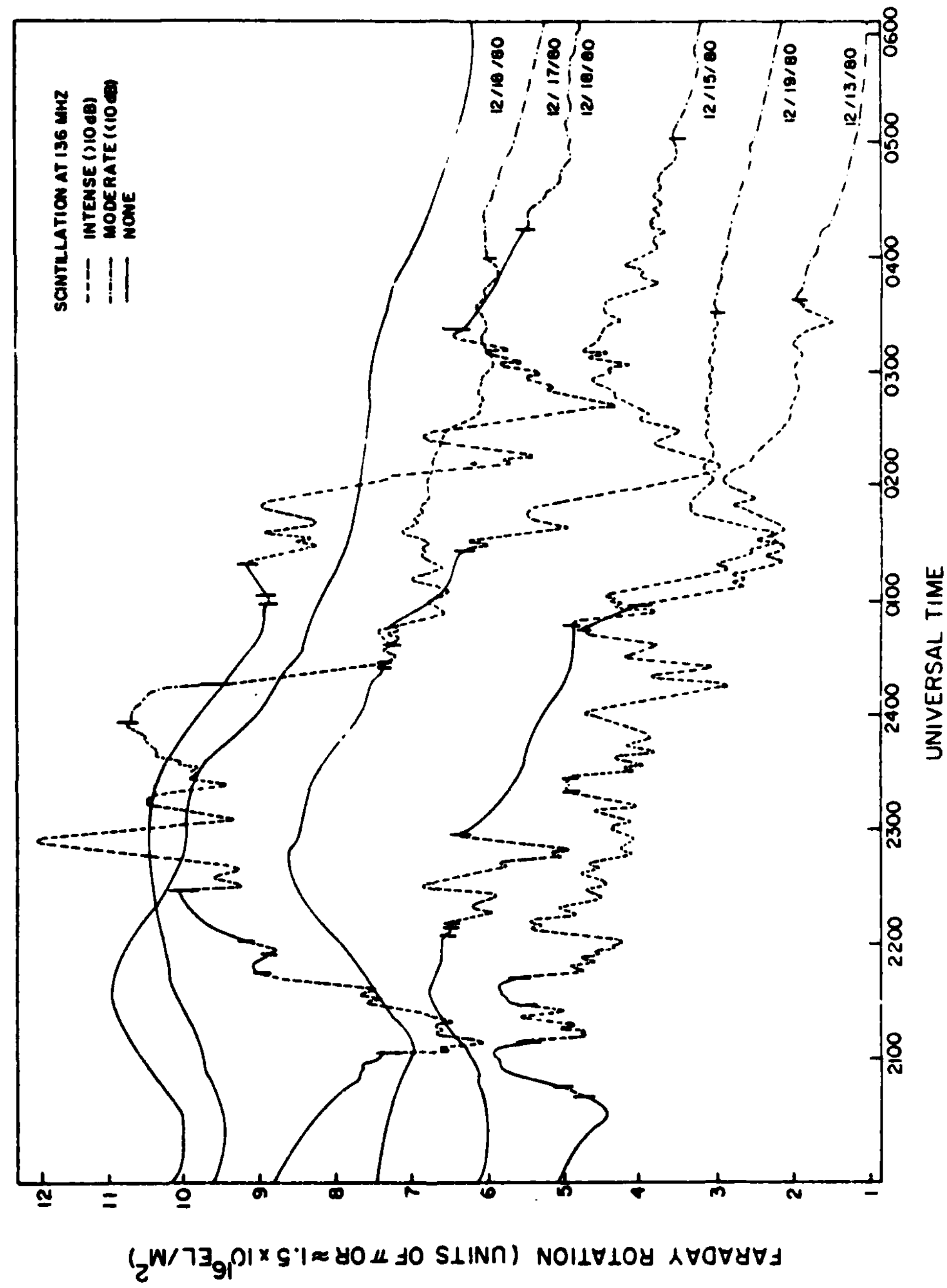

Figure 3. Measurements of nighttime TEC for six consecutive days in December 1980.

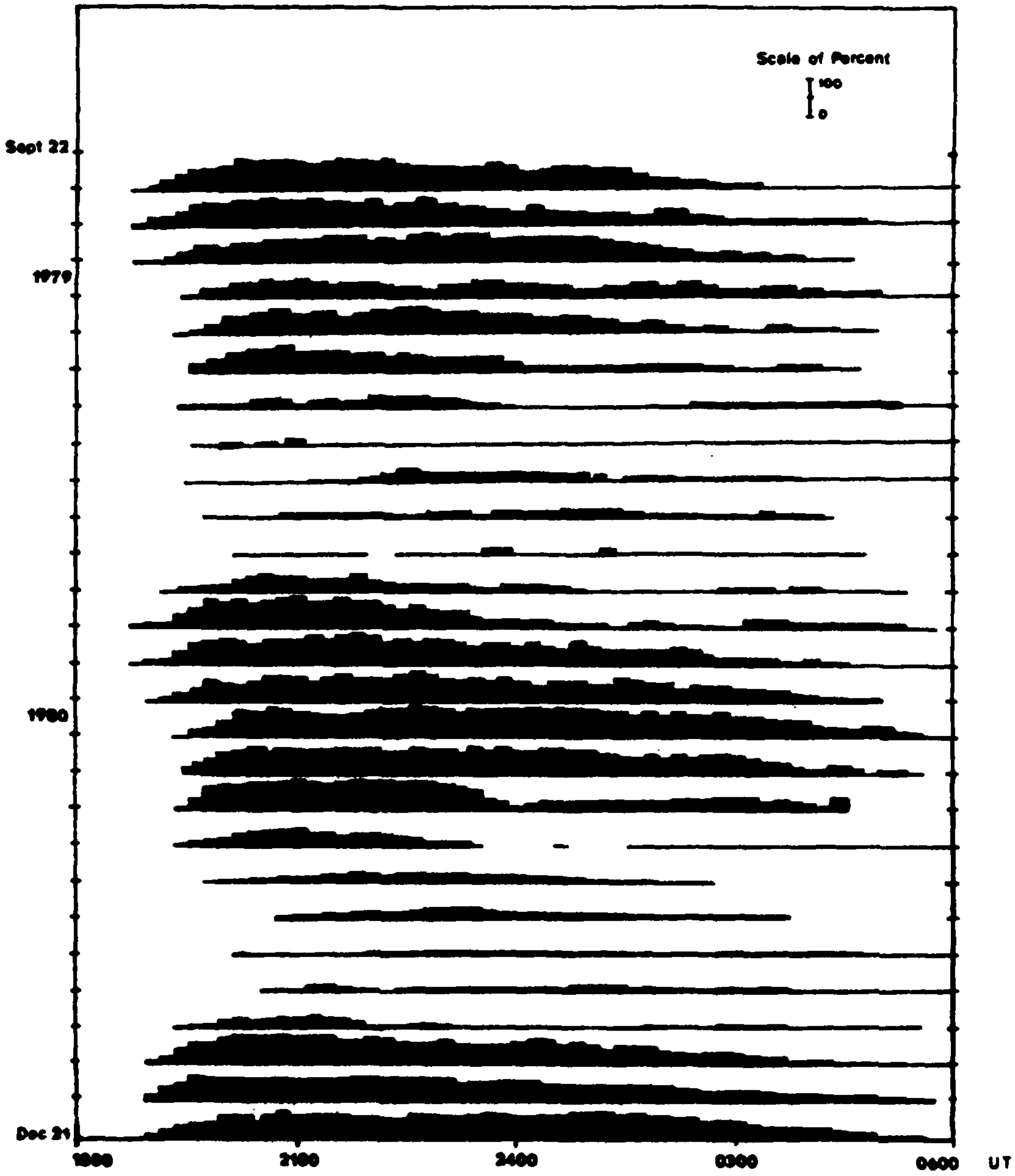

Figure 4. Histograms of percentage occurrence of structure in TEC over the nighttime for each of the 27 months of data from September 22, 1978 to December 21, 1980.

longitude sector.

These structures appear earliest in the September to December period and latest in June. The earliest structures are also those of shortest duration. Typically, they last one hour but vary from less than one minute to several hours in duration.

The nocturnal behavior shows a distinct seasonal control. A pronounced peaking in occurrence during early evening hours occurs at the equinoxes, but is obscured at the solstices. This is particularly obvious near the December solstice which has an occurence frequency comparable to that near the equinoxes for the early evening hours. The early evening behavior tends to persist throughout the night, however.

DISCUSSION

There are basically two effects being considered: first, the large post-sunset enhancements; second, the sharp structures, usually depletions, associated with them. The first has been observed by Hunter(1969) and Koster(1972) and discussed by Koster and Beer(1972) and Koster(1972). They conclude that the F-region dynamo thoery(Rishbeth, 1971) offers the most plausible explanation for this effect. Since then vertical drift measurements at Jicamarca showing large enhancements in upward drift near sunset(Fejer et al 1979) give credence to Rishbeth's theory. The use of this theory by Heelis et al(1974) in modelling these drifts produced the effect observed at Jicamarca.

Rishbeth(1971, 1977) suggests that the neutral winds in the F-region produce polarization fields that short-circuit through the E-region in daytime, but build up at sunset through the sudden drop in E-region conductivity This produces large upward drifts, resulting in a rapid lifting of the F-layer and massive transport of plasma along field lines. Near the magnetic equator this appears as a rapid sunset decline in TEC as noted by Koster(1972) with observations at dip latitude 4°. This effect is less pronounced in Hunter's(1969) observations at 13° dip latitude, and even less in the Ascension Island observations at 15° dip latitude. The subsequent enhancement, however, is more pronounced in Hunter's observations. The plasma must be transported along the field lines corresponding to the height above the magnetic equator to which the F-layer is lifted, indicating the layer is raised to altitudes $\geq$ 600 km. The topside density measurements reported by Young et al(1981) complement these observations. DMSP measurements in the post-sunset(19.5 LT) sector at 840 km. showed smooth density depletions in the immediate vicinity of the magnetic equator with enhancement in the ± 10° to 20° magnetic latitude range.

The second feature considered here is the sharp structure, often depletions, in TEC. Observational studies of the equatorial F-region suggest that these structures are plasma bubbles along the ray path. These bubbles, have been observed in the bottomside (Kelly et al, 1976), topside (Burke et al, 1979) and near the peak (McClure et al 1977) of the F layer. Presently accepted theory suggests that these begin as an E x B or collisional Rayleigh-Taylor instability in the bottomside of the F layer. The growth of the initially small perturbations depends on (1) the altitude of the initial perturbations, (2) the strength of the bottomside density gradient, (3) the altitude of the F peak, and (4) the strength of the post-sunset, eastward electric field (Ossakow et al, 1979 ; Anderson and Haerendel, 1979). Thus, large plasma depletions at and above the peak of the F layer most likely exist when the F layer is moving vertically upward.

It was noted above that most of the contributions to TEC at Ascension Island comes from flux tubes which cross the magnetic equator at altitudes between 600 and 1000 km. Young et al (1981) have found that in the Atlantic-African longitude sector, plasma bubbles appear near the magnetic equator at 840 km. on more than 80% of DMSP passes between 2000 and 2200 LT and never before 2000LT. This conicides with the local time at which the first structure of the evening appears in TEC at Ascension Island during the seasons of highest occurrence frequency.

The first structure of the evening is usually well defined, and as noted above, lasts for about one hour. This can be viewed as a structure of finite longitudinal extent drifting across the Ascension Island ray path. It has been established (Rishbeth, 1971) that post-sunset polarization electric fields cause the ionosphere to drift eastward at a faster speed than corotative. A typical value for this drift is 100 m/sec. Thus the structures appear to have longitudinal widths of about 300-400 km.

Structures that appear later in the evening usually have less well-defined boundaries. Two possible explanations are presented. First: Costa and Kelley(1978) suggest that plasma bubbles grow as large amplitude Rayleigh- Taylor waves. Sharp density gradients develop at the boundaries of the bubbles which give rise to small wavelength drift wave instabilities. The drift waves grow at the expense of the density gradient causing cross-field line diffusion, leading to decaying boundaries. Second: the ray path passes through more than one structure. This occurs if the wind speed varies with height. This would produce a shearing effect on the drifting structures, allowing portions of two or more structures to cross the ray path simultaneously.

The seasonal variation in the occurrence of these structures bears a similarity to the behavior of the vertical drift measurements of Fejer et al (1979). The most structure is observed in months for which the pre-reversal enhancement of vertical drift is greatest. This emphasizes the relationship of these structures to the evening enhancement in TEC, i.e. the enhancement as a pre-condition for the existence of structure. A clue to the difference in nocturnal behavior with season may be provided by McClure et al (1977). They observed that some "bubbles" drift more slowly than others, and in some cases, they move with the velocity of the background plasma. If the faster moving ones were to occur at the equinoxes, the slower, at the solstice, those occurring at the solstices would be longer lived.

ACKNOWLEDGEMENTS

This work was supported, in part, under the provisions of USAF contract # F19628-80-C-0016 with Regis College.

REFERENCES

Aarons, J., J.P. Mullen, J.R. Koster, R.F. da Silva, J.R. Medeiros, R.T. Medeiros, A. Bushby, J. Pantoja, and J. Lanat, Seasonal and geomagnetic control of equatorial scintillations in the 1° to 69° W longitudinal sector, J. Atmos, Terr. Phys., in press, 1980.

Aarons, J., and H.E. Whitney, Recent Observations of Equatorial and High Latitude Scintillations, AGARD Conference Proceedings # 284, Propagation Effects in Space/Earth Systems, 1980.

Anderson, D.N., and G. Haerendel, The motion of depleted plasma regions in the equatorial ionosphere J. Geophys. Res., 84, 4251, 1979.

Basu, S. and M.C. Kelley, A review of recent observations of equatorial scintillations and their relationship to current theories of F-region irregularity generation, Radio Sci., 14, 471, 1979.

Burke, W.J., D.E. Donatelli, R.C. Sagalyn, and M.C.Kelley, Observations of low density regions at high altitude in the topside equatorial ionosphere and their interpretation in terms of equatorial Spread F, Planet, Sp. Sci., 27, 593, 1979.

Costa, E., and M.C. Kelley, Linear theory for the collisionless drift wave instability with wave-lenghts near the ion gyroradius, J. Geophys. Res., 83, 4365, 1978.

Fejer, B.G., D.T. Farley, R.F. Woodman, and C.Calderon, Dependende of equatorial F-region vertical drifts on season and solar cycle, J. Geophys. Res., 84, 5792, 1979.

Fejer, B.G., M.C. Kelley, Ionospheric Irregularities, Res. Geophys. Space Phys., 18, 401, 1980.

Heelis, R.H., P.C. Kendall, R.J. Moffet, D.W. Windle, and H. Rishbeth, Electric coupling of the E and F regions and its effect on F region drifts and winds, Planet. Space Sci., 22, 743, 1974.

Hunter, A.N. Faraday rotation of the 136 MHz Transmission from geostationary satellite "Canary Bird" observed at Nairobi, Radio Sci., 4, 811, 1969.

Kaushika, N.D. and F. de Mendonca, Nighttime fluctuations (scintillations) in Faraday rotation angle of VHF signals from geostationary satellites, Planet. Space Sci., 22, 1331, 1974.

Kelley, M.C., G. Haerendel, H. Kappler, A. Valenzuela, B.B.Balsley, D.A. Carter, W.L. Ecklund, C.W. Carlson, B. Hausler, and R. Torbert, Evidence for a Rayleigh-Taylor type instability and upwelling of depleted density regions during equatorial spread F, Geophys, Res, Lett., 3, 448, 1976.

Koster, J.R., Equatorial Scintillation, Planet, Space Sci., 20, 1999, 1972.

Koster, J.R. and T.Beer, An interpretation of ionospheric Faraday rotation observations at the equator, Department of Physics, University of Ghana, 1972.

McClure, J.P., W.B. Hanson, and J.F. Hoffman, Plasma bubbles and irregularities in the equatorial ionosphere, J. Geophys. Res., 82, 2650, 1977.

Ossakow, S.L., S.T. Zalesak, B.E. McDonald, and P.K. Chaturvedi ; Nonlinear equatorial spread F; Dependence on altitude at the F peak and bottomside background electron density gradient scale length, J. Geophys, Res., 84, 17, 1979.

Rishbeth, H., Polarization fields produced by winds in the equatorial F-region, Planet. Space Sci., 19, 357, 1971

Rishbeth, H., Dynamics of the equatorial F-region J. Atmos. Terr. Phys., 39, 1159, 1977.

Tsunoda, R.T., and D.M. Towle, On the spatial relationship to 1-meter equatorial spread- F irregularities and depletions in the total electron content, Geophys. Res. Lett., 6, 873, 1979.

Young, E.R., W.J., Burke, F.J. Rich, R.C. Sagalyn, and M. Smiddy, The global distribution of equatorial spread F in the topside ionosphere during equinoctial periods, Proceedings of this Symposium, 1981.

Yeh, K.C., H. Soicher, and C.H.Lai, Observations of Equatorial Ionospheric Bubbles by the Radio Propagation Method, J. Geophys. Res., 84, 6589, 1979.

J. Phys. D: Appl. Phys., 14 (1981) 851–60. Printed in Great Britain

Ion line enhancement in ionospheric heating experiments

M C Lee
Regis College Research Center, Weston, MA 02193, USA

Received 4 July 1980, in final form 8 December 1980

Abstract. Ion line enhancement detected by the Arecibo 430 MHz radar is interpreted to be a result of nonlinear interaction of weak Langmuir waves via ponderomotive force. These weak Langmuir waves originate in the scattering of the O-mode heater wave and of the excited Langmuir waves from thermal ion acoustic waves. Theoretical analysis shows that those enhanced density irregularities associated with ion lines are forced ion acoustic modes; but their frequencies, determined by the beat frequencies of Langmuir waves, are not necessarily their characteristic frequencies. It is expected that much stronger ion line enhancement would be observed if back-scatter radar of lower frequencies (e.g. 50 MHz) was employed.

1. Introduction

It has been observed in ionospheric heating experiments (see *Radio Science*, November 1974) that the density fluctuations of the ionosphere can be greatly enhanced by powerful radio waves. Figure 1 shows a typical power spectrum detected by the Arecibo incoherent back-scatter radar from the ionospheric F region, which is illuminated by a powerful HF O-mode radio wave known as a heater wave. This power spectrum contains two components, namely, plasma lines and ion lines. Plasma lines are the signals with upshifted and downshifted frequency slightly less than the heater wave frequency (f_h). They are the pair of narrow lines located at 430 MHz $\pm f_h$ in figure 1 (where 430 MHz is the Arecibo radar frequency). Ion lines correspond to the double-humped frequency spectrum straddling the radar frequency. The pair of ion lines are broadened by the Landau damping with a Doppler spread of the order of the ion acoustic frequency.

Existing theories (Fejer and Kuo 1973, Perkins *et al* 1974) show that the O-mode heater wave can generate a spectrum of unstable Langmuir waves near its reflexion layer in the ionosphere via parametric decay instability. These unstable Langmuir waves propagate within a narrow cone centred on geomagnetic field lines. Their angles of propagation are estimated to be less than 20° for the power of the heater wave used in the experiments. However, the angle between the Arecibo radar beam and the geomagnetic field line in the modified ionospheric F region is about 45°. Hence, the weak plasma lines at 45° observed at Arecibo are interpreted to result from the scattering of the heater wave and of the unstable Langmuir waves from thermal ion acoustic waves (Fejer and Kuo 1973, Perkins *et al* 1974). But much stronger plasma lines at 90° observed at Boulder, Colorado, have been suggested to be caused by a similar process from intense field-aligned density irregularities, rather than from thermal ion acoustic waves (Fejer

0022-3727/81/050851+10 \$01.50 © 1981 The Institute of Physics

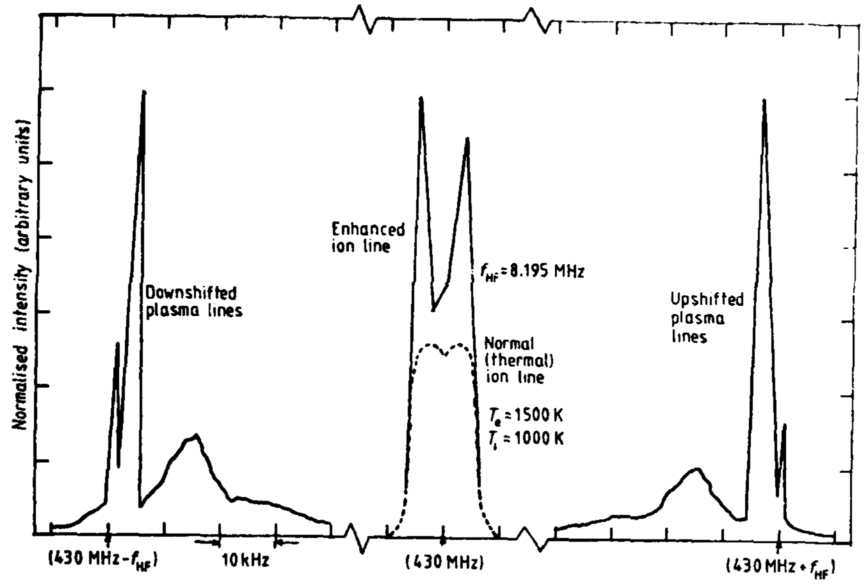

Figure 1. A typical power spectrum detected by the Arecibo 430 MHz monostatic radar during ionospheric heating experiments (adapted from Showen and Kim 1978) showing HF-induced enhancement. Plasma lines are the pair of narrow lines located at 430 MHz ± f_h where f_h, the heater wave frequency, is of the order of several MHz. Ion lines at thermal and enhanced levels correspond to the broad double-humped portion straddling the radar frequency (Hagfors and Zamlutti 1973).

1975). According to the theory of parametric decay instability, a spectrum of unstable ion acoustic waves propagating nearly along geomagnetic field lines is also concurrently generated. It is clear that the enhanced ion lines at 45° detected at Arecibo cannot be these ion acoustic waves. We suggest that this ion line enhancement arises from the nonlinear interaction of Langmuir waves via ponderomotive force. Thermal interaction of Langmuir waves is discussed by Perkins (1974) and by Lee and Fejer (1978), who interpret the generation of intense density striations.

This paper presents a qualitative investigation of the Arecibo ion line enhancement. Section 2 describes the power spectrum of induced low-frequency number density fluctuations associated with the enhanced ion lines. As shown, these induced fluctuations are forced ion acoustic modes whose frequencies (determined by the beat frequencies of Langmuir waves) are not necessarily their characteristic frequencies. Interpretation and discussion of the Arecibo ion line enhancement are finally presented in §3.

2. Induced low-frequency number density fluctuations

2.1. Ponderomotive force

In the presence of two high-frequency waves (e.g. two Langmuir waves, or one Langmuir wave and one electromagnetic wave), electrons experience a wave-like nonlinear Lorentz force whose frequency is the difference between these two high-frequency waves. If both thermal motion of electrons and geomagnetic effect are neglected, this nonlinear force acting on an electron has the following expression

$$\boldsymbol{F}=\mathrm{Re}\left[\frac{\mathrm{i}e^2E_{k_1}E_{k_2}}{2m}\left(\frac{\boldsymbol{k}_1}{k_1}\cdot\frac{\boldsymbol{k}_2}{k_2}\right)\left(\omega_1^{-2}\boldsymbol{k}_2-\omega_2^{-2}\boldsymbol{k}_1\right)\times\exp\left[\mathrm{i}(\omega_1-\omega_2)t-\mathrm{i}(\boldsymbol{k}_1-\boldsymbol{k}_2)\cdot\boldsymbol{r}-\mathrm{i}(\varphi_1-\varphi_2)\right]\right] \tag{1}$$

where E, ω, $\boldsymbol{k}$, φ, e and m are wave electric field amplitude, wave frequency, wave vector, wave phase angle, electric charge, and electron mass respectively. This nonlinear Lorentz force is generally called the ponderomotive force.

Equation (1) is appropriate for the case concerned, since the phase velocities of those high-frequency waves are much greater than the thermal velocities of electrons in the ionosphere, and the wave frequencies are about five times the electron cyclotron frequency. Furthermore, since the wave frequencies of high-frequency waves (the heater wave and the excited Langmuir waves) are just slightly larger than the electron plasma frequency ω_p, equation (1) can be approximated by (Kuo and Fejer 1972)

$$\boldsymbol{F}=\mathrm{Re}\left[\frac{\mathrm{i}e^2E_{k_1}E_{k_2}}{2m\omega_p^2}\left(\frac{\boldsymbol{k}_1}{k_1}\cdot\frac{\boldsymbol{k}_2}{k_2}\right)(\boldsymbol{k}_2-\boldsymbol{k}_1)\exp\left[\mathrm{i}(\omega_1-\omega_2)t-\mathrm{i}(\boldsymbol{k}_1-\boldsymbol{k}_2)\cdot\boldsymbol{r}-\mathrm{i}(\varphi_1-\varphi_2)\right]\right] \tag{2}$$

The ponderomotive force experienced by a singly-charged ion is $\boldsymbol{F}(m/M)\sim10^{-4}\,\boldsymbol{F}$, where (m/M) is the mass ratio between an electron and an ion. Ions are, therefore, considered to be immobile in the electric fields of high-frequency waves. However, electron bunching caused by $\boldsymbol{F}$ results in a charge-separation electric field $\boldsymbol{E}_{cs}$. Hence, the net force acting on an electron is $(\boldsymbol{F}-e\boldsymbol{E}_{cs})$, while that acting on an ion is approximately $e\boldsymbol{E}_{cs}$.

2.2. *Dispersion relation of density perturbations*

The corresponding number density perturbations in electrons and in ions can be obtained from the linearisation of their equations of continuity

$$\frac{\partial}{\partial t}(en_e)+\nabla\cdot n_e\sigma_e\left(\frac{\boldsymbol{F}}{e}-\boldsymbol{E}_{cs}\right)=0 \tag{3}$$

$$\frac{\partial}{\partial t}(en_i)+\nabla\cdot(n_i\sigma_i\boldsymbol{E}_{cs})=0 \tag{4}$$

by assuming that all perturbations have a space-time dependence of the same form as $\boldsymbol{F}$, i.e. of the $\exp\left[\mathrm{i}(\omega_1-\omega_2)t-\mathrm{i}(\boldsymbol{k}_1-\boldsymbol{k}_2)\cdot\boldsymbol{r}\right]$ type. Thus, equations (3) and (4) lead to

$$n_e=n_0\,\frac{\sigma_e}{e}\left(\frac{\boldsymbol{F}}{e}-\boldsymbol{E}_{cs}\right)\cdot\frac{(\boldsymbol{k}_1-\boldsymbol{k}_2)}{(\omega_1-\omega_2)} \tag{5}$$

and

$$n_i=n_0\,\frac{\sigma_i}{e}\,\boldsymbol{E}_{cs}\cdot\frac{(\boldsymbol{k}_1-\boldsymbol{k}_2)}{(\omega_1-\omega_2)} \tag{6}$$

where n_0 is the unperturbed plasma density, and σ_e and σ_i are the electric conductivities for electrons and ions respectively. The density perturbations n_e and n_i are approximately equal, since the plasma remains neutral for low-frequency perturbations on scales much larger than the Debye length. In the case of interest, the wavelength of the low-frequency perturbations picked up by Arecibo 430 MHz monostatic radar is about 35 cm, which is quite large as compared to the Debye length (~ 0.3 cm). Therefore, either equation (5) or equation (6) may be written as

$$n_{12} = n_0 \frac{\boldsymbol{F} \cdot (\boldsymbol{k}_1 - \boldsymbol{k}_2) \sigma_e \sigma_i}{e^2 (\omega_1 - \omega_2)(\sigma_e + \sigma_i)} \tag{7}$$

which represents the low-frequency number density perturbations induced by the nonlinear interaction of the two high-frequency waves via ponderomotive force.

In the absence of external disturbance, i.e. $\boldsymbol{F} = 0$, the dispersion relation of these low-frequency modes can be obtained by setting the denominator of (7) to be zero, namely

$$\sigma_e + \sigma_i = 0. \tag{8}$$

2.3. *Determination of σ_e and σ_i*

Because the wavelength (~ 35 cm) of induced fluctuations of interest is much shorter than electron collision mean free path (several hundreds of meters in the F region), the electric conductivities σ_e and σ_i are determined by Vlasov plasma dynamics. In addition, the wave frequency of these induced fluctuations $\omega (= \omega_1 - \omega_2)$ satisfies the following inequalities:

$$\Omega_i \ll \omega \sim kC_s < \omega_i \ll \Omega_e < \omega_p$$

where Ω_i, C_s, ω_i, Ω_e, and ω_p are the ion cyclotron frequency, ion acoustic velocity, ion plasma frequency, electron cyclotron frequency, and electron plasma frequency respectively; $k = |\boldsymbol{k}_1 - \boldsymbol{k}_2|$. Ions can, therefore, be treated as unmagnetised, and electrons as strongly magnetised. Nevertheless, since the electron cyclotron radii (a few centimetres in the F region) are smaller than the low-frequency wavelength (~ 35 cm), electrons can move freely along the geomagnetic field to neutralise ionic perturbations as long as these low-frequency perturbations do not propagate perpendicularly across geomagnetic field lines. As mentioned before, ionic fluctuations at 45° are detected by the Arecibo monostatic radar. Thus, neglecting the geomagnetic effect on electrons as well is still a good approximation.

Mathematically, ion dynamics are described by

$$\frac{\partial}{\partial t} f_i + \boldsymbol{v} \cdot \frac{\partial}{\partial \boldsymbol{r}} f_i + \frac{e}{M} \boldsymbol{E} \cdot \frac{\partial}{\partial \boldsymbol{v}} f_i = 0$$

where f_i is the ion distribution function in the presence of electrostatic disturbance ($\boldsymbol{E} = \boldsymbol{E}_{es}$) due to electron bunching caused by ponderomotive force: f_i is represented by a linear combination of perturbed and unperturbed components, namely, $f_i = f_{i1} + f_{i0}$. The unperturbed distribution function f_{i0} is assumed to be of the isotropic Maxwellian type

$$f_{i0} = \left(\frac{M}{2\pi T_i}\right)^{3/2} \exp\left(-\frac{Mv^2}{2T_i}\right).$$

It can be shown that the ion conductivity is given by

$$\sigma_i = i \frac{\omega \varepsilon_0}{k^2 h_i^2} \left(\frac{M}{2T_i}\right)^{1/2} \int_L dU \frac{U \exp(-MU^2/2T_i)}{U - (\omega/k)} \tag{9}$$

where L indicates that integration follows the Landau prescription; h_i is the ion Debye length. If ω is real, equation (9) may be written as

$$\sigma_{\rm i}=(\mathrm{i}\omega\varepsilon_0/k^2h_{\rm i}^2)\,[1-2\,\alpha_{\rm i}\exp(-\alpha_{\rm i}^2)\int_0^{\alpha_{\rm i}}\mathrm{d}\tau\exp(\tau^2)-\mathrm{i}\pi^{1/2}\,\alpha_{\rm i}\exp(-\alpha_{\rm i}^2)] \tag{10}$$

or

$$\sigma_{\rm i}=(\mathrm{i}\omega\varepsilon_0/k^2h_{\rm i}^2)[1-\alpha_{\rm i}Z(-\alpha_{\rm i})] \tag{11}$$

where $Z(-\alpha_{\rm i})$ is the so-called plasma dispersion function (Fried and Conte 1961); $\alpha_{\rm i}=(\omega/k)(M/2T_{\rm i})^{1/2}$.

Electron dynamics are represented by the following Vlasov equation

$$\frac{\partial}{\partial t}f_{\rm e}+\boldsymbol{v}\cdot\frac{\partial}{\partial \boldsymbol{r}}f_{\rm e}-\frac{e}{m}(\boldsymbol{E}+\boldsymbol{v}\times\boldsymbol{B}_0)\cdot\frac{\partial}{\partial \boldsymbol{v}}f_{\rm e}=0$$

where $f_{\rm e}$ is the electron distribution function under electrostatic disturbance $\boldsymbol{E}=\boldsymbol{E}_{\rm cs}-\boldsymbol{F}/e$ associated with ponderomotive force; $\boldsymbol{B}_0$ is uniform geomagnetic field. $f_{\rm e}$ is similarly composed of two components, namely, $f_{\rm e}=f_{\rm e1}+f_{\rm e0}$. The unperturbed distribution function $f_{\rm e0}$ is also assumed to be Maxwellian, as given by equation (12)

$$f_{\rm e0}=(m/2\pi T_{\rm e})^{3/2}\exp(-mv^2/2T_{\rm e}). \tag{12}$$

The electron conductivity can then be shown to have the form (Bernstein 1958)

$$\sigma_{\rm e}=\frac{i\varepsilon_0\omega}{k^2h_{\rm e}^2}\left[1-2\mathrm{i}\frac{\omega}{\Omega_{\rm e}}\int_0^{-\infty}\mathrm{d}\beta\exp\left(-\mathrm{i}\frac{2\beta\omega}{\Omega_{\rm e}}-k^2r_{\rm e}^2(\beta^2\cos^2\theta+\sin^2\beta\sin^2\theta)\right)\right] \tag{13}$$

where θ is the angle between the wave propagation vector $\boldsymbol{k}$ and the geomagnetic field $\boldsymbol{B}_0$; $r_{\rm e}$ is the electron cyclotron radius defined by

$$r_{\rm e}=(2T_{\rm e}/\Omega_{\rm e}^2m)^{1/2}.$$

For the parameters of present interest the term with $\sin^2\beta\sin^2\theta$ in equation (13) can be neglected. Then, after some straightforward mathematical manipulation, equation (13) can be written as

$$\sigma_e=\frac{i\varepsilon_0\omega}{k^2h_{\rm e}^2}\left(1+2\,\mathrm{i}\alpha_{\rm e}\exp(-\alpha_{\rm e}^2)\int_{-\infty}^{i\alpha_{\rm e}}\mathrm{d}\tau\exp(-\tau^2)\right) \tag{14}$$

or, in terms of the plasma dispersion function, equation (14) takes the form

$$\sigma_{\rm e}=(i\varepsilon_0\omega/k^2h_{\rm e}^2)\,[1+\alpha_{\rm e}Z(\alpha_{\rm e})] \tag{15}$$

where $\alpha_{\rm e}=(\omega/k)(m/2T_{\rm e})^{1/2}(\cos\theta)^{-1}$. Since $\alpha_{\rm e}\ll 1$, equation (15) can be well approximated by

$$\sigma_{\rm e}\simeq e\varepsilon_0\omega/k^2h_{\rm e}^2. \tag{16}$$

This final form of $\sigma_{\rm e}$ shows that the geomagnetic effect on electrons turns out to be negligible for the low-frequency fluctuations of interest. Recall that the wavelength (~35 cm) of these induced fluctuations is larger than the electron cyclotron radius (~2 cm) by one order of magnitude and that their wave propagation angle (~45°) is far from being perpendicular to geomagnetic field lines.

Substituting equations (9) and (16) into equation (8) and separating the real and imaginary parts leads to the following two equations

$$\mathrm{Re}(\omega)=C_{\rm s}k \tag{17}$$

$$\mathrm{Im}(\omega)=\pi^{1/2}(C_{\rm s}^4/v_{\rm i}^3)\,k\exp(-T_{\rm e}/T_{\rm i}). \tag{18}$$

Equation (17) indicates that these low-frequency plasma fluctuations are essentially ion acoustic modes, whose Landau damping rate is given by equation (18).

However, in the presence of external disturbance, i.e. $F \neq 0$, ω is real and determined as the difference frequency of two high-frequency waves. Substituting equations (2), (11) and (16) into equation (7) yields the specific form of number density perturbations caused by nonlinear interaction of two high-frequency waves via the ponderomotive force

$$n_{12}(t, \boldsymbol{r}) = -\frac{E_{k_1} E_{k_2} \varepsilon_0}{2T_i} n_0 \left(\frac{\boldsymbol{k}_1}{k_1} \cdot \frac{\boldsymbol{k}_2}{k_2}\right) \frac{\exp[\mathrm{i}(\omega t - \boldsymbol{k} \cdot \boldsymbol{r}) - \mathrm{i}(\varphi_1 - \varphi_2)]}{\{(T_e/T_i) + [1 - \alpha_i Z(-\alpha_i)]^{-1}\}} \tag{19}$$

where $\boldsymbol{k} = \boldsymbol{k}_1 - \boldsymbol{k}_2$ and $\omega (= \omega_1 - \omega_2)$ is the driving frequency of the ponderomotive force. These low-frequency density perturbations are, consequently, forced ion acoustic modes, which are not necessarily excited at their characteristic frequencies.

In terms of the Fourier transform $n_{12}(\omega, \boldsymbol{k})$ of $n_{12}(t, \boldsymbol{r})$, i.e.

$$n_{12}(\omega, \boldsymbol{k}) = \int_{V_L t_L} n_{12}(t, \boldsymbol{r}) \exp[-\mathrm{i}(\omega t - \boldsymbol{k} \cdot \boldsymbol{r})] \, \mathrm{d}t \, \mathrm{d}\boldsymbol{r}$$

equation (19) becomes

$$n_{12}(\omega, \boldsymbol{k}) = -\frac{E_{k_1} E_{k_2} \varepsilon_0}{2T_i} n_0 \left(\frac{\boldsymbol{k}_1}{k_1} \cdot \frac{\boldsymbol{k}_2}{k_2}\right) V_L t_L \left(\frac{T_e}{T_i} + [1 - \alpha_i \cdot Z(-\alpha_i)]^{-1}\right)^{-1} \exp[-\mathrm{i}(\varphi_1 - \varphi_2)] \tag{20}$$

where V_L is a very large volume and t_L a very long time interval.

2.4. *Power spectrum and radar cross-sections of low-frequency perturbations*

The power spectrum $\langle |n(\boldsymbol{k}, \omega\rangle|^2\rangle$ of low-frequency number density perturbations, caused by the heater wave and a spectrum of randomly phased Langmuir waves, is obtained from the generalisation of equation (20) as follows:

$$\begin{aligned} \langle |n(\omega, \boldsymbol{k}\rangle|^2\rangle &= \left\langle \sum_{\boldsymbol{k}} |n_{12}(\omega, \boldsymbol{k})|^2 \right\rangle = n_0^2 V_L^2 t_L^2 \left(\left| \frac{T_e}{T_i} + [1 - \alpha_i Z(-\alpha_i)]^{-1} \right| \right)^{-2} \\ &\quad \times \left\langle \sum_{\boldsymbol{k}} \left| \frac{E_{k_1} E_{k_1 - k} \varepsilon_0}{2T_i} \left(\frac{\boldsymbol{k}_1}{|\boldsymbol{k}_1|} \cdot \frac{(\boldsymbol{k}_1 - \boldsymbol{k})}{|\boldsymbol{k}_1 - \boldsymbol{k}|} \right) \exp[-\mathrm{i}(\varphi_1 - \varphi_2)] \right|^2 \right\rangle \end{aligned} \tag{21}$$

where $\langle | \quad |^2\rangle$ indicates that the absolute value of physical quantities concerned is squared and phased-averaged. It should be noted that $\boldsymbol{k}_2$'s in equation (20) have been replaced by $(\boldsymbol{k}_1 - \boldsymbol{k})$'s in equation (21). The summation in equation (21) is taken over all pairs of high-frequency waves whose beat products satisfy the prescribed value $(\omega, \boldsymbol{k})$.

If those randomly phased Langmuir waves are characterised by a spectral density $W(\boldsymbol{k}_1)$

$$\varepsilon_0 E^2{}_{lmn} = 2 W(k_l, k_m, k_n)(\Delta k)^3$$

where k_l, k_m and k_n are the three perpendicular components of $\boldsymbol{k}_1$ in a rectangular coordinate system. $k_l = l(\Delta k)$, where $l = \ldots, -2, -1, 0, 1, 2 \ldots,$ and Δk is an infinitesimal defined by $2\pi V_L^{-1/3}$. It follows from Lee and Fejer (1978) that the summation in equation (21) is replaced by integration and thus

$$\begin{aligned} \langle |n(\omega, \boldsymbol{k})|^2\rangle &= 16\pi^4 V_L t_L n_0^2 T_i^{-2} \{|(T_e/T_i) + [1 - \alpha_i Z(-\alpha_i)]^{-1}|\}^{-2} \\ &\quad \times \iint W(\boldsymbol{k}_1) W(\boldsymbol{k}_1 - \boldsymbol{k}) (\partial\omega/\partial k_{1x})^{-1} \, \mathrm{d}k_{1y} \, \mathrm{d}k_{1z} \end{aligned} \tag{22}$$

where the z axis is taken along the direction of geomagnetic field, and the double integral is taken over the surface $\omega = \text{constant}$.

The power spectrum $\langle |n(\omega, \boldsymbol{k})|^2 \rangle$ is related to the average differential scattering cross-section $\varphi(\omega_0 + \omega)$ by

$$\sigma(\omega_0 + \omega)\, \mathrm{d}\omega = (2\pi V_L t_L)^{-1} \sigma_T \langle |n(\omega, \boldsymbol{k})|^2 \rangle\, \mathrm{d}\omega \tag{23}$$

where ω_0 is the incoherent radar frequency (430 MHz in the present case), and σ_T the Thomson differential cross-section. Substituting equation (22) into (23) leads to the final result

$$\sigma(\omega_0 + \omega)\, \mathrm{d}\omega = 8\, \pi^3 n_0^2 T_i^{-2} \sigma_T \{ |(T_e/T_i) + [1 - \alpha_i Z(-\alpha_i)]^{-1}| \}^{-2} \times \left[\iint W(\boldsymbol{k}_1) W(\boldsymbol{k}_1 - \boldsymbol{k}) (\partial\omega/\partial k_{1x})^{-1}\, \mathrm{d}k_{1y}\, \mathrm{d}k_{1z} \right] \mathrm{d}\omega \tag{24}$$

which specifically expresses the radar measurement (per unit incident power per unit solid angle per unit volume and per unit frequency interval) of average power scattered incoherently from the enhanced plasma density fluctuations due to nonlinear wave–wave interaction via the ponderomotive force.

Computation of equation (24) seems to be complicated, but a crude estimate of $\sigma(\omega_0 + \omega)$ can be made as follows. Remember that ω in equation (24) is the frequency difference between two Langmuir waves: one with the wave number $\boldsymbol{k}_1$ and the other with $(\boldsymbol{k}_1 - \boldsymbol{k})$, namely

$$\omega = \omega_1(\boldsymbol{k}_1) - \omega_2(\boldsymbol{k}_1 - \boldsymbol{k}).$$

If the Bohm–Gross relation is used as the dispersion relation of Langmuir waves, then

$$\omega = \tfrac{3}{2} h_e^2 \omega_p (2\boldsymbol{k}_1 \cdot \boldsymbol{k} - \boldsymbol{k}_2)$$

and therefore

$$\partial\omega/\partial k_{1x} = 3 h_e^2 \omega_p k \sin\theta \tag{25}$$

where θ is the angle between $\boldsymbol{k}$ and the earth's magnetic field which coincides with the z axis. $\boldsymbol{k}$ lies in the x–z plane.

It follows from equation (25) that (24) can be written as

$$\sigma(\omega_0 + \omega) = 8\pi^3 n_0^2 T_i^{-2} 3^{-1} h_e^{-2} \omega_p^{-1} k^{-1} \sin^{-1}\theta A(\alpha_i) \sigma_T \times \iint W(\boldsymbol{k}_1) W(\boldsymbol{k}_1 - \boldsymbol{k})\, \mathrm{d}k_{1y}\, \mathrm{d}k_{1z} \tag{26}$$

where $A(\alpha_i) = \{ |(T_e/T_i) + [1 - \alpha_i Z(-\alpha_i)]^{-1}| \}^{-2}$ determining the shape of ion lines. $A(\alpha_i)$ versus α_i for $T_e/T_i = 1.0$, 1.5 and 2.0 are plotted in figure 2. For a larger ratio of T_e to T_i, $A(\alpha_i)$ has a sharper hump located at a higher frequency. This indicates that Landau damping broadens the ion lines.

It is interesting to note that $\sigma(\omega_0 + \omega)$ in equation (26) shows a simple k^{-1} behaviour or an f^{-1} dependence on radar frequency. In other words, the theory predicts that radars of lower frequencies would detect stronger ion lines. These ion lines have less Doppler shifts as explained by an example given in §3. Much simplification of equation (26) can be achieved if we assume that the energy density $W(k_1)$ of Langmuir waves is constant inside a cylinder of radius k_r and height k_h in $\boldsymbol{k}$ space. This means that the double integral in equation (26) is expressed approximately as

$$\iint W(\boldsymbol{k}_1) W(\boldsymbol{k}_1 - \boldsymbol{k})\, \mathrm{d}k_{1y}\, \mathrm{d}k_{1z} \simeq 2 W^2 k_r k_h$$

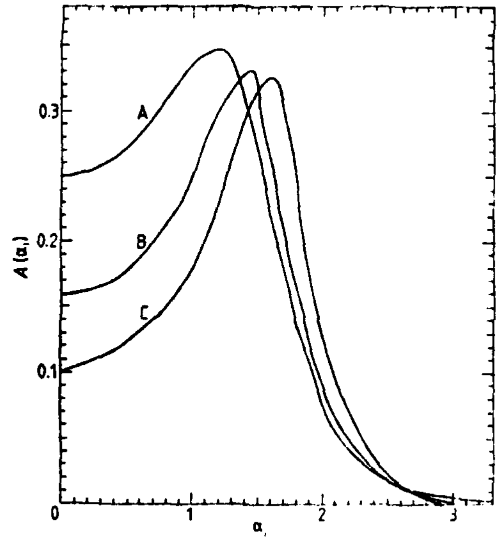

Figure 2. Graphs of $A(\alpha_i)=\{|(T_e/T_i)+[1-\alpha_i Z(-\alpha_i)]^{-1}|\}^{-2}$ as a function of $\alpha_i=(\omega/k)(m_i/2T_i)^{1/2}$ for $T_e/T_i=$(A) 1.0, (B) 1.5, and (C) 2.0.

or

$$\iint W(\boldsymbol{k}_1)\, W(\boldsymbol{k}_1-\boldsymbol{k})\, \mathrm{d}k_{1y}\, \mathrm{d}k_{1z} \simeq 2^{-1}\varepsilon_0{}^2 E^4 k_r{}^{-3}\pi^{-2}k_n{}^{-1}$$

in terms of the amplitude of Langmuir wave field E. Then, equation (26) can be written as

$$\sigma(\omega_0+\omega)=\eta E^4$$

where

$$\eta=4\pi n_0{}^2 T_i{}^{-2}\varepsilon_0{}^2 k_r{}^{-3} k_h{}^{-1} 3^{-1} h_e{}^{-2}\omega_p{}^{-1} k^{-1} \sin^{-1}\theta\, \sigma_T A(\alpha_i).$$

Equation (27) is a convenient form of the theory, from which one may estimate roughly what the Langmuir wave amplitude would have to be to produce the observed radar cross-sections.

3. Interpretation and discussion of Arecibo ion line enchancement

It is clear from figure 1 that the ion lines observed at Arecibo (Hagfors and Zamlutti 1973) are modified appreciably after ionospheric heating. However, the wave number of these ion density fluctuations is 18 m^{-1}, which is larger than the linear dimension of the k-space region occupied by the spectrum of unstable Langmuir waves (see figure 3). This spectrum of unstable Langmuir waves is adapted from the theoretical calculation of Chen and Fejer (1976). According to the theory, these unstable Langmuir waves are excited by an O-mode heater wave near its reflection layer in the ionosphere via parametric decay instability.

Obviously, the ion lines detected by the Arecibo radar at 45° cannot be generated as beat products of these unstable Langmuir waves. They may, however, be so generated by a spectrum of stable Langmuir waves which originate in the scattering of the heater wave and of the unstable Langmuir waves from thermal ion acoustic waves. These stable Langmuir waves are much weaker than those unstable Langmuir waves, but they have a

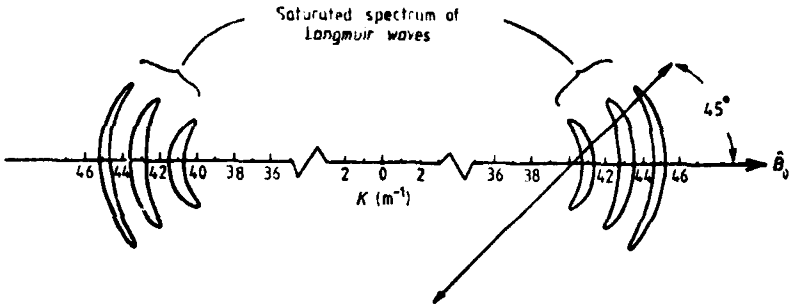

Figure 3. Illustration of the relative magnitudes of the ion acoustic mode detected by the Arecibo 430 MHz radar and of the saturated spectrum of Langmuir waves in the k space. The saucer-shaped regions represent the latter, which is adapted from the theoretical calculation of Chen and Fejer (1976). The diagonal arrow represents the wave vector of the ion fluctuations. $\hat{B}_0$ is the local geomagnetic field direction.

broader distribution in k-space. Calculation of stable Langmuir waves at 45° has quite successfully reproduced the Arecibo weak plasma line echoes (Fejer and Kuo 1973, Perkins *et al* 1974). We, therefore, interpret the weak ion line enhancement observed at Arecibo as the consequence of nonlinear interaction of stable Langmuir waves via ponderomotive force. Such a physical process is formulated in detail in §2. This interpretation leads to the expectation that ion density fluctuations of longer wavelengths (i.e. smaller wave numbers) will be enhanced strongly by the nonlinear interaction of intense unstable Langmuir waves. In other words, it is predicted that back-scatter radar of lower frequencies, say, 50 MHz, would detect at Arecibo ion lines which are strongly enhanced by intense sources (i.e. unstable Langmuir waves) in addition to their k^{-1} behaviour shown in equation (26).

We note, from figure 2, that the ion lines are located approximately at $|\alpha_i| = 1.45$ in the case of $T_e/T_i = 1.5$, where α_i is the ratio of the phase velocity (ω/k) of ion acoustic waves to their thermal velocity $(2T_i/M_i)^{1/2}$. If $T_i = 1000$ K, the frequency of forced ion acoustic modes detected by the Arecibo 430 MHz radar is about 4.2 kHz, which agrees with the observation (Hagfors and Zamlutti 1973). Under the same ionospheric condition, ion lines detected by a 50 MHz radar are estimated to have a frequency of 0.5 kHz. That is, the theory expects that much narrower ion lines would be observed by a 50 MHz radar. Moreover, since the ion lines detected by a 50 MHz radar are primarily generated by the saturated spectrum of parametrically excited Langmuir waves, the Langmuir wave field E in equation (27) is therefore given by $E = RE_0$, where E_0 is the threshold field amplitude of the decay instability, namely

$$E_0^2 = 3.42\ \varepsilon_0^{-1} n_0 (T_e + T_i)\, \nu_e/\omega_p$$

and R is the ratio of E_t^2 to E_0^2, where E_t is the largest field amplitude of the heater wave at the standing wave maxima, neglecting absorption and the magnetic field, that is, $E_t^2 = (8Pf/\varepsilon_0 c)\,(H/Z)^{1/2}$ (Fejer and Graham 1974).

Currents flowing in the k direction of ion density fluctuations may cause the two-humped ionic spectrum to become asymmetrical (Rosenbluth and Rostoker 1962). It is, however, impossible to generate such strong currents through ionospheric heating. Fejer (1977) suggested that the asymmetry of enhanced ion lines might be caused by parametric interaction of the incoherently back-scattered waves with the upgoing probing wave. This process involves a parametric instability known as stimulated Brillouin scattering. The back-scattered waves representing the lower frequency ion line are amplified, while those representing the upper frequency ion line are attenuated. Fejer (1977) estimated that an asymmetry of ± 1 % in the Arecibo ion lines was caused by stimulated Brillouin scattering.

This paper has presented a qualitative investigation of ion line enhancement; quantitative analysis of it requires knowing the spectra of stable and unstable Langmuir waves. Experimental spectra of Langmuir waves are still not available, in spite of two attempts to obtain them. It is by no means easy to calculate the theoretical spectra to meet the exact experimental conditions, since some effects, e.g. the self-focusing of the heater wave (Lee 1979), are now qualitatively clear, but it is difficult to evaluate them quantitatively. It is crucial to prove the existence of the saturated spectra of Langmuir waves now, because interpretations of some unexpected phenomena observed in ionospheric heating experiments are based on their existence. Continuing effort to measure these spectra of Langmuir waves is badly needed.

Acknowledgments

Part of this work has been presented at the National Radio Science Meeting, 6–9 November 1978, University of Colorado at Boulder, Colorado, USA.

References

Bernstein I B 1958 *Phys. Rev.* **109** 10–21
Chen H C and Fejer J A 1976 *Phys. Fluids* **18** 1809–12
Fejer J A 1975 *Phil. Trans. R. Soc.* Ser. A **280** 151–65
—— 1977 *Geophys. Res. Lett.* **4** 289–90
Fejer J A and Graham K N 1974 *Radio Sci.* **9** 1081–4
Fejer J A and Kuo Y Y 1973 *Proc. AGARD Conf.* **138** 11-1–11-8
Fried B D and Conte S D 1961 *The Plasma Dispersion Function* (New York: Academic Press)
Hagfors T and Zamlutti C J 1973 *Proc. AGARD Conf.* **138** 5-1–5-11
Kuo Y Y and Fejer J A 1972 *Phys. Rev. Lett.* **29** 1667–70
Lee M C 1979 *Proc. Nat. Radio Sci. Mtg, Boulder, Colorado, USA* to be published
Lee M C and Fejer J A 1978 *Radio Sci.* **13** 893–9
Perkins F W 1974 *Radio Sci.* **9** 1065–70
Perkins F W, Oberman C and Valeo E J 1974 *J. Geophys. Res.* **79** 1478–96
Rosenbluth M N and Rostoker N 1962 *Phys. Fluids* **5** 776–88
Showen R L and Kim D M 1978 *J. Geophys. Res.* **83** 623–8

12P-I-08

Proceedings of 1982 International Conference on Plasma Physics,
Goteberg, Sweden

Parametric excitation of upper hybrid side-bands in ionospheric heating experiments

M. C. Lee
Regis College Research Center, Weston, Massachusetts 02193, U.S.A.
S. P. Kuo
Polytechnic Institute of New York, Long Island Center,
Farmingdale, New York 11735, U.S.A

Abstract Upper hybrid side-bands and a purely growing mode can be parametrically excited by an O-mode heater wave. This instability can compete with the parametric decay instability in the ionospheric heating experiments. It may be responsible for the production of the plasma lines at 90° at Boulder, Colorado.

1. Introduction

It has been generally believed that plasma line enhancement at 45° detected by the Arecibo 430 MHz incoherent radar indicates the excitation of parametric decay instability by an O-mode heater wave in the ionosphere (Fejer and Kuo, 1973; Perkins et al., 1974). These enhanced plasma lines are interpreted to result from the scattering of the heater wave and of the parametrically excited Langmuir waves off thermal ion acoustic waves. But much more intense "field-aligned" plasma lines have been observed at Boulder and are characteristic of extremely narrow spectral widths, indicating a different mechanism of producing them (Minkoff and Kreppel, 1976). In this paper, we present a theory suggesting that these field-aligned plasma lines be upper hybrid modes excited parametrically with a purely growing mode by an O-mode heater wave. This parametric instability cannot be excited by an extraordinary heater wave, however.

2. A parametric instability

Near the reflection height of a heater wave, the pump field can be approximately represented by a dipole field $\mathbf{E}_p = \mathcal{E}_p \exp(-i\omega_o t)$, where ω_o is the wave frequency, and $\mathcal{E}_p$ is the field strength. The parametric instability under investigation is expected to produce upper hybrid modes and purely growing (i.e., zero frequency) modes. Since the purely growing mode is involved, the excitation of both the downshifted and upshifted upper hybrid modes have to be considered. The perturbations in physical quantities (e.g., density) due to these modes can be represented respectively by $\delta\tilde{n}_s \exp(\gamma t - ikx)$, $\delta\tilde{n}_1 \exp[-i(kx+\omega t)]$, and $\delta\tilde{n}_2 \exp[i(kx-\omega t)]$, where $\omega = \omega_o + i\gamma$, and γ is the growth rate. A rectangular coordinate system has been so chosen that its z axis coincides with the geomagnetic field $(\underline{B}_o)$ and its x axis with the direction of $\underline{k}$.

The coupled mode equations for exciting upper hybrid waves by scattering the heater wave off the electrostatic density perturbations can be derived from electron continuity equation and momentum equation. They are given by $\tilde{\phi}_1 = A(\delta\tilde{n}_s^*/n_o)$ and $\tilde{\phi}_2 = -A(\delta\tilde{n}_s/n)$ (1)

where $\tilde{\phi}_1(\tilde{\phi}_2)$ is the electrostatic potential of the downshifted (upshifted) upper hybrid waves, $\delta\tilde{n}_s$ is the electron density perturbation due to the excited zero-frequency mode, and $A = (\omega_p^2/k)[(\omega_o + i\nu_e)E_{px} - \Omega_e E_{py}]/(i\omega_o\delta + \nu_e(2\omega_o^2 - \omega_k^2))$, where $\delta = \omega_k^2 + \Omega_e^2 + \nu_e^2 - \omega_o^2$, $\omega_k^2 = \omega_o^2 + 3k^2 v_t^2$; ω_p, Ω_e, ν_e, n_o, and v_t are electron plasma frequency, electron gyrofrequency, electron-ion collision frequency, the background plasma density, and electron thermal velocity respectively.

The other equation relating $\delta\tilde{n}_s$ to $\tilde{\phi}_1$ and $\tilde{\phi}_2$, obtained from electron and ion momentum equations, electron heat equation, and quasi-neutrality approximation, can be shown to be $B(\delta n_s/n_o) = \tilde{\phi}_1^* - C^*\tilde{\phi}_2$ (2)

where $B = (\gamma\nu_e m_i/\nu_e + k^2 c_s^2)(\gamma + 2\nu_e m_e/m_i + k^2 v_t^2 \nu_e/\Omega_e^2) + (2/3)\gamma k^2 c_s^2$ and $C = (2/3)(k^3 e/m_i)(2\nu_e\omega_o/(\omega_o^2 - \Omega_e^2))(\tilde{v}_{px} - i\tilde{v}_{py}\Omega_e/\omega_o) + i\tilde{v}_{px}(k/k_D^2)$, where $\tilde{v}_{px}$ and $\tilde{v}_{py}$ are the perpendicular components of the induced electron velocity in the presence of the heater wave field, $c_s^2 = (T_e + T_i)/m_i$, and $k_D = \omega_p/v_t$. Substituting (1) into (2) leads to the dispersion equation $B = CA^* + c.c$ (3)

3. Threshold and growth rates

For the oblique incidence of O-mode heater waves, the perpendicular components of the heater wave field can be approximately related as $E_{py} = iE_{px}$. The threshold power for the instability can be obtained from (3) as

$$|eE_{px}/m_e|^2_{th} = [v_t^2(m_e/m_i + k^2v_t^2/2\Omega_e^2)(\omega_o(\omega_o-\Omega_e)/\omega_p^2)(\delta^2+\omega_o^2\nu_e^2)][2(\delta(\omega_o+\Omega_e) - \nu_e^2\omega_o)(\omega_o-\Omega_e) - (k^2/k_D^2)\omega_o(\omega_o+\Omega_e)]^{-1}. \quad (4)$$

which leads to the criterion of exciting the instability by an O-mode heater wave, i.e., $\delta > (1/2)(k^2/k_D^2)\omega_o(\omega_o-\Omega_e) + \nu_e^2\omega_o/(\omega_o+\Omega_e)$. (5)

The threshold power has a minimum value at $\delta = \delta_o = \beta + (\beta^2 + \nu_e^2\omega_o^2)^{1/2}$, where $\beta = \nu_e^2 + (k^2/k_D^2)(\omega_o^2/2)$; and the optimum growth rate is found to be $\gamma = -a\nu_e + \nu_e(a^2 + (2k^2 v_t^2 \Omega_e b/\Omega_e^2)(|E_{px}|^2/|E_{px}|^2_{th} - 1))^{1/2}$, where $a = (m_e/m_i) +$ [illegible] $k^2 v_t^2/\Omega_e^2)$ and $b = (m_e/m_i) + (1/2)(k^2 v_t^2/\Omega_e^2)$.

In the case of X-mode heater waves $E_{py} = -iE_{px}$. The threshold power for the instability can be similarly derived as $|eE_{px}/m_e|^2_{th} = 3(v_t^2(\omega_o+\Omega_e)^2/\omega_p^2)(m_e/m_i + k^2v_t^2/2\Omega_e^2)[\nu_e^2(\omega_o^2+\Omega_e^2)^2 + \omega_o^2\delta^2][\delta\omega_o(\omega_o-\Omega_e) - \nu_e^2(\omega_o^2+\Omega_e^2) - (k^2/k_D^2)(\omega_o^4-\Omega_e^4)]^{-1}$ and the criterion of the instability is $\delta > \nu_e^2(\omega_o^2+\Omega_e^2)/(\omega_o(\omega_o-\Omega_e)) + (k^2/k_D^2)(\omega_o^2+\Omega_e^2)(\omega_o+\Omega_e)/\omega_o$. (6)

Note that δ is defined to be $\omega_k^2 + \Omega_e^2 + \nu_e^2 - \omega_o^2$. Near the reflection height of X-mode heater waves, $\omega_o = (1/2)(\Omega_e + (\Omega_e^2 + 4\omega_p^2)^{1/2})$. Therefore, $\delta = k^2 v_t^2 + \nu_e^2 + (1/2)\Omega_e^2 - (\Omega_e/2)(\Omega_e^2 + 4\omega_p^2)^{1/2}$. In the ionospheric F region: $T_e \sim T_i \sim 1000°K$, $m_e/m_i \sim 3.4\times10^{-5}$, $\nu_e \sim 1$ KHz, $\Omega_e/2\pi \sim 1.4$ MHz, $\omega_p/2\pi \sim 6$ MHz, $2\pi/k_D \sim 3\times10^{-3}$ m, δ cannot be positive and the criterion of the instability [(6)] can never be satisfied. Hence, the instability of concern cannot be excited by X-mode heater waves in the ionosphere. In contrast, in the case of O-mode heater waves, it can be shown that $\delta_o \sim \nu_e\omega_o$ and the criterion of the instability [(5)] is well satisfied.

4. Relevant roles in the ionosphere

For $\lambda(=2\pi/k) < 10$ m, the minimum threshold power [(4)] can be approximated as $|eE_{px}/m_e|^2_{min} \approx 2.83\times10^{18}\lambda^{-2}$ and the growth rate as $\gamma \sim 5(|E_{px}|/|E_{px}|_{min} - 1)\lambda^{-2}$. The threshold field strength for exciting the modes with $\lambda = 1$ m is 14 mv/m, which is far below the field strength (a few hundreds of mv/m) of the incident heater wave field, and the corresponding growth rate (time) is ~ 50 sec^{-1} (20 ms) if $|E_{px}|/|E_{px}|_{min}$ is taken to be 10. It is interesting to note that the threshold and the growth rates of these modes are comparable to those of the modes excited by the parametric decay instability. In other words, the parametric instability of interest can compete with parametric decay instability in ionospheric heating. This seems to be supported by observations of the "mini-overshoot" in the measured power of the enhanced plasma lines (Showen and Kim, 1978), which occurs in a few tens of mili-seconds. Much lower threshold field strength (~2 mv/m) is needed to excite modes with $\lambda = 5$ m, and the growth rate (time) is ~2 sec^{-1} (0.5 sec). The excitation of modes with longer wavelengths probably contribute to the "main overshoot" reported by Showen and Kim (1978). For $\lambda > 10$ m, $|eE_{px}/m_e|^2_{min} \sim 3.8\times10^{16}$, which is independent of the wavelength and $\gamma \sim 3.4\times10^{-2}\{[1+5.9\times10^2\lambda^{-2}(|E_{px}|^2/|E_{px}|^2_{min} - 1)]^{1/2} - 1\}$. The threshold field for exciting the modes of, say, 50 m is ~0.8 mv/m and the growth rate (time) is ~0.13 sec^{-1} (7.5 sec). Our proposed instability may be responsible for the plasma line enhancement at 90° and may also contribute to the production of field-aligned ionospheric irregularities with scale sizes ranging from meters to hundreds of meters in ionospheric heating experiments.

References

Fejer, J.A. and Y.Y. Kuo (1973), AGARD Conf. Proc., 138, 11-1.

Minkoff, J. and R. Kreppel (1976), J. Geophys. Res., 81, 2844.

Perkins, F.W., C. Oberman and E.J. Valeo (1974), J. Geophys. Res., 79, 1478.

Showen, R.L. and D.M Kim (1978), J. Geophys. Res., 83, 628.

Acknowledgements This work was supported by AFGL contract F 19628-80C-0016 at Regis College Research Center and in part by NSF grant ATM-8008296 at Polytechnic Institute of New York.

Proceedings of 1982 International Conference on Plasma Physics,
Goteberg, Sweden

Generation of field-aligned irregularities in the ionosphere by a parametric decay process

S. P. Kuo
Polytechnic Institute of New York, Long Island Center,
Farmingdale, New York 11735, U.S.A.
M. C. Lee
Regis College Research Center, Weston, Massachusetts 02193, U.S.A.
B. R. Cheo
Polytechnic Institute of New York, Long Island Center,
Farmingdale, New York 11735, U.S.A.

Abstract. A parametric decay instability, which involves four wave interaction with an electrostatic pump, is proposed as a process of producing both the large- and the short-scale irregularities in the ionospheric heating experiments. It can explain the detection of discrete rather than continuous spectra of large-scale irregularities in the experiments.

1. Introduction

The generation of field-aligned ionospheric irregularities was one of the unexpected modification effects due to ionospheric heating. The field-aligned structure with scale lengths of hundreds of meters or larger is associated with the occurrence of artificial spread F, while that with scale lengths of meters or shorter is responsible for the creation of strong HF through UHF backscatter radar cross sections. The identification of possible mechanisms has stimulated a flurry of theoretical investigation. Thermal self-focusing instability (Perkins and Valeo, 1974; Cragin and Fejer, 1974) has been generally believed to be the cause of those large-scale irregularities. However, discrete rather than continuous spectra of irregularities as predicted by the theories were detected by the radar beams scanned rapidly across the modified region in the ionosphere (Duncan and Behnke, 1978). The causes of short-scale irregularities seem to be very complicated and many possibilities have been indicated (Inhester et. al., 1981 and references therein). In this paper, we investigate the parametric decay process of O-mode heater waves in the ionosphere and show that it may be an efficient process of producing field-aligned irregularities with a broad range of scales from meters to kilometers.

2. Source of pump waves

O-mode heater waves can excite parametrically a Langmuir wave and an ion-acoustic wave near its reflection height in the ionosphere. A saturated spectrum of Langmuir waves is expected theoretically to be formed via the nonlinear ion Landau damping. The occurrence of such a parametric decay process has been strongly indicated by the plasma line enhancement observed at Arecibo. These excited Langmuir waves have already been considered as the potential source of generating the short-scale irregularities (Perkins, 1974; Lee and Fejer, 1978). Along the same line, we investigate four-wave other than the three-wave interaction discussed by Perkins (1974) as the mechanism of causing the induced ionospheric irregularities in the ionospheric heating experiments.

Langmuir waves excited by O-mode heater waves are used as the pump to initiate another parametric instability, through which upshifted and downshifted decay bands and a purely growing decay mode are produced. The matching wave-vector and wave frequency relations for this instability are $\underline{k}_1=\underline{k}_2+\underline{k}_3=\underline{k}_0-\underline{k}_3$, $\omega_0=\omega_2=\omega_1=\omega, \omega_3=0$, where the subscript "1" stands for the Langmuir pump, "0" and "2" for the upshifted and downshifted decay bands, respectively, and "3" for the purely growing decay mode. The basic equations employed in our analysis of the problem include electron and ion continuity equations, electron and ion momentum equations, and electron heat equation. For simplicity, a rectangular system of coordinates is so chosen that all the wave vectors lie on the x-z plane. The Langmuir pump is assumed to be along the geomagnetic field line, which coincides with the z axis. It is a tedious but straightforward procedure to formulate the coupling mode equation for the purely growing mode and the coupled mode equations for the upshifted and downshifted decay modes. Solving these equations will lead to the dispersion relation for the instability of interest. It is

$$\{(\gamma\Omega_e\Omega_i/\nu_e+k_3^2c_s^2)B+(2/3)\gamma(m_e/m_i)k_3^2v_t^2\} = 2(m_e/m_i)(e/m_e)^2\phi_1^2\{k_1^4k_3^4/k_1^2+k_3^2)^{-1}\}\{(4/3)\nu_e(\omega^2-\Omega_e^2)\omega^{-2}[\Omega_e^2(k_1^2+k_3^2)^{-1}+(5/2)v_t^2]\}\{[k_3^2\Omega_e^2(k_1^2+k_3^2)^{-1}+3v_t^2k_3^2+2\nu_e^2]+(\omega^2-\Omega_e^2)^2(\nu_e^2/\omega^2)\}^{-1} \qquad (1)$$

where $B = \gamma+2\nu_e(m_e/m_i)$; $\phi_1, \gamma, \Omega, \nu_e, c_s, m$, and v_t are the electric potential of the pump field, growth rate, gyrofrequency, electron-ion collision frequency, ion-acoustic velocity, mass of the charged particles, and electron thermal velocity respectively.

3. Excitation of field-aligned irregularities

Setting $\gamma = 0$ in (1) gives the threshold field ($|E_1| = |k_1\phi_1|$): $|eE_1/m_e|^2_{th}$

$$= (3/8)c_s^2(k_1^2+k_3^2)k_1^{-2}k_3^{-2}\omega^2(\omega^2-\Omega_e^2)^{-2}[2+(m_i/m_e)k_3^2v_t^2\Omega_e^{-2}]\{[k_3^2\Omega_e^2(k_1^2+k_3^2)^{-1}+3v_t^2k_3^2+2\nu_e^2]^2+(\omega^2-\Omega_e^2)(\nu_e^2/\omega^2)\}[\Omega_e^2(k_1^2+k_3^2)^{-1}+(5/2)v_t^2]^{-1} \qquad (2)$$

The growth rate can be shown to be

$$\gamma = -\nu_e[m_e/m_i+(11/6)k_3^2v_t^2/\Omega_e^2]+\{\nu_e^2[m_e/m_i+(11/6)k_3^2v_t^2/\Omega_e^2]^2+2(m_e/m_i)(\nu_e/\Omega_e)^2k_3^2v_t^2[2+(m_i/m_e)k_3^2v_t^2/\Omega_e^2](|E_1|^2/|E_1|^2_{th}-1)\}^{1/2} \qquad (3)$$

These expressions can be much simplified analytically for the excitation of short- and large-scale irregularities: (1) for $(1/2)(m_i/m_e)k_3^2v_t^2/\Omega_e^2 \gg 1$, i.e., $\lambda_3<10$ m if the following ionospheric parameters are used: $m_i/m_e\sim 2.94\times10^4$, $v_t\sim10^5$(m/sec), $\Omega_e/2\pi\sim1.4$ MHz. The threshold field and the growth rate can be expressed approximately as $|E_1|_{th}\sim 0.187\lambda_3^{-2}(v/m)\sim 21$(mv/m) and $\gamma\sim 1.24\{[|E_1|^2/|E_1|^2_{th}+0.69]^{1/2}-1.3\}\lambda_3^{-2}\sim 4.4$(sec^{-1}) for $\lambda_3 = 3$ m. The threshold field required for exciting the short-scale irregularities is quite small compared with the Langmuir field (say, 0.7(v/m)); (2) for $(11/6)(m_i/m_e)k_3^2v_t^2\Omega_e^{-2} \ll 1$, i.e., $\lambda_3 \gg 30$ m Then, $|E_1|_{th}\sim 6.2\times10^{-2}\lambda_3(mv/m)\sim 31$(mv/m) and $\gamma\sim 3.3\times10^{-2}\{[1+1.05\times10^3\lambda_3^{-2}(|E_1|^2/|E_1|^2_{th}-1)]^{1/2}-1\}(sec^{-1})\sim 2.5\times10^{-2}$(sec^{-1}).

Our proposed mechanism predicts that in the case of exciting large-scale irregularities, less threshold fields are required for modes with smaller scale sizes. Moreover, modes with smaller scale sizes have larger growth rates. This may explain the detection of discrete rather than continuous spectra in the Duncan and Behnke's experiments. It should be stressed that the instability of concern can generate both the short- and large-scale irregularities. This instability may contribute additively to the excitation of ionospheric irregularities with other mechanisms discussed in the literature. Since either O- or X-mode heater waves can also generate large-scale irregularities via the self-focusing instability, but the instability discussed in this paper can only be excited by O-mode heater waves, we expect that more intense large-scale irregularities can be produced by O-mode than by X-mode heater waves. This prediction can be tested by, for example, radio Star or satellite scintillation measurements.

References

Cragin, B.L. and J.A. Fejer (1974), Radio Sci., 9, 1071.
Duncan, L.M. and R.A. Behnke (1978), Phys. Rev. Lett., 41, 998.
Inhester, B., A.C. Das, and J.A. Fejer (1981), J. Geophys. Res., 86, 9101.
Lee, M.C. and J.A. Fejer (1978), Radio Sci., 13, 893.
Perkins, F.W. (1974), Radio Sci., 9, 1065.
Perkins, F.W. and E.J. Valeo (1974), Phys. Rev. Lett., 32, 1234.

Acknowledgments. This work was supported in part by NSF grant ATM-8008296 at Polytechnic Institute of New York and by AFGL contract F 19628-80-C-0016 at Regis College Research Center.

ON THE PARAMETRIC EXCITATION OF PLASMA MODES AT UPPER HYBRID RESONANCE

S.P. KUO
Polytechnic Institute of New York, Long Island Center, Farmingdale, NY 11735, USA

and

M.C. LEE
Regis College Research Center, Weston, MA 02193, USA

Received 15 March 1982
Revised manuscript received 5 July 1982

The conditions for the upper hybrid modes to be excited parametrically by an intense electromagnetic wave near its cut-off have been examined. They show that upper hybrid side-bands can easily be produced in the ionosphere by an obliquely incident wave of ordinary but not extraordinary polarization.

Lee [1] has shown that upper hybrid and diffusion modes can be excited parametrically by an extraordinary pump wave. The criterion of the instability is $\nu_c\omega_0 \gg \Omega_e^2 + \nu_c^2$, where ω_0, Ω_e, and ν_c are pump wave frequency, electron gyrofrequency, and electron–ion collision frequency, respectively. However, this criterion cannot be satisfied in either laboratory plasma or space plasma. We show in this letter that upshifted and downshifted upper hybrid modes can be excited concurrently with a purely growing mode by an obliquely incident ordinary wave transmitted into the ionosphere from the ground. The established criterion prohibits the excitation of these plasma modes by an extraordinary wave.

The process under consideration is a parametric instability which occurs near the cutoff of electromagnetic waves in magnetized plasmas. A monochromic dipole pump field, $\boldsymbol{E}_p = \boldsymbol{\varepsilon}_p \exp(-i\omega_0 t)$, can be reasonably assumed. Let the parametrically excited purely growing (i.e., zero frequency) mode take the form of $\exp(\gamma t - ikx)$, where a positive value of γ represents the growth rate of the instability. The wave vector ($\boldsymbol{k}$) of this mode is taken to be along the x axis of a rectangular system of coordinates. The z axis coincides with the imposed dc magnetic field ($\boldsymbol{B}_0$). Then, the excited upshifted and downshifted upper hybrid modes can be represented by $\exp[-i(kx + \omega t)]$ and $\exp[i(kx - \omega t)]$ respectively, where $\omega = \omega_0 + i\gamma$.

The mode-coupling equation for exciting the upper hybrid waves by scattering the pump waves off the electrostatic density perturbations can be obtained from electron continuity equation and momentum equation. It is given by

$$\left[\left(\frac{\partial}{\partial t} + \nu_c\right)\left(\frac{\partial^2}{\partial t^2} + \nu_c \frac{\partial}{\partial t} + \omega_{pe}^2 - v_t \nabla_\perp^2\right) + \Omega_e^2 \frac{\partial}{\partial t}\right]\nabla_\perp^2 \phi_1$$
$$= \omega_{pe}^2\left[\left(\frac{\partial}{\partial t} + \nu_c\right)\nabla_\perp \cdot \left(\boldsymbol{E}_p \frac{\delta n_s}{n_0}\right) - \Omega_e \nabla_\perp \cdot \left(\boldsymbol{E}_p x \hat{z} \frac{\delta n_s}{n_0}\right)\right], \tag{1}$$

where ϕ_l is the electrostatic potential of the upper hybrid modes, δn_s is the electron density perturbation due to the excited zero-frequency mode, v_t is the electron thermal velocity, ω_{pe} is the electron plasma frequency, and $\nabla_\perp = \hat{x}\partial/\partial x + \hat{y}\partial/\partial y$. In obtaining (1), the approximation of uniform medium has been made. Substituting $\phi_1 = \tilde{\phi}_1 \exp[i(kx - \omega t)]$, $\phi_2 = \tilde{\phi}_2 \exp[-i(kx + \omega t)]$, $\delta n_s = \delta\tilde{n}_s \exp(\gamma t - ikx)$, and $\boldsymbol{E}_p = \boldsymbol{\varepsilon}_p \exp(-i\omega_0 t)$ into equation (1) leads to

$$\tilde{\phi}_1 = A(\delta\tilde{n}_s^*/n_0), \quad \tilde{\phi}_2 = -A(\delta\tilde{n}_s/n_0), \tag{2}$$

where

0 031-9163/82/0000–0000/$02.75 © 1982 North-Holland

$$A = \frac{\omega_{pe}^2}{k} \frac{(\omega_0 + i\nu_e)\epsilon_{px} - i\Omega_e\epsilon_{py}}{i\omega_0\sigma + \nu_e(2\omega_0^2 - \omega_{ek}^2)} ,$$

where $\sigma = \omega_{ek}^2 + \Omega_e^2 + \nu_e^2 - \omega_0^2$ and $\omega_{ek}^2 = \omega_{pe}^2 + 3k^2v_t^2$; the subscripts 1 and 2 designate the downshifted and upshifted upper hybrid modes respectively. $\gamma \ll \omega_0, \nu_e$ has been assumed in obtaining (2).

The other equation relating $\delta\tilde{n}_s$ to ϕ_l, derived from electron and ion momentum equations, electron heat equation, and quasi-neutrality approximation, can be shown to be

$$B(\delta\tilde{n}_s/n_0) = c\tilde{\phi}_1^* - c^*\tilde{\phi}_2 , \qquad (3)$$

where

$$B = (\gamma\Omega_e\Omega_i/\nu_e + k^2c_s^2)(\gamma + 2\nu_e m_e/m_i + k^2v_t^2\nu_e/\Omega_e^2) + \tfrac{2}{3}\gamma k^2c_s^2 ,$$

$$C = \tfrac{2}{3}(k^3e/m_i)[2\nu_e\omega_0/(\omega_0^2 - \Omega_e^2)](\tilde{v}_{px} - i\tilde{v}_{py}\Omega_e/\omega_0) - i\tilde{v}_{px}(k^2/k_D^2) ,$$

where $\tilde{v}_{px}$ and $\tilde{v}_{py}$ are the penpendicular components of the induced electron velocity in the presence of pump field; m_e, m_i, c_s, Ω_i, and $2\pi/k_D$ are electron mass, ion mass, ion-acoustic velocity, ion gyrofrequency, and Debye length, respectively. In the case of our interest, $\omega_0 > \Omega_e$ and $k^2/k_D^2 \ll 1$ are assumed. Substituting (2) into (3) yields

$$B = CA^* + C^*A . \qquad (4)$$

For the oblique incidence of ordinary pump waves, the perpendicular components of the pump field are approximately related as $\epsilon_{py} = -i\epsilon_{px}$. The induced electron velocity is, then, given by $\tilde{v}_{px} = -ie\epsilon_{px}/[m_e(\omega_0 - \Omega_e)]$ and $\tilde{v}_{py} = e\epsilon_{px}/[m_e(\omega_0 - \Omega_e)]$. (4) can be, therefore, written as

$$B \approx \alpha_0|e\epsilon_{px}/m_e|^2\{2[\sigma(\omega_0 + \Omega_e) - \nu_e^2\omega_0]/(\omega_0 - \Omega_e) - (k^2/k_D^2)\omega_0(\omega_0 + \Omega_e)\}(\nu_e^2\omega_0^2 + \sigma^2)^{-1} \qquad (5)$$

after the substitution of these expressions into it, where

$$\alpha_0 = \tfrac{4}{3}(m_e/m_i)[k^2\nu_e/\omega_0(\omega_0 - \Omega_e)] .$$

The threshold power for exciting the instability is determined by setting $\gamma = 0$ in (5), namely,

$$|e\epsilon_{px}/m_e|_{th}^2 = 3v_t^2(m_e/m_i + k^2v_t^2/2\Omega_e^2) \times [\omega_0(\omega_0 - \Omega_e)/\omega_{pe}^2](\sigma^2 + \nu_e^2\omega_0^2) \times \{2[\sigma(\omega_0 + \Omega_e) - \nu_e^2\omega_0]/(\omega_0 - \Omega_e) - (k^2/k_D^2)\omega_0(\omega_0 + \Omega_e)\}^{-1} . \qquad (6)$$

Since the RHS of (6) must be positive, it requires that

$$\sigma > \tfrac{1}{2}(k^2/k_D^2)\omega_0(\omega_0 - \Omega_e) + \nu_e^2\omega_0/(\omega_0 + \Omega_e) . \qquad (7)$$

Inequality (7) is the condition for the instability of concern to be excited by an ordinary pump wave in magnetized plasmas (e.g., the ionosphere). If the pump wave frequency is large compared with the electron gyrofrequency, (7) can be simplified to be

$$\sigma > \nu_e^2 + \tfrac{1}{2}(k^2/k_D^2)\omega_0^2 . \qquad (8)$$

The threshold power has a minimum value at $\sigma = \sigma_0 = \beta + (\beta^2 + \nu_e^2\omega_0^2)^{1/2}$, where $\beta = \nu_e^2 + (k^2/k_D^2)(\omega_0^2/2)$. Solving (5) gives the growth rate of the instability. It is

$$\gamma = -a\nu_e + \nu_e[a^2 + (2k^2v_t^2\nu_e b/\Omega_e^2) \times (|\epsilon_{px}|^2/|\epsilon_{px}|_{th}^2 - 1)]^{1/2} , \qquad (9)$$

where

$$a = (m_e/m_i) + \tfrac{11}{6}(k^2v_t^2/\Omega_e^2) ,$$

$$b = (m_e/m_i) + \tfrac{1}{2}(k^2v_i^2/\Omega_e^2) .$$

The typical ionospheric parameters in the F region are: $\nu_e \approx 1$ kHz, $\Omega_e/2\pi \approx 1.4$ MHz, $T_e \approx T_i \approx 1000$ K, $m_e/m_i \approx 3.4 \times 10^{-5}$, $\omega_{pe}/2\pi \approx 6$ MHz, $2\pi/k_D \approx 3 \times 10^{-3}$ m. Let us investigate the possibility of exciting upper hybrid modes with the wavelength of, say, 3 m in the ionosphere by an HF (say, 6 MHz) ordinary pump wave. It is seen that $\sigma_0 \sim \nu_e\omega_0$ and the condition for the instability [eq. (7) or (8)] can be well satisfied. The required minimum field intensity can be estimated from (6). It is about 3.2 (mV/m). The corresponding growth rate is 1.8 s^{-1} if $|\epsilon_{px}|^2/|\epsilon_{px}|_{min}^2 \approx 10^4$ is assumed. This threshold field intensity is far below that (a few hundreds of mV/m) employed in the ionospheric heating experiments performed at, for example, Boulder and Puerto Rico. Therefore, upper hybrid modes can be easily produced by ordinary pump waves in the ionosphere. The comparison between the predictions and the relevant observations in the experiments will be published elsewhere.

In the case of the extraordinary pump wave, $\epsilon_{py} = i\epsilon_{px}$. The extraordinary mode tends to propagate along the geomagnetic field near its cutoff [2] and almost becomes a right-hand circularly polarized wave. The induced electron velocity can be shown to be $\tilde{v}_{px} = -ie\epsilon_{px}/[m_e(\omega_0 + \Omega_e)]$ and $\tilde{v}_{py} = -e\epsilon_{px}/[m_e(\omega_0 + \Omega_e)]$. The threshold power for exciting the instability by an extraordinary pump wave can be similarly derived as

$$|e\epsilon_{px}/m_e|^2_{th} = \tfrac{3}{2}\,[v_t^2(\omega_0 + \Omega_e)^2/\omega_p^2] \\ \times (m_e/m_i + k^2 v_t^2/2\Omega_e^2)\{\nu_e^2(\omega_0^2 + \Omega_e^2)^2 + \omega_0^2\sigma^2\} \\ \times \{\sigma\omega_0(\omega_0 - \Omega_e) - \nu_e^2(\omega_0^2 + \Omega_e^2) \\ - (k^2/k_D^2)(\omega_0^4 - \Omega_e^4)\}^{-1} . \qquad (10)$$

For the instability to occur, it requires that

$$\sigma > \nu_e^2(\omega_0^2 + \Omega_e^2)/\omega_0(\omega_0 - \Omega_e) \\ + (k^2/k_D^2)(\omega_0^2 + \Omega_e^2)(\omega_0 + \Omega_e)/\omega_0 . \qquad (11)$$

Near the cutoff of the extraordinary waves in the ionosphere,

$$\omega_0 = \Omega_e/2 + \tfrac{1}{2}(\Omega_e^2 + 4\omega_{pe}^2)^{1/2} .$$

Note that $\sigma = \omega_{ek}^2 + \Omega_e^2 + \nu_e^2 - \omega_0^2$. Therefore,

$$\sigma = \tfrac{1}{2}\Omega_e^2 + k^2 v_t^2 + \nu_e^2 - (\Omega_e/2)(\Omega_e^2 + 4\omega_{pe}^2)^{1/2} ,$$

which can never be positive in the ionosphere. Thus, we may conclude that upper hybrid modes cannot be excited in the ionosphere by an HF pump wave of extraordinary polarization transmitted from the ground. However, the accessibility of the extraordinary pump wave to the upper hybrid resonance zone is possible, if the wave is incident upon the plasmas from either the higher density side or the higher magnetic field side. The typical example for the former case is the incidence of the wave from the topside of the ionosphere. The latter case is achievable in the laboratory (e.g., ref. [3]), the inhomogeneous magnetic field can be generated in the magnetic fusion devices, e.g., Tokamaks.

In addition to the criterion for the parametric excitation of upper hybrid modes in the ionosphere, there are some new approaches in our work, which lead to different results in comparison with the previous relevant studies (e.g., refs. [4–8]). Since the excited low frequency modes are purely growing modes, four wave interaction (i.e., pump wave, up-shifted and down-shifted excited high-frequency modes purely growing mode) should be analyzed as described in this paper. Except Dimant's work [4], only three-wave interaction was considered before. Moreover, a new nonlinear effect, viz., a nonoscillatory beating current is included in our analyses. This beating current at zero frequency is driven by pump wave in the oscillatory electron density perturbations of the excited high-frequency waves. It tends to compensate part of the well-known nonlinear effects, i.e., the ponderomotive force and the differential Ohmic heating. This new nonlinear effect not considerd in the previous work leads to a marked difference between our results and, e.g., Dimant's [4] in the threshold fields and the growth rates of the excited instabilities. Finally we should point out that the present work is restricted to a uniform medium. The restriction of our results as applied to the ionospheric heating experiments will be discussed elsewhere.

We thank the two referees' comments which draw our attention to the interesting work in the previous relevant studies. This work was supported in part by NSF under grant number ATM-8008296 at Polytechnic Institute of New York and by AFGL contract F19628-80-C-0016 at Regis College Research Center.

References

[1] K.F. Lee, Phys. Lett. 36A (1974) 257.

[2] W.F. Utlaut and R. Cohen, Science 174 (1971) 245.

[3] M. Porkolab and M.V. Goldman, Phys. Fluids 19 (1976) 872.

[4] Y.S. Dimant, Radiophys. Quantum Electron. 20 (1977) 1259.

[5] V.V. Vaskov and A.V. Gurevich, Sov. Phys. JETP 46 (1977) 487.

[6] A.C. Das and J.A. Fejer, J. Geophys. Res. 84 (1979) 6701.

[7] A.G. Litvak and G.A. Mironov, Sov. Phys. JETP 51 (1980) 282.

[8] T.M. Burinskaya and A.S. Volokitin, Physica 2D (1981) 117.

JOURNAL OF GEOPHYSICAL RESEARCH, VOL. 88, NO. A1, PAGES 417–423, JANUARY 1, 1983

The Role of Parametric Decay Instabilities in Generating Ionospheric Irregularities

S. P. KUO AND B. R. CHEO

Polytechnic Institute of New York, Long Island Center, Farmingdale, New York 11735

M. C. LEE

Regis College Research Center, Weston, Massachusetts 02193

We show that purely growing instabilities driven by the saturation spectrum of parametric decay instabilities can produce a broad spectrum of ionospheric irregularities. The threshold field $|E_{th}|$ of the instabilities decreases with the scale lengths λ of the ionospheric irregularities as $|E_{th}| \propto \lambda^{-2}$ in the small-scale range (<15 m) but becomes an increasing function as $|E_{th}| \propto \lambda$ in the large-scale range. The minimum threshold field (~ 2 mV/m) occurs at $\lambda \sim 20$ m. The growth rate γ of the instabilities maximizes at $\lambda \sim 6$ m and decreases drastically as $\gamma \propto \lambda^{-2}$ with scale lengths larger than a few kilometers. The excitation of kilometer-scale irregularities is strictly restricted by the instabilities themselves and by the spatial inhomogeneity of the medium. These results are drawn from the analyses of four-wave interaction. Ion-neutral collisions impose no net effect on the instabilities when the excited ionospheric irregularities have a field-aligned nature.

1. INTRODUCTION

Parametric decay instabilities are expected to be excited by O mode heater waves in ionospheric heating experiments [*Perkins and Kaw*, 1971]. A saturation spectrum of Langmuir waves within a small cone around the geomagnetic field can be produced by these instabilities via cascading processes and nonlinear ion Landau damping [e.g., *Fejer and Kuo*, 1973*a*; *Perkins et al.*, 1974]. Although experimental spectra of such Langmuir waves are still not available, it has been generally believed that plasma line enhancement observed at Arecibo [*Carlson et al.*, 1972] is the evidence of the excitation of parametric decay instabilities. Based on the theoretical spectra of parametric decay instabilities, plasma line enhancement at Arecibo can be successfully reproduced [*Fejer and Kuo*, 1973*b*; *Perkins et al.*, 1974].

The relevant roles of parametric decay instabilities in causing other unexpected modification effects due to ionospheric heating have been actively explored, such as 6300-Å airglow enhancement [*Fejer and Graham*, 1974; *Weinstock*, 1974; *Nicholson*, 1977], the generation of short-scale field-aligned ionospheric irregularities [*Perkins*, 1974; *Lee and Fejer*, 1978], the possible formation of a soliton and its collapse [*Weatherall et al.*, 1982], etc. However, parametric decay instabilities do not seem to be the only cause leading to the generation of short-scale irregularities. Their dominant role is questioned in particular by the discovery of the overshoot phenomenon of plasma line intensity at Arecibo [*Showen and Kim*, 1978]. Other competitive mechanisms have been suggested with continuing effort [e.g., *Das and Fejer*, 1979; *Inhester et al.*, 1981 and references therein; *Lee and Kuo*, 1982]. The excitation of ionospheric irregularities by powerful HF radio waves is probably a gross effect contributed additively by different mechanisms.

The purpose of this paper is to investigate the generation of ionospheric irregularities by the saturated spectrum of parametric decay instabilities via purely growing instabilities [*Perkins*, 1974]. In his study of three-wave interaction, *Perkins* [1974] has already commented on the importance of four-wave interaction for exciting purely growing modes. In this paper we analyze a process of four-wave interaction including beating current in addition to differential ohmic heating and nonlinear Lorentz forces as the nonlinear effects for purely growing modes. The mechanism for the generation of field-aligned ionospheric irregularities is the filamentation instability of Langmuir waves. The beating current at zero frequency is the nonoscillatory part of the current driven by the total high-frequency fields on the total high-frequency density perturbations. It appears in the electron continuity equation. The differential ohmic heating force is the hydrodynamic expansion force of electron gas caused by the wave-induced heating. It appears as an additional pressure gradient term in the electron momentum equation. The nonlinear Lorentz force is derived from the convective term of the electron momentum equation and is reduced to the ponderomotive force in the unmagnetized plasma case. It will be seen that the differential ohmic heating force predominates over the ponderomotive force in the consideration of present interest, in contrast to other cases, e.g., type III solar radio bursts [*Bardwell and Goldman*, 1976; *Weatherall et al.*, 1981], where ponderomotive force is the dominant nonlinear effect.

The plan of this paper is as follows. The excitation of parametric decay instabilities by O mode heater waves is briefly described in section 2. In section 3, purely growing instabilities driven by the saturation spectrum of parametric decay instabilities are analyzed in spatially uniform plasmas. The uniform medium theory is justified by the result that large-scale (kilometers) ionospheric irregularities cannot be excited favorably by the purely growing instabilities. The influence of spatial inhomogeneity on the generation of ionospheric irregularities is discussed in section 4, and conclusions are finally drawn.

2. PARAMETRIC DECAY INSTABILITIES

An O mode heater wave can decay into one Langmuir wave and one ion acoustic wave near its reflection height in

Paper number 2A1487.
0148-0227/83/002A-1487$05.00

the ionosphere. After the excited Langmuir wave grows and acquires a sufficiently large intensity, it can decay into a daughter Langmuir wave and an ion acoustic wave. A cascade to lower-frequency Langmuir waves proceeds and finally results in a saturation spectrum of Langmuir waves [*Fejer and Kuo*, 1973*a*; *Perkins et al.*, 1974] whose distribution in wave vector space is confined in a narrow cone around the axis taken along the geomagnetic field.

These parametrically excited Langmuir waves are now considered as pump waves to excite ionospheric irregularities (purely growing modes) and wave vector up-shifted and down-shifted daughter Langmuir waves. The process under consideration can be represented by the following matching relations:

$$\omega_3 = 0 \qquad \omega_1 = \omega_2 = \omega_0$$
$$\mathbf{k}_2 = \mathbf{k}_3 + \mathbf{k}_1 \qquad \mathbf{k}_1 = \mathbf{k}_3 + \mathbf{k}_0 \tag{1}$$

where 0, 1, 2, and 3 are used to represent respectively the down-shifted daughter Langmuir wave, the Langmuir pump wave, the up-shifted daughter Langmuir wave, and the purely growing mode (ionospheric irregularities).

To begin with our analyses, the Langmuir pump waves $(\omega_1, \mathbf{k}_1)$ are represented approximately by the following dispersion relation:

$$1 - \frac{\omega_p^2}{k_1^2}\left[\left(\frac{k_{1x}^2}{\omega_1^2 - \Omega_e^2} + \frac{k_{1z}^2}{\omega_1^2}\right)\left(1 + \frac{3k_1^2}{k_D^2}\right)\right] = 0 \tag{2}$$

where ω_p, k_D, and Ω_e are electron plasma frequency, electron Debye length, and electron gyrofrequency respectively. A Cartesian system of coordinates is chosen with its z axis along the geomagnetic field, and the wave vectors lie on the x-z plane. Since no damping term is included in (2), unattenuated Langmuir pump waves have been assumed. This is because the Langmuir pump waves with saturated intensities are maintained by CW O mode heater waves. For simplicity, the Langmuir pump waves are assumed to be not depleted. In fact, the process discussed in section 3 can modify the saturation spectrum of Langmuir waves determined by, for example, cascading processes or nonlinear ion Landau damping and can be viewed as a saturation mechanism of the parametric decay instability. Therefore the effect of pump depletion should, in general, be considered in the following analyses. However, this is beyond the scope of the present work.

3. PURELY GROWING INSTABILITIES EXCITED BY LANGMUIR PUMP WAVES

The coupled mode equations for daughter Langmuir waves $(\omega_0, \mathbf{k}_0; \omega_2, \mathbf{k}_2)$ in terms of Langmuir pump waves $(\omega_1, \mathbf{k}_1)$ and ionospheric irregularities $(\omega_3, \mathbf{k}_3)$ can be derived from the electron continuity equation and electron momentum equation as

$$\left[\frac{\partial}{\partial t}\left(\frac{\partial}{\partial t} + \nu_e\right)^3 + \omega_{k2}^2\left(\frac{\partial}{\partial t} + \nu_e\right)^2 + \Omega_e^2\,\frac{\partial}{\partial t}\left(\frac{\partial}{\partial t} + \nu_e\right)\right.$$
$$\left. + \left(\frac{k_{2z}}{k_2}\right)^2\Omega_e^2\omega_{k2}^2\right]\Phi_2 = -\left(\frac{\omega_p^2}{k_2^2}\right)\left[\left(\frac{\partial}{\partial t} + \nu_e\right)^2(\mathbf{k}_1\cdot\mathbf{k}_2)\right.$$
$$\left. + \Omega_e^2 k_{2z}k_{1z}\right]\Phi_1\left(\frac{\delta n}{n_0}\right) \tag{3}$$

$$\left[\frac{\partial}{\partial t}\left(\frac{\partial}{\partial t} + \nu_e\right)^3 + \omega_{k0}^2\left(\frac{\partial}{\partial t} + \nu_e\right)^2 + \Omega_e^2\,\frac{\partial}{\partial t}\left(\frac{\partial}{\partial t} + \nu_e\right)\right.$$
$$\left. + \left(\frac{k_{0z}}{k_0}\right)^2\Omega_e^2\omega_{k0}^2\right]\Phi_0 = -\left(\frac{\omega_p^2}{k_0^2}\right)\left[\left(\frac{\partial}{\partial t} + \nu_e\right)^2(\mathbf{k}_1\cdot\mathbf{k}_0)\right.$$
$$\left. + \Omega_e^2 k_{0z}k_{1z}\right]\Phi_1\left(\frac{\delta n^*}{n_0}\right) \tag{4}$$

where Φ_1, Φ_2, and Φ_0 are electrical potentials of the Langmuir pump wave, up-shifted daughter Langmuir wave, and down-shifted daughter Langmuir wave; n_0, δn, and ν_e are unperturbed electron density, induced nonoscillatory electron density perturbations, and electron-ion collision frequency respectively; the superscript asterisk is used to indicate complex conjugate; and $\omega_{kj}^2 = \omega_p^2(1 + 3k_j^2/k_D^2)$, $j = 0, 2$, where k_D is the Debye wave number. In obtaining (3) and (4), uniform background density n_0 has been assumed.

The other coupled mode equation can be obtained from the following fluid equations for electrons and ions:

$$\frac{\partial}{\partial t}n_e + \nabla\cdot n_e\mathbf{V}_e = 0 \tag{5}$$

$$m\left(\frac{\partial}{\partial t} + \mathbf{V}_e\cdot\nabla\right)\mathbf{V}_e = -\frac{\nabla p_e}{n_e} - e\mathbf{E} - m\Omega_e\mathbf{V}_e\times\hat{z}$$
$$- \nu_e m(\mathbf{V}_e - \mathbf{V}_i) \tag{6}$$

$$\frac{\partial}{\partial t}T_e + \tfrac{2}{3}T_0\nabla\cdot\mathbf{V}_e = \frac{2}{3n_e}\nabla\cdot(R_\parallel^e + R_\perp^e\,\nabla_\perp)T_e$$
$$- 2\nu_e\frac{m}{M}(T_e - T_0) + \tfrac{2}{3}\nu_e m\,\langle V_e^2\rangle \tag{7}$$

$$\frac{\partial}{\partial t}n_i + \nabla\cdot n_i\mathbf{V}_i = 0 \tag{8}$$

$$M\left(\frac{\partial}{\partial t} + \mathbf{V}_i\cdot\nabla\right)\mathbf{V}_i = -\frac{\nabla p_i}{n_i} + e\mathbf{E} + M\Omega_i\mathbf{V}_i\times\hat{z}$$
$$+ \nu_e m\frac{n_e}{n_i}(\mathbf{V}_e - V_i) - \nu_{in}M\mathbf{V}_i \tag{9}$$

where

$$R_\parallel^e = \tfrac{5}{2}(n_0T_0/m\nu_e)$$
$$R_\perp^e = \tfrac{5}{2}(\nu_e/\Omega_e)^2(n_0T_0/m\nu_e)$$

and where m and M are the masses of electrons and ions; n, V, T, Ω, and P are their density, velocity, temperature, gyrofrequency, and thermal pressure; T_0 is the plasma temperature (measured by electron volts) in thermal equilibrium; ν_{in} is the ion-neutral collision frequency; and the angle brackets in (7) mean the time average taken over a few high-frequency periods.

According to the matching relations given by (1), waves '0,' '1,' '2,' and '3' may be designated respectively by

$$\delta\varphi_0\exp[i(\mathbf{k}_0\cdot\mathbf{r} - \omega t)] \qquad \delta\varphi_1\exp[i(\mathbf{k}_1\cdot\mathbf{r} - \omega t)]$$
$$\delta\varphi_2\exp[i(\mathbf{k}_2\cdot\mathbf{r} - \omega t)] \qquad \delta\varphi_3\exp(\gamma t + i\mathbf{k}_3\cdot\mathbf{r})$$

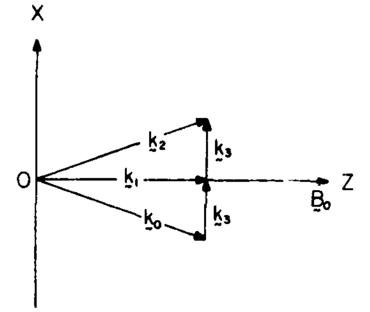

Fig. 1. Configuration of four-wave interaction. Langmuir pump wave ($\mathbf{k}_1$) propagating along the geomagnetic field excites a down shifted daughter Langmuir wave ($\mathbf{k}_0$) and a purely growing mode ($\mathbf{k}_3$). An up-shifted daughter Langmuir wave ($\mathbf{k}_2$) is also excited as the beat product of the Langmuir pump wave ($\mathbf{k}_1$) and the purely growing mode ($\mathbf{k}_3$).

where $\omega = \omega_1 + i\gamma$ and a positive γ represents the growth rate of the instabilities. Equations (5)–(9) in linearized form can be written as

$$\gamma\left(\frac{\delta n_e}{n_0}\right) + i\mathbf{k}_3 \cdot \delta\mathbf{V}_e + i\mathbf{k}_3 \cdot \mathbf{J} = 0 \qquad (5')$$

where

$$\mathbf{J} = n_0^{-1}(n_{e1}\mathbf{V}_{e0}^* + n_{e0}^*\mathbf{V}_{e1} + n_{e1}^*\mathbf{V}_{e2} \quad n_{e2}\mathbf{V}_{e1}^*)$$

is the superposition of nonoscillatory beating currents driven by the Langmuir pump wave in the oscillatory electron density perturbations of the excited high-frequency waves and vice versa; n_0 is the unperturbed plasma density.

$$i\mathbf{F} = -i\mathbf{k}_3\delta T_e - i\mathbf{k}_3 T_0\left(\frac{\delta n_e}{n_0}\right)$$
$$- e\mathbf{E}_3 - m\Omega_e\delta\mathbf{V}_e \times \hat{z} - m\nu_e(\delta\mathbf{V}_e - \delta\mathbf{V}_i) \qquad (6')$$

where

$$\mathbf{F} = m(\mathbf{k}_1 \cdot \mathbf{V}_{e0}^*\mathbf{V}_{e1} - \mathbf{k}_0 \cdot \mathbf{V}_{e1}\mathbf{V}_{e0}^*$$
$$+ \mathbf{k}_2 \cdot \mathbf{V}_{e1}^*\mathbf{V}_{e2} - \mathbf{k}_1 \cdot \mathbf{V}_{e2}\mathbf{V}_{e1}^*)$$

is the superposition of nonlinear Lorentz forces acting on an electron which oscillates under the influence of the Langmuir pump wave and experiences a force exerted by the excited high-frequency waves and vice versa. This force reduces to the ponderomotive force in the unmagnetized plasma case and includes an additional term, $-\langle \mathbf{V}_e \times \nabla \times \mathbf{V}_e\rangle$, in the magnetized plasma case. $\mathbf{E}_3$ is the low-frequency electric field. The inertial term has been neglected in (6′) since $\gamma \ll \nu_e$ is assumed and can be justified.

$$\delta T_e = \tfrac{2}{3}(H - iT_0\mathbf{k}_3 \cdot \delta\mathbf{V}_e)$$
$$\left[\gamma + 2\nu_e(m/M) + \frac{2}{5n_0}(k_{3z}^2R_\parallel^{e} + k_{3x}^2R_\perp^{e})\right] \qquad (7')$$

where $H = 2\nu_e m(\mathbf{V}_{e1} \cdot \mathbf{V}_{e0}^* + \mathbf{V}_{e2} \cdot \mathbf{V}_{e1}^*)$ is the differential ohmic heating term arising from electron energy dissipation in the high-frequency wave fields.

$$\gamma\delta n_i + in_0\mathbf{k}_3 \cdot \delta\mathbf{V}_i = 0 \qquad (8')$$

$$\bar{\nu}_{in}M\delta\mathbf{V}_i = -(T_0/n_0)i\mathbf{k}_3\delta n_i + e\mathbf{E}_3$$
$$+ M\Omega_i\delta\mathbf{V}_i \times \hat{z} + \nu_e m(\delta\mathbf{V}_e - \delta\mathbf{V}_i) \qquad (9')$$

where $\bar{\nu}_{in} = \gamma + \nu_{in}$. The nonlinear Lorentz force term is not included in (9′), because ions are too massive to respond quickly in the high-frequency fields. Eliminating $\mathbf{E}_3$, $\delta\mathbf{V}_e$, $\delta\mathbf{V}_i$, and δT_e from (5′)–(9′), we obtain the following coupled mode equation for the purely growing mode:

$$-\left\{\gamma\bar{\nu}_{in}a\left[b\left(1 + \frac{\Omega_e\Omega_i}{\nu_e\bar{\nu}_{in}}\right) + k_{3z}^2\frac{\Omega_e^2}{\nu_e^2}\right]\right.$$
$$\left. + C_s^2\left(\frac{\gamma}{3} + a\right)\left(b^2 + \frac{\Omega_e^3k_3^2k_{3z}^2}{\nu_e^2}\right)\right\}\left(\frac{\delta n}{n_0}\right)$$
$$= a\left\{\frac{bk_{3x}}{M}F_x - \frac{\Omega_e}{\nu_e}\frac{k_3^2k_{3y}}{M}F_y\right.$$
$$\left. + \left[b\left(1 + \frac{\Omega_e\Omega_i}{\nu_e\bar{\nu}_{in}} + \frac{\Omega_e^2}{\nu_e^2}k_3^2\right]\frac{k_{3z}}{M}F_z\right\}$$
$$+ \frac{2}{3M}H\left(b^2 + \frac{\Omega_e^2}{\nu_e^2}k_3^2k_{3z}^2\right)$$
$$+ i\left[ak_{3x}^2\frac{\Omega_e\Omega_i}{\nu_e} + \left(\frac{C_s^2}{3}\right)\left(b^2 + \frac{\Omega_e^2}{\nu_e^2}k_3^2k_{3z}^2\right)\right](\mathbf{k} \cdot \mathbf{J}) \qquad (10)$$

where

$$a = \gamma + 2\nu_e(m/M) + (3/2n_0)(k_{3z}^2R_\parallel^{e} + k_{3x}^2R_\perp^{e})$$
$$b = k_3^2 + k_{3z}^2(\Omega_e\Omega_i/\nu_e\bar{\nu}_{in})$$

and F_x, F_y, and F_z are the three components of $\mathbf{F}$.

The dispersion relation can be derived from (3), (4), and (10). Instead of giving its complicated general expression, we analyze the dispersion relation for a special case, wherein the Langmuir pump wave propagates along the geomagnetic field. This actually represents the most favorable situation, because this Langmuir wave has the largest intensity in the saturation spectrum of parametric decay instabilities. The study of this case is therefore sufficient to highlight the problems. Since the up-shifted ($\mathbf{k}_2$) and down-shifted ($\mathbf{k}_0$) daughter Langmuir waves are in symmetry with respect to the Langmuir pump wave (see (3) and (4)), the purely growing mode ($\mathbf{k}_3$) is exactly perpendicular to the geomagnetic field in this particular case. Illustrated in Figure 1 is the configuration of this four-wave interaction process in wave vector space:

$$\mathbf{k}_1 = k_1\hat{z} \qquad \mathbf{k}_3 = k_3\hat{x}$$
$$\mathbf{k}_2 = k_3\hat{x} + k_1\hat{z} \qquad \mathbf{k}_0 = -k_3\hat{x} + k_1\hat{z}$$

Hence (10) reduces to

$$\left[\gamma\bar{\nu}_{in}a_0\left(1 + \frac{\Omega_e\Omega_i}{\nu_e\bar{\nu}_{in}}\right) + C_s^2\left(\frac{\gamma}{3} + a_0\right)k_3^2\right]\left(\frac{\delta n}{n_0}\right)$$
$$= \frac{a_0k_3}{M}\left(F_x - \frac{\Omega_e}{\nu_e}F_y\right) + \frac{2}{3}\frac{k_3^2}{M}H$$
$$+ i\left(a_0\frac{\Omega_e\Omega_i}{\nu_e} + \frac{C_s^2k_3^2}{3}\right)k_3J_x \qquad (11)$$

where

$$a_0 = \gamma + 2\nu_e(m/M) + \nu_e k_3^2 r_e^2$$

where r_e is the electron gyroradius. With the aid of (2), (3) and (4) become

$$\Phi_2 = f\left(\frac{\Phi_1}{k_2^2}\right)\left(\frac{\delta n}{n_0}\right)\left[-k_3^2\omega_1^2\left(\frac{\Omega_e^2}{k_2^2} + 3v_t^2\right) - 2\omega_1^2\nu_e^2 + i\omega_1(\omega_1^2 - \Omega_e^2)\nu_e\right]^{-1} \qquad (12)$$

$$\Phi_0 = f\left(\frac{\Phi_1}{k_0^2}\right)\left(\frac{\delta n^*}{n_0}\right)\left[-k_3^2\omega_1^2\left(\frac{\Omega_e^2}{k_0^2} + 3v_t^2\right) - 2\omega_1^2\nu_e^2 + i\omega_1(\omega_1^2 - \Omega_e^2)\nu_e\right]^{-1} \qquad (13)$$

where

$$f = k_1^2\omega_p^2[(\omega_1^2 - \Omega_e^2) + 2i\omega_1\nu_e]$$

$$\omega_1^2 = \omega_p^2(1 + 3k_1^2/k_D^2) \qquad v_t^2 = T_0/m$$

and $\gamma \ll \nu_e$ has been assumed.

In the presence of high-frequency electrostatic wave fields, the electron density perturbations are given by

$$\delta n_j = -k_j^2\Phi_j/4\pi e \qquad j = 0, 1, 2$$

and the electron velocity perturbations can be represented approximately by

$$\mathbf{v}_j = -(e/m)\left[\hat{x}\,\frac{\omega_j}{\omega_j^2 - \Omega_e^2}\,k_{jx} + i\hat{y}\,\frac{\Omega_e}{\omega_j^2 - \Omega_e^2}\,k_{jx} + \hat{z}\,\frac{k_{jz}}{\omega_j}\right]\Phi_j \qquad j = 0, 1, 2$$

Then,

$$J_x = \frac{\omega_1}{(\omega_1^2 - \Omega_e^2)}\,\frac{k_1^2k_3}{4\pi n_0 m}\,(\Phi_1^*\Phi_2 - \Phi_1\Phi_0^*) \qquad (14)$$

$$H = 2\nu_e m(e/m)^2\,\frac{k_1^2}{\omega_1^2}\,(\Phi_1^*\Phi_2 + \Phi_1\Phi_0^*) \qquad (15)$$

$$F_x = m(e/m)^2\,\frac{k_1^2k_3}{(\omega_1^2 - \Omega_e^2)}\,(\Phi_1\Phi_2^* + \Phi_0\Phi_1^*) \qquad (16)$$

$$F_y = i\,\frac{m}{M}\,(e/m)^2\,\frac{\Omega_e}{\omega_1}\,\frac{k_1^2k_3}{(\omega_1^2 - \Omega_e^2)}\,(\Phi_1^*\Phi_2 - \Phi_1\Phi_0^*) \qquad (17)$$

Substituting (14)–(17) into (11) and with the aid of (12) and (13), we obtain the dispersion relation

$$\left\{\left[\gamma\bar{\nu}\left(1 + \frac{\Omega_e\Omega_i}{\nu_e\nu_{in}}\right) + k_3^2C_s^2\right]\left(\gamma + 2\nu_e\,\frac{m}{M} + \nu_e\,\frac{k_3^2v_t^2}{\Omega_e^2}\right) + \tfrac{2}{3}\gamma\,\frac{m}{M}\,k_3^2v_t^2\right\} = [2(m/M)(e/m)^2|\Phi_1|^2k_1^4k_3^4(k_1^2 + k_3^2)^{-1}]$$

$$\div\left\{\left[k_3^2\left(\frac{\Omega_e^2}{k_1^2 + k_3^2} + 3v_t^2\right) + 2\nu_e^2\right]^2 + (\omega_1^2 - \Omega_e^2)(\nu/\omega_1)^2\right\}$$

$$\cdot\left\{\left[a_0\left(\frac{\Omega_e^2}{k_1^2 + k_3^2} + 3v_t^2\right) + a_0\,\frac{\Omega_e^2}{\omega_1^2}\,\frac{(\omega_1^2 - \Omega_e^2)}{k_3^2}\right]_F + \left[\frac{4}{3}\,\frac{\nu_e}{\omega_1^2}\,(\omega_1^2 - \Omega_e^2)\left(\frac{\Omega_e^2}{k_1^2 + k_3^2} + 3v_t^2\right)\right]_H - a_0\left[\frac{\Omega_e^2}{\omega_1^2}\,\frac{(\omega_1^2 - \Omega_e^2)}{k_3^2} + \frac{2v_t^2(\omega_1^2 - \Omega_e^2)}{3\omega_1^2}\,\nu_e\right]_J\right\} \qquad (18a)$$

or

$$\left\{\left[\gamma\bar{\nu}\left(1 + \frac{\Omega_e\Omega_i}{\nu_e\nu_{in}}\right) + k_3^2C_s^2\right]\left(\gamma + 2\nu_e\,\frac{m}{M} + \nu_e\,\frac{k_3^2v_t^2}{\Omega_e^2}\right) + \tfrac{2}{3}\gamma\,\frac{m}{M}\,k_3^2v_t^2\right\} = 2(m/M)(e/m)^2\,[|\Phi_1|^2k_1^4k_3^4(k_1^2 + k_3^2)^{-1}]$$

$$\div\left\{\left[k_3^2\left(\frac{\Omega_e^2}{k_1^2 + k_3^2} + 3v_t^2\right) + 2\nu_e^2\right]^2 + (\omega_1^2 - \Omega_e^2)\left(\frac{\nu_e}{\omega_1}\right)^2\right\}$$

$$\cdot\left\{\tfrac{4}{3}\,\nu_e\left(\frac{\omega_1^2 - \Omega_e^2}{\omega_1^2}\right)\left(\frac{\Omega_e^2}{k_1^2 + k_3^2} + \tfrac{5}{2}\,v_t^2\right) + \left[\gamma + \nu_e\left(2\frac{m}{M} + k_3^2r_e^2\right)\right]\left(\frac{\Omega_e^2}{k_1^2 + k_3^2} + 3v_t^2\right)\right\} \qquad (18b)$$

On the right-hand side of (18*a*) the three terms labeled by *F*, *H*, and *J* correspond respectively to the three nonlinear effects, namely, nonlinear Lorentz forces, differential ohmic heating, and beating currents. The first term inside the brackets labeled by *F* comes from the ponderomotive force, and the second term is derived from $-(\mathbf{V}_e \times \nabla \times \mathbf{V}_e)$, which reduces to zero in the unmagnetized plasma. It is seen that the nonlinear Lorentz force and differential ohmic heating force add together for $\omega_1 > \Omega_e$ and are partially counterbalanced by beating currents with the net result given in (18*b*). Note that $a_0 = \gamma + 2\nu_e(m/M) + \nu_e k_3^2 r_e^2$, where $(m/M) \sim 3.4 \times 10^{-5}$ and $r_e \sim 2$ cm in the *F* region. Therefore the contribution of the ponderomotive force in generating field-aligned ionospheric irregularities is smaller than that of differential ohmic heating by a factor of $k_3^2 r_e^2$ for irregularities with scale lengths (λ_3) less than $\pi r_e(2M/m)^{1/2} \sim 15$ m and by a factor of (m/M) otherwise.

If the following ionospheric parameters are used for the *F* region heating experiments: $m/M(\mathrm{O}^+) \sim 3.4 \times 10^{-5}$, $\nu_e \sim 1$ kHz, $\Omega_e/2\pi \sim 1.2$ MHz, $v_t \sim 1.3 \times 10^5$ m/s, $\omega_1/2\pi \sim 6$ MHz, $\nu_{in} \sim 0.5$ Hz, $2\pi/k_1 \sim 0.4$ m, and $E_1 = |k_1\Phi_1| \sim 0.7$ V/m, equation (18*b*) can be simplified as

$$\left(\gamma\,\frac{\Omega_e\Omega_i}{\nu_e} + k_3^2C_s^2\right)\left(\gamma + 2\nu_e\,\frac{m}{M} + \nu_e k_3^2 r_e^2\right) + \frac{2}{3}\,\frac{m}{M}\,k_3^2v_t^2$$

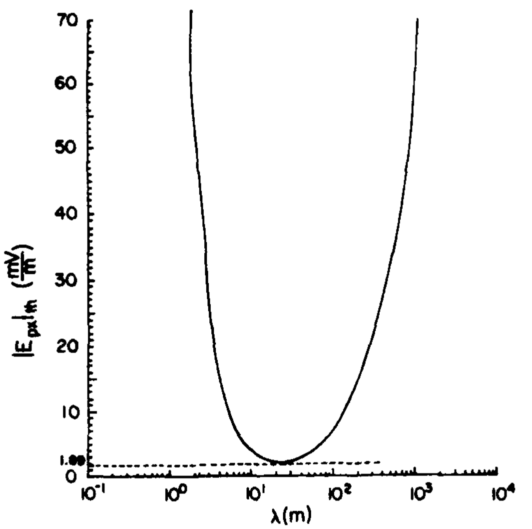

Fig. 2. Threshold field intensities $|E_{th}|$ as a function of scale lengths of the ionospheric irregularities excited by purely growing instabilities.

$$\approx \tfrac{8}{3}(m/M)(e/m)^2|\Phi_1|^2\nu_e\left(\frac{\Omega_e^2}{k_1^2+k_3^2}+\tfrac{5}{2}\,v_t^2\right)$$

$$\cdot\,[k_1^4k_3^4(k_1^2+k_3^2)^{-1}]$$

$$\div\left\{\left[k_3^2\left(\frac{\Omega_e^2}{k_1^2+k_3^2}+3v_t^2\right)+2\nu_e^2\right]^2+\nu_e^2\omega_1^2\right\} \qquad (19)$$

It is interesting to note that since $\Omega_e\Omega_i/\nu_e\tilde{\nu}_{in} \gg 1$, $\tilde{\nu}_{in}$ is finally canceled in (19). The reason can be understood from (10) that $\tilde{\nu}_{in}$ can be retained in the expression unless the purely growing modes are exactly field-aligned (i.e., $k_{3z} = 0$). In other words, $\tilde{\nu}_{in}$ has no net effect on field-aligned purely growing modes. It can be shown that the retardation on the polarization drift of field-aligned modes caused by ν_{in} damping is compensated by an $F_D \times B$ drift due to ν_{in} drag force in the direction perpendicular to the plane formed by the geomagnetic field and the polarization drift.

The threshold field $|E_{th}| = |k_1\Phi_1|$ is determined from (19) by setting $\gamma = 0$, i.e.,

$$\left|\frac{e}{m}\,E_{th}\right|^2 = \tfrac{3}{4}\,v_t^2\left(2\frac{m}{M}+k_3^2r_e^2\right)$$

$$\cdot\left\{\left[k_3^2\left(\frac{\Omega_e^2}{k_1^2+k_3^2}+3v_t^2\right)+2\nu_e^2\right]^2+\nu_e^2\omega_1^2\right\}$$

$$\cdot\,(k_1^2+k_3^2)\div\left[\left(\frac{\Omega_e^2}{k_1^2+k_3^2}+\tfrac{5}{2}\,v_t^2\right)k_1^2k_3^2\right] \qquad (20)$$

Solving (19) for γ gives the growth rate

$$\gamma = -\nu_e\left(\frac{m}{M}+\tfrac{11}{6}k_3^2r_e^2\right)+\nu_e\left[\left(\frac{m}{M}+\tfrac{11}{6}k_3^2r_e^2\right)^2\right.$$

$$\left.+\,2k_3^2r_e^2\left(2\frac{m}{M}+k_3^2r_e^2\right)\left(\frac{|E_1|^2}{|E_{th}|^2}-1\right)\right]^{1/2} \qquad (21)$$

The results of (20) and (21) are plotted in Figures 2 and 3 respectively. Also plotted in Figure 3 is the growth time of the instabilities defined to be the time interval for the amplitude of excited modes to exceed their thermal level by five e folds of magnitude.

The threshold field decreases with the scale lengths of irregularities in the small-scale range but becomes an increasing function in the large-scale range. This interesting behavior of threshold field versus scale lengths can be seen from (20) where

$$|E_{th}| \sim (\sqrt{3}/2)(m/e)(v_t^2k_3^2/k_1) \propto \lambda_3^{-2}$$

$$\lambda \ll \pi r_e(2M/m)^{1/2} \sim 15 \text{ m}$$

$$|E_{th}| \sim 1.2(m/M)^{1/2}v_t(m/e)(\nu_e\omega_1k_1/k_3\Omega_e) \propto \lambda_3 \qquad \lambda \gg 15 \text{ m}$$

While $|E_{th}|$ has a minimum value of 1.89 mV/m around λ_3 = 20 m, the growth rate (time) has a maximum value of 56.0 s^{-1} (minimum value of 0.09 s) near λ_3 = 6 m. Although meter-scale irregularities have the fastest growth rates, larger-scale (tens and hundreds of meters) irregularities can still be excited by the present instabilities in reasonable time (a few to tens of seconds). However, the thresholds and growth time of kilometer-scale irregularities increase drastically. Consequently, kilometer-scale irregularities cannot be excited by the present instabilities as favorably as by the thermal self-focusing instabilities [*Perkins and Valeo*, 1974; *Cragin and Fejer*, 1974; *Berger et al.*, 1975].

4. DISCUSSIONS AND CONCLUSIONS

Along the line of *Perkins*' [1974] approach, we consider the saturation spectrum of parametric decay instabilities as the source of heating-induced ionospheric irregularities. Instead of three-wave coupling, we analyze four-wave interaction whereby the Langmuir pump wave can excite two daughter Langmuir waves (wave vector up-shifted and down-shifted sidebands) and ionospheric irregularities (purely growing modes). This is, essentially, the filamentation instability of Langmuir waves in a magnetized plasma. Moreover, nonoscillatory heating currents as well as differ-

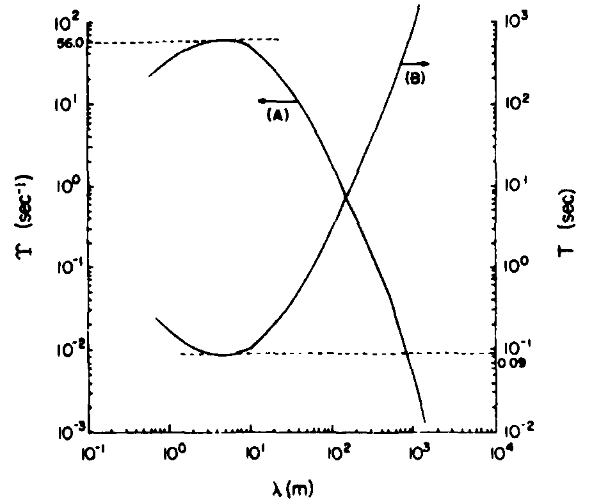

Fig. 3. Growth rates γ and growth times T as a function of the scale lengths of the excited ionospheric irregularities. Curves A and B represent respectively the growth rates and growth times of purely growing instabilities. Growth time is defined to be the time interval for the amplitude of excited modes to exceed their thermal level by five e folds of magnitude.

ential ohmic heating and nonlinear Lorentz force are the nonlinear effects in the formation of field-aligned ionospheric irregularities. Because the excited low-frequency modes are purely growing modes, the beating current always provides a stabilization effect to counterbalance partially the differential ohmic heating and nonlinear Lorentz forces. The principal results of our analyses are summarized as follows. (1) A broad spectrum of ionospheric irregularities can be produced with scale lengths ranging from meters to hundreds of meters under reasonable experimental conditions. (2) The analyses of four-wave interaction reflect new features of purely growing instabilities not discovered before in the analyses of three-wave interaction. The threshold field $|E_{th}|$ of the instabilities decreases with the scale lengths λ of the ionospheric irregularities as $|E_{th}| \propto \lambda^{-2}$ in the small-scale range (<15 m) but becomes an increasing function as $|E_{th}| \propto \lambda$ in the large-scale range. The threshold field has a minimum value of ~ 2 mV/m at $\lambda \sim 20$ m. The growth rate γ of the instabilities maximizes at $\lambda \sim 6$ m and decreases drastically as $\gamma \propto \lambda^{-2}$ with scale lengths larger than a few kilometers.

There is one important point to be made regarding the maximum scale lengths of ionospheric irregularities excited by electrostatic pump waves. As shown in Figures 2 and 3, the instabilities do not favor the excitation of large-scale (kilometers) irregularities. On the other hand, the ionospheric inhomogeneity also imposes a limitation as explained below. To generate large-scale irregularities as the beat product of two Langmuir waves, it requires that the coherence of these two short-wavelength Langmuir waves be maintained over a distance of many wavelengths in the transverse direction. Under quiet and spatially uniform (with typical scale height of a few tens of kilometers) ionospheric conditions, the maximum scale lengths of the excited irregularities are determined by the instabilities themselves. Otherwise, they are primarily determined by the spatial inhomogeneity of the medium.

It should be pointed out that although growth rates are determined by ionospheric and experimental parameters, the location of their maximum (around $\lambda_3 = 6$ m in Figure 3) does not change significantly with different parameters (e.g., varying $|E_1|$: 0.3–1.2 V/m). The result that meter-scale irregularities have the fastest growth rates generally agrees with the experiments. However, whether the growth rates of irregularities maximize at the meter-scale lengths as predicted by this theory cannot be thoroughly checked from the available backscatter radar measurements [e.g., *Rao and Thome*, 1974; *Minkoff*, 1974] and awaits future experimental verification. The apparent experimental difficulty is that, for instance, irregularities with a scale length of 10 m can be picked up by a backscatter radar of 15 MHz, but HF radar echoes cannot be simply attributed to the scattering from irregularities, because refraction is important too. Lower-frequency HF probing radar signals cannot even reach the heated ionospheric *F* region.

The use of unattenuated Langmuir pump waves is not as unrealistic as it appears to be. As mentioned before, they are waves with saturated intensities maintained by CW heater waves. As soon as the heater waves are turned off, they die out within milliseconds. The induced ionospheric irregularities do not decay quickly, however. The reason is that the field-aligned nature of these irregularities prevents them from being removed promptly by the diffusion damping. Meter-scale irregularities can persist for seconds, and large-scale (hundreds of meters) irregularities can even survive for hours.

Although our attention has been addressed primarily to the generation of field-aligned ionospheric irregularities, the filamentation of Langmuir pump waves is also an important result in our work. *Schmidt* [1975] shows that the breakup of solitons is just a continuation of the filamentation instability. A comparison between the present work and the recent work on a soliton and its collapse [*Weatherall et al.*, 1982; *Hafizi et al.*, 1982] cannot be made directly, however. This is because only ponderomotive force is included to analyze the nonlinear evolution of Langmuir waves via the oscillating two-stream instability [*Weatherall et al.*, 1982] or via the scattering of Langmuir waves off ion acoustic quasi-modes [*Hafizi et al.*, 1982]. In our future work, we plan to take a broadband Langmuir pump in the analysis of the modulational instability. Then, the nonlinear evolution of this instability can be studied and compared with the results of the present linear stability analysis. As mentioned before, cascading processes and nonlinear ion Landau damping [*Fejer and Kuo*, 1973*a*; *Perkins et al.*, 1974] have been suggested as the saturation mechanisms of the parametric decay instability. The process discussed in our paper can also be considered as a saturation mechanism of the parametric decay instability. It occurs on a much slower timescale than the cascading processes or the nonlinear ion Landau damping. It, then, contributes to depleting and broadening the saturation spectrum of Langmuir waves determined by, for example, the cascading processes. Therefore the depletion and broadening effects of the present process on the Langmuir pump waves should be taken into account in our future analyses. If pump depletion is the saturation mechanism of the instability proposed here, the intensity of the purely growing modes can then be determined.

In conclusion, purely growing instabilities driven by the saturation spectrum of parametric decay instabilities can excite not only meter-scale but also tens and even hundreds of meter-scale irregularities within seconds (see Figure 3) under optimum (i.e., quiet and spatially uniform) ionospheric conditions. The excitation of kilometer-scale irregularities is strictly restricted by the instabilities themselves (i.e., their spatial coherency) and by the spatial inhomogeneity of the medium. It is true that parametric decay instabilities encounter competitive processes as indicated probably by the overshoot phenomenon of plasma line intensity [*Showen and Kim*, 1978]. However, since the threshold fields of purely growing instabilities are a few millivolts per meter in the tens of meters scale range (see Figure 2), parametric decay instabilities may still play a significant role in generating intermediate-scale ionospheric irregularities in the presence of other competitive processes.

Acknowledgments. This work was supported by NSF grant ATM-8114427 at Polytechnic Institute of New York and by AFGL contract F19628-80-C-0016 at Regis College Research Center.

The Editor thanks M. V. Goldman and another referee for their assistance in evaluating this paper.

References

Bardwell, S., and M. V. Goldman, Three-dimensional Langmuir wave instabilities in type III solar radio bursts, *Astrophys. J.*, *209*, 912, 1976.

Berger, R. L., M. V. Goldman, and D. F. DuBois, Stimulated diffusion scattering in ionospheric modification, *Phys. Fluids*, *18*, 207, 1975.

Carlson, H. C., W. E. Gordon, and R. L. Showen, High frequency induced enhancements of the incoherent scatter spectrum at Arecibo, *J. Geophys. Res.*, *77*, 1242, 1972.

Cragin, B. L., and J. A. Fejer, Generation of large-scale field-aligned irregularities in ionospheric modification experiments, *Radio Sci.*, *9*, 1071, 1974.

Das, A. C., and J. A. Fejer, Resonance instability of small-scale field-aligned irregularities, *J. Geophys. Res.*, *84*, 6701, 1979.

Fejer, J. A., and K. N. Graham, Electron acceleration by parametrically excited Langmuir waves, *Radio Sci.*, *9*, 1081, 1974.

Fejer, J. A., and Y. Y. Kuo, Structure in the nonlinear saturation spectrum of parametric instabilities, *Phys. Fluids*, *16*, 1490, 1973*a*.

Fejer, J. A., and Y. Y. Kuo, The saturation spectrum of parametric instabilities, *AGARD Conf. Proc.*, *138*, 11-1–11-8, 1973*b*.

Hafizi, B., J. C. Weatherall, M. V. Goldman, and D. R. Nicholson, Scattering and collapse of Langmuir waves driven by a weak electron beam, *Phys. Fluids*, *25*, 392, 1982.

Inhester, B., A. C. Das, and J. A. Fejer, Generation of small-scale field-aligned irregularities in ionospheric heating experiments, *J. Geophys. Res.*, *86*, 9101, 1981.

Lee, M. C., and J. A. Fejer, Theory of short-scale field-aligned density striations due to ionospheric heating, *Radio Sci.*, *13*, 893, 1978.

Lee, M. C., and S. P. Kuo, Theory of HF-induced upper hybrid waves and ionospheric irregularities, submitted to *J. Geophys. Res.*, 1982.

Minkoff, J., Radio frequency scattering from a heated ionospheric volume, 3, Cross section calculations, *Radio Sci.*, *9*, 997, 1974.

Nicholson, D. R., Magnetic field effects on electrons during ionospheric modification, *J. Geophys. Res.*, *82*, 1839, 1977.

Perkins, F. W., A theoretical model for short-scale field-aligned plasma density striations, *Radio Sci.*, *9*, 1065, 1974.

Perkins, F. W., and P. K. Kaw, On the role of plasma instabilities in ionospheric heating by radio waves, *J. Geophys. Res.*, *76*, 282, 1972.

Perkins, F. W., and E. J. Valeo, Thermal self-focusing of electromagnetic waves in plasmas, *Phys. Rev. Lett.*, *32*, 1234, 1974.

Perkins, F. W., C. Oberman, and E. J. Valeo, Parametric instabilities and ionospheric modification, *J. Geophys. Res.*, *79*, 1478, 1974.

Rao, P. B., and G. D. Thome, A model for RF scattering from field-aligned heater-induced irregularities, *Radio Sci.*, *9*, 987, 1974.

Schmidt, G., Stability of envelope solitons, *Phys. Rev. Lett.*, *34*, 724, 1975.

Showen, R. L., and D. M. Kim, Time variation of HF induced plasma waves, *J. Geophys. Res.*, *83*, 623, 1978.

Weatherall, J. C., M. V. Goldman, and D. R. Nicholson, Parametric instabilities in weakly magnetized plasma, *Astrophys. J.*, *246*, 306, 1981.

Weatherall, J. C., J. P. Sheerin, D. R. Nicholson, G. L. Payne, M. V. Goldman, and P. J. Hansen, Solitons and ionospheric heating, *J. Geophys. Res.*, *87*, 823, 1982.

Weinstock, J., Enhanced airglow, Electron acceleration, and parametric instabilities, *Radio Sci.*, *9*, 1085, 1974.

(Received May 14, 1982;
revised September 2, 1982;
accepted September 21, 1982.)

JOURNAL OF GEOPHYSICAL RESEARCH, VOL. 87, NO. A2, PAGES 751–755, FEBRUARY 1, 1982

Faraday Polarization Fluctuations of Transionospheric Propagation

M. C. LEE

Regis College Research Center, Weston, Massachusetts 02193

Rapid, intense Faraday polarization fluctuations of satellite HF and VHF beacon signals have been shown to be caused by wave scattering from density irregularities. Except in the case of HF signals (e.g., 20 MHz), irregularities with Gaussian spectra cannot affect the polarization of satellite signals as effectively as irregularities with power law spectra. It is adequate to use the theory of single scattering for describing the Faraday polarization fluctuations even in cases involving large density fluctuations, such as those of 41-MHz signals near the magnetic equator and those of 136-MHz signals near the equatorial anomaly region.

INTRODUCTION

Rapid, intense fluctuations in Faraday rotation angles have been observed at middle and high latitudes in low orbit satellite beacon signals of 20, 40, and 54 MHz [*Kent*, 1959; *Parthasarathy and Reid*, 1959; *Yeh and Swenson*, 1959; *McClure*, 1964; *Roger*, 1965]. Similar Faraday polarization fluctuations (FPF) of 136-MHz signals from geostationary satellite have also been seen at locations like Ascension Island, Calcutta, and Delhi, situated near the equatorial anomaly region [*Klobuchar and Aarons*, 1980; *Das Gupta and Maitra*, 1980; *Lee et al.*, 1982 and references therein]. In the observations at Ascension Island, *Lee et al.* [1982] noted the coexistence of FPF with strong *L* band amplitude scintillations as displayed in Figure 1. These two phenomena appeared together during the postsunset hours and disappeared simultaneously near or after midnight.

FPF of satellite signals have been interpreted as the depolarization of linearly polarized waves by wave scattering from ionospheric irregularities [*Yeh and Liu*, 1967; *Lee et al.*, 1982]. *Yeh and Liu* [1967] show that small density fluctuations with Gaussian spectra are sufficient to cause FPF of 20-MHz satellite signals. In the case of 136-MHz FPF, *Lee et al.* [1982] show that small-scale (<200 m) density fluctuations with power law other than Gaussian spectra are responsible for this effect. High ambient plasma densities have been shown to be required to cause the FPF of 136-MHz signals.

The purposes of this paper are to investigate the different nature of ionospheric irregularities that give rise to the FPF of satellite HF and VHF beacon signals and to discuss the validity of weak scattering theory and the effect of multiple scattering in the study of FPF in the ionosphere.

FARADAY POLARIZATION FLUCTUATIONS (FPF)

A linearly polarized satellite beacon signal can be decomposed into an ordinary and an extraordinary mode for its transionospheric propagation. If a slab of uniform density irregularities is assumed to exist in the *F* region, each mode can interact with density irregularities in a different manner as described below. Assuming that the irregularity scale sizes of interest are much greater than the wavelength of the signal, one can neglect the refraction caused by spatial inhomogeneity and the reflection from density irregularities. For simplicity, one may only consider single scattering process, which introduces different complex shifts into the original ordinary and extraordinary modes, i.e., $\mathbf{E}_{R\pm}(z_0) = \mathbf{E}_{i\pm} \exp(-i\phi_\pm)$, where $\mathbf{E}_{R+}(\mathbf{E}_{R-})$ refers to the received wave field of the ordinary (extraordinary) mode in the presence of density irregularities, $\mathbf{E}_{i+}(\mathbf{E}_{i-})$ is the wave field of the ordinary (extraordinary) mode in the absence of density irregularities, and $\phi_+(\phi_-)$ the phase shift caused by wave scattering from density irregularities. The phase shifts are given by

$$\phi_\pm = -iz_0 r_e \int_V d^3r \, \frac{\Delta N(\mathbf{r}) \exp\left[-ik_\pm(r + R - z_0)\right]}{Rr}$$

where $r_e(\sim 2.82 \times 10^{-15}$ m) is the classical electron radius, $\Delta N(r)$ is the local density fluctuations, $k_+(k_-)$ is the wave number of the ordinary (extraordinary) mode, V is the total volume of density irregularities, and as illustrated in Figure 2, z_0 is the distance between the satellite and the ground-based receiver, r that between the satellite and the scatterer V_s, and R that between the scatterer V_s and the receiver, respectively. For quasi-longitudinal propagation in the ionosphere, $k_\pm = k[1 \pm XY \cos\theta/2(1 - X)]$ where X, Y, and θ are the squared ratio of the ambient plasma frequency (f_N) to the wave frequency (f), the ratio of electron cyclotron frequency (Ω) to the wave frequency, and the propagation angle of the signal with respect to the geomagnetic field; $k = (2\pi f/c)(1 - X)^{1/2}$ is the wave number for propagating in an isotropic medium (i.e., $Y \to 0$).

An induced Faraday rotation angle ($\Delta\Omega$) due to wave scattering by density irregularities is just the half of the differential phase shift between the ordinary and the extraordinary modes, i.e.,

$$\Delta\Omega = \tfrac{1}{2}(\phi_+ - \phi_-) = -z_0 r_e \cdot \int_V d^3r \, \frac{\Delta N(\mathbf{r}) \exp\left[-ik(r + R - z_0)\right]}{Rr} \sin\left[\varepsilon k(r + R - z_0)\right]$$

where $\varepsilon = XY \cos\theta/2(1 - X)$.

An induced wave field that is perpendicular to the original one can be visualized to be associated with the induced Faraday rotation angle. The ratio of the induced to the original wave fields is approximately equal to the induced Faraday rotation angle, if the differential phase shift between two characteristics modes is less than one radian.

The physical quantity of interest is the variance of the induced Faraday rotation angle, i.e.,

$$\langle|\Delta\Omega|^2\rangle = z_0^2 r_e^2 \int_V d^3r_1 \int_V d^3r_2 \, \frac{\langle\Delta N(\mathbf{r}_1)\Delta N^*(\mathbf{r}_2)\rangle}{R_1 R_2 r_1 r_2} \cdot \cos\left[k(r_1 + R_1 - z_0) - k(r_2 + R_2 - z_0)\right] \cdot \sin\left[\varepsilon k(r_1 + R_1 - z_0)\right] \sin\left[\varepsilon k(r_2 + R_2 - z_0)\right] \tag{1}$$

Paper number 1A1606.
0148-0227/82/001A-1606$01.00

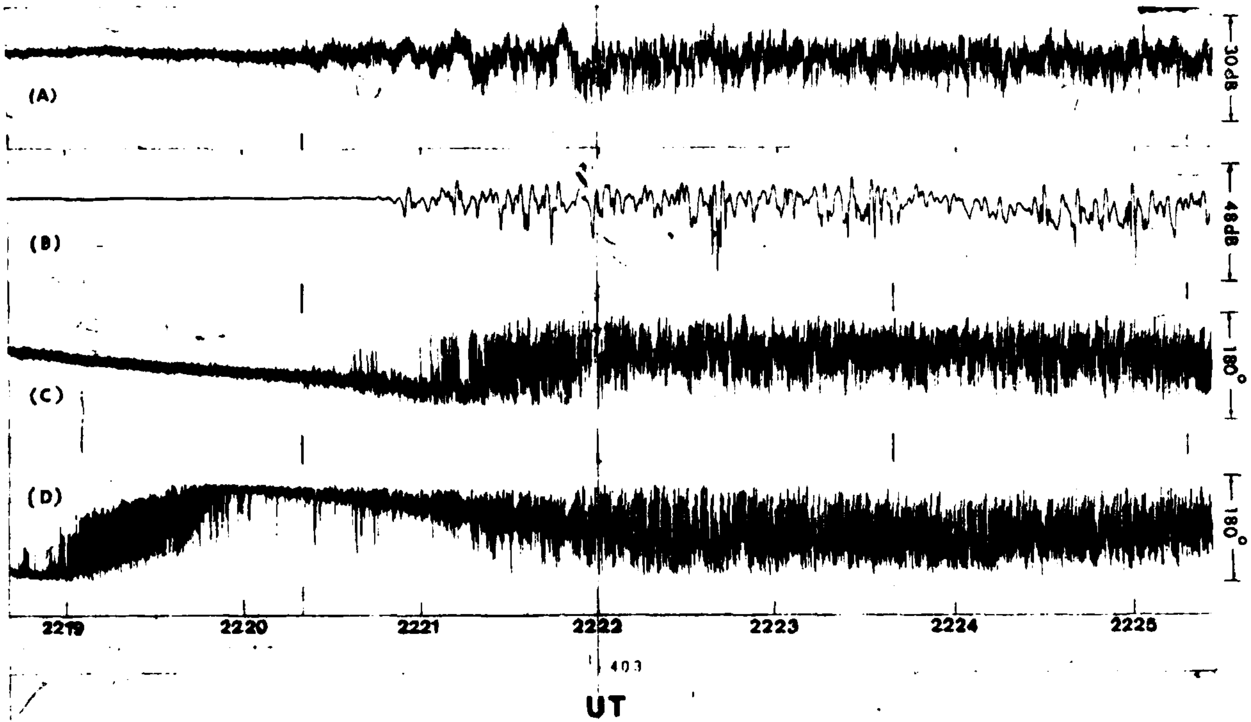

Fig. 1. Sample data of the geostationary satellite signals received at Ascension Island on January 2, 1980. The amplitude scintillations of the 136-MHz signals transmitted from SIRIO and those of the L band (1.541 GHz) transmitted from MARISAT-(I) are displayed in channels (A) and (B), respectively. Shown in channels (C) and (D) are the Faraday rotation measurements of 136-MHz signals in a ramp format with one channel displaced by 90° relative to the other. Rapid, intense fluctuations make the last two channels almost undistinguishable [*Lee et al.*, 1982].

where the angle brackets indicate that the spatial average is taken over the volume V; $\langle \Delta N(\mathbf{r}_1)\Delta N^*(\mathbf{r}_2)\rangle$ is the autocorrelation function of ionospheric irregularities.

IONOSPHERIC IRREGULARITIES

Power law spectra and Gaussian spectra with a scale size of 1 km have been seen to be associated respectively with the early and the late developed phases of irregularities in the observation of satellite scintillations [*Basu et al.*, 1980*a*]. To simplify the problem mathematically, statistically isotropic density irregularities are considered and assumed to be generated by spatially homogeneous processes, namely, the correlation function can be expressed as $\langle \Delta N(\mathbf{r}_1)\Delta N^*(\mathbf{r}_2)\rangle = (\Delta N)^2 \exp[-(|\mathbf{r}_1 - \mathbf{r}_2|)^m l^{-m}]$, where $(\Delta N)^2$ is the mean square fluctuations of the ambient plasma density; $m = 1$ for the power law type and $m = 2$ for the Gaussian type of ionospheric irregularities.

Making the following coordinate transformation in (1): $x = \frac{1}{2}(x_1 + x_2)$, $y = \frac{1}{2}(y_1 + y_2)$, $z = \frac{1}{2}(z_1 + z_2)$, $\xi = x_1 - x_2$, $\eta = y_1 - y_2$, $\zeta = z_1 - z_2$, and integrating (1) over x and y from $-\infty$ to $+\infty$, one obtains

$$\langle |\Delta\Omega|^2\rangle = \pi(\Delta N)^2 r_e^{\,2} \int_a^{a + D\sec\chi} dz \iiint_{-\infty}^{+\infty} d\zeta\, d\eta\, d\xi \cdot \exp[-(\zeta^2 + \eta^2 + \xi^2)^{m/2} l^{-m}] \cdot \{2F(0)\sin[F(0)(\xi^2 + \eta^2)] - F(\varepsilon)\sin[F(\varepsilon)(\xi^2 + \eta^2)] - F(-\varepsilon)\sin[F(-\varepsilon)(\xi^2 + \eta^2)]\} \qquad (2)$$

where D is the thickness of irregularities layer, χ the zenith angle; $F(t) = z_0 k\{|2\zeta(2z - z_0) + 4t[zz_0 - z^2 - (\zeta/2)^2]|\}^{-1}$, $t = 0, \pm\varepsilon$. It is clear in (2) that if $F(\pm\varepsilon) \simeq F(0)$, $\langle|\Delta\Omega|^2\rangle$ vanishes and no FPF can be observed. Therefore, FPF requires

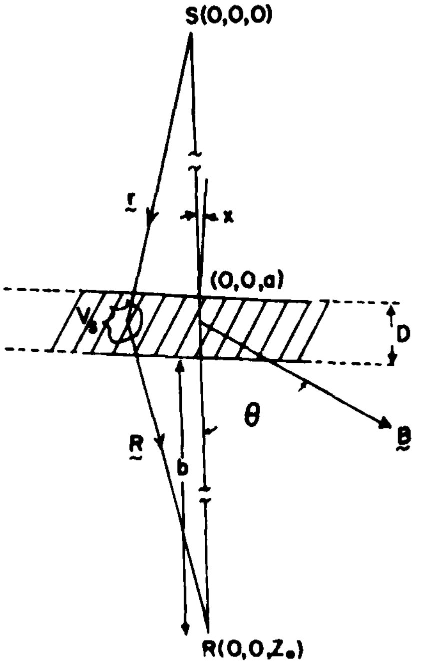

Fig. 2 Geometry of transionospheric propagation and wave scattering by density irregularities.

that

$$4\varepsilon[zz_0 - z^2 - (l/2)^2] \gtrsim 2l(2z - z_0) \qquad (3)$$

in $F(\pm\varepsilon)$, l's have replaced ζ's in (3) since ζ is of the order of l.

On the above condition it can be shown that

$$\langle|\Delta\Omega|^2\rangle = 2\lambda^2 r_e^{\,2}\langle(\Delta N/N)^2\rangle_p N^2 D \cdot \sec\chi[\varepsilon z_m(z_0 - z_m)\lambda/(2\pi z_0)]^{1/2} \qquad (4)$$

for irregularities with power law spectra [*Lee et al.*, 1982], where $\lambda = 2\pi/k$, and z_m is the distance between the satellite and the mean altitude of density irregularities, and that

$$\langle|\Delta\Omega|^2\rangle = \pi^{-3/2} l^3 \lambda^4 r_e^{\,2} N^2\langle(\Delta N/N)^2\rangle_G \cdot [\varepsilon z_m(z_0 - z_m)/z_0]^2 D \sec\chi \qquad (5)$$

for irregularities with Gaussian spectra [*Yeh and Liu*, 1967]. Equations (4) and (5) can be used to estimate the required density fluctuations ($\langle(\Delta N/N)^2\rangle^{1/2}$) for causing different degrees of FPF ($\langle|\Delta\Omega|^2\rangle^{1/2}$) under the given ionospheric conditions.

Equating the right-hand sides of (4) and (5) leads to

$$\Gamma = \frac{\langle(\Delta N/N)^2\rangle_G^{\;1/2}}{\langle(\Delta N/N)^2\rangle_p^{\;1/2}} = 2\pi^{1/2} l^{3/2} f_N^{\,-3/2}[z_0^{\,-1} z_m(z_0 - z_m)\Omega c(\cos\theta)]^{-3/4} \cdot (1 - f_N^{\,2}/f^2)^{3/4} f^3 \qquad (6)$$

which gives the ratio of Gaussian to power law types of density fluctuations in causing the same level of FPF; where f_N, Ω, c, and f are the ambient plasma frequency, electron cyclotron frequency, speed of light in vacuum, and the signal frequency, respectively.

If the scale sizes of irregularities are assumed to be much less than the slab thickness of irregularities, one may neglect $(l/2)^2$ in (3) and obtain

$$2(f_N/f)^2(\Omega/f)(1 - f_N^{\,2}/f^2)^{-1} \cdot \cos\theta\, z_m(z_0 - z_m) \gtrsim l(2z_m - z_0) \qquad (7)$$

on the substitution of $\varepsilon = XY\cos\theta/2(1 - X)$. Z's have been replaced in (3) by z_m's, which represent the distance between the satellite and the mean altitude of density irregularities. Taking the equality in (7), one can determine the outer scale sizes (l) of irregularities involved in causing the FPF of satellite beacon signals under the given ionospheric conditions.

FPF OF GEOSTATIONARY SATELLITE BEACON SIGNALS

As mentioned before, FPF of geostationary satellite beacons at 136 MHz have only been reported from ground-stations such as Ascension Island, Calcutta, Delhi, etc., near the equatorial anomaly region during the current solar maximum period. In the observations made at Ascension Island (31° S dip), very high f_oF_2 (16–20 MHz) were indicated from the TEC measurements (J. A. Klobuchar, private communication, 1981) and from the airborne-ionosonde measurements of ionization density profiles (E. J. Weber and J. G. Moore, private communication, 1981). While large FPF of low orbit satellite 40-MHz signals have been seen at middle-latitude stations, e.g., Cambridge, England [*Kent*, 1959], Faraday rotation measurements of geostationary satellite (ATS 6) 41-MHz signals made at Huancayo (1.3° N dip), Peru in 1975 did not show rapid, intense fluctuations (J. A. Klobuchar, private communications, 1981). The f_oF_2 at Huancayo were generally less than 10 MHz in this solar quiet year.

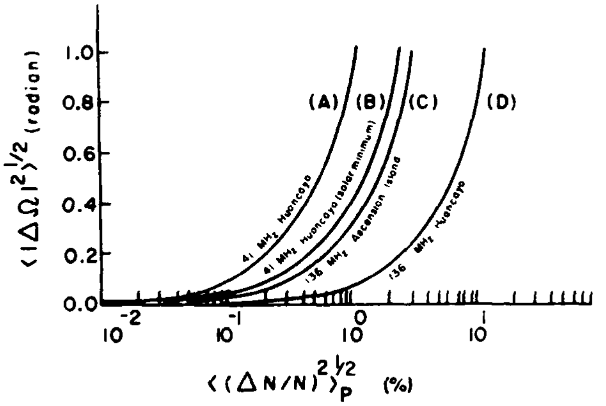

Fig. 3a. $\langle(\Delta N/N)^2\rangle^{1/2}$ versus $\langle|\Delta\Omega|^2\rangle^{1/2}$ for power law type of irregularities to cause the FPF of geostationary satellite 41-MHz beacons at Huancayo (curves (A) and (B)) and the FPF of 136-MHz beacons at Ascension Island (curve (C)) and at Huancayo (curve (D)). The propagation angles (θ) and the zenith angles (χ) of 136-MHz signals at Ascension Island and at Huancayo are 52°, 10° and 85°, 70°, respectively. θ and χ of 41-MHz signals at Huancayo are 82° and 70°. The ambient plasma densities N (or frequencies f_N) at Ascension Island and at Huancayo are taken to be 4.05×10^{12} m^{-3} (or 18 MHz) and 1.25×10^{12} m^{-3} (or 10 MHz), respectively. But in the solar minimum case at Huancayo (curve (B)), N (or f_N) is assumed to be 6.13×10^{11} m^{-3} (or 7 MHz).

Let us assume that ionospheric irregularities have a thickness (D) of 200 km at a mean altitude of 600 km ($z_0 - z_m$). Figure 3*a* shows the theoretically calculated $\langle(\Delta N/N)^2\rangle_p^{\;1/2}$ versus $\langle|\Delta\Omega|^2\rangle^{1/2}$ (equation (4)) for power law type of irregularities to cause the 41-MHz FPF at Huancayo and the 136-MHz FPF at Ascension Island and at Huancayo; $\langle|\Delta\Omega|^2\rangle^{1/2} = 0.1$ radians corresponds to appreciable FPF and $\langle|\Delta\Omega|^2\rangle^{1/2} = 0.5$ radians to large FPF. The outer scale sizes of irregularities l (equation (7)) involved are displayed in Figure 3*b*. Γ versus f_N (equation (6)) are plotted in Figure 3*c*. The product of Γ and $\langle(\Delta N/N)^2\rangle_p^{1/2}$ gives the required Gaussian type of density fluctuations $\langle(\Delta N/N)^2\rangle_G^{\;1/2}$ for causing the same level of FPF.

The 136-MHz FPF at Ascension Island turns out to be caused by small-scale (< 200 m) irregularities with about 1% density depletion. It is, however, impossible for Gaussian type of irregularities to cause the 136-MHz FPF, since absurdly

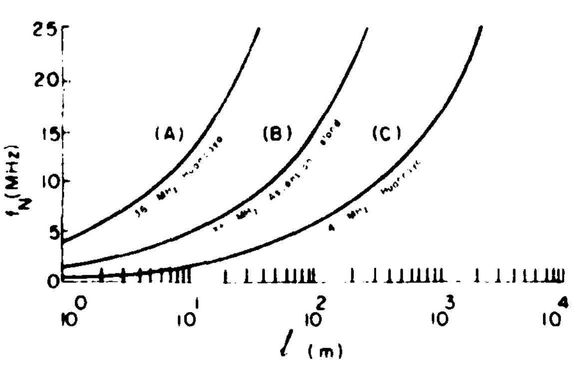

Fig. 3b. The outer scale sizes (l) of irregularities versus ambient plasma frequencies (f_N) in causing the 41-MHz FPF at Huancayo (curve (C)) and the 136-MHz FPF at Huancayo (curve (A)) and at Ascension Island (curve (B)).

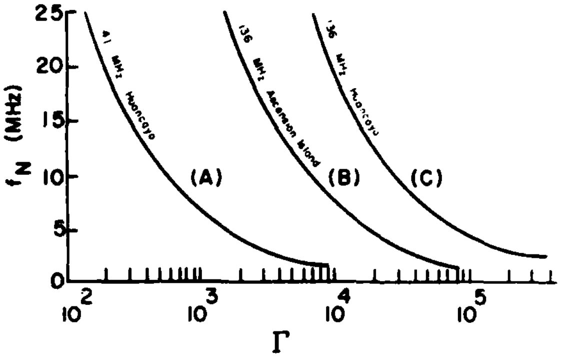

Fig. 3*c*. Γ versus f_N. The product of Γ and $\langle(\Delta N/N)^2\rangle_p^{1/2}$ gives the required Gaussian type of density fluctuations $\langle(\Delta N/N)^2\rangle_G^{1/2}$ for causing the same level of 41-MHz FPF at Huancayo (curve (A)) and for causing that of 136-MHz FPF at Huancayo (curve (C)) and at Ascension Island (curve (B)).

large density depletions (e.g., $\langle(\Delta N/N)^2\rangle^{1/2} = 834\%$ for $\langle|\Delta\Omega|^2\rangle^{1/2} = 0.1$) are required. The 136-MHz FPF are, therefore, not expected during the late phase of ionospheric irregularities. Since both the *L* band amplitude scintilation and the 136-MHz FPF are caused by small-scale (< 1 km) density irregularities, the coexistence of these two phenomena observed at Ascension Island can be so explained. In contrast, the observation of 136-MHz FPF at Huancayo is not expected. This is because Huancayo is located near the magnetic equator, where the f_oF_2 is relatively low and the propagation angles θ of geostationary beacons are nearly perpendicular to the geomagnetic field, therefore as shown in Figure 3, meter scale irregularities with unrealistically large fluctuations (1.4% for $\langle|\Delta\Omega|^2\rangle^{1/2} = 0.1$) are required.

The theory predicts that the 41-MHz FPF at Huancayo, if any, are caused by irregularities with an outer scale of several hundreds of meters. This leads to the expectation of the coexistence of 41-MHz FPF and the *L* band amplitude scintillation.

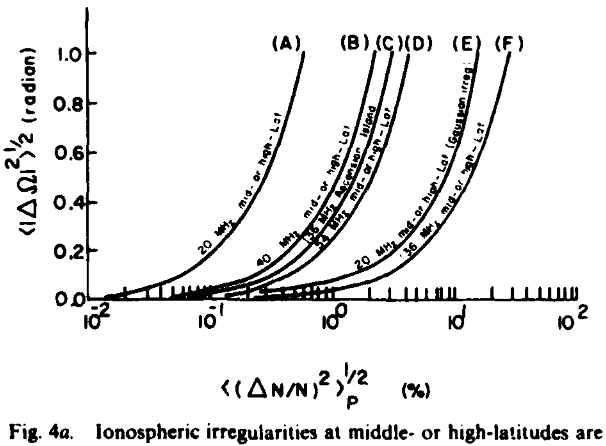

Fig. 4*a*. Ionospheric irregularities at middle- or high-latitudes are assumed to have a thickness of 50 km at a mean altitude of 400 km. Curves (A), (B), (D), and (F) correspond to the FPF of low orbit satellite 20, 40, 54, and 136-MHz signals, respectively, caused by power law type of irregularities within plasma density background of 1.25×10^{12} m^{-3} (or $f_N = 10$ MHz). Both the propagation angles (θ) and the zenith angles (χ) are taken to be zeros for simplicity. But irregularities of 200 km thick within high plasma density environment of 4.05×10^{12} m^{-3} (or $f_N \sim 18$ MHz) have been assumed in obtaining curve (C) for the FPF of low orbit satellite 136-MHz beacons at Ascension Island. Curve (E) shows the condition for the FPF of 20 MHz signals caused by irregularities with Gaussian rather than power law spectra.

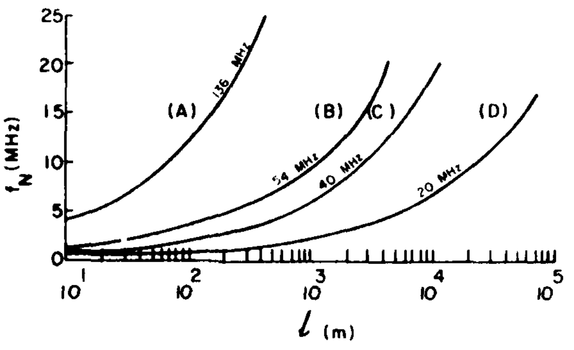

Fig. 4*b*. Curves (A), (B), (C), and (D) show the outer-scale sizes of irregularities involved in causing the FPF of 136, 54, 40, and 20-MHz signals, respectively, within different plasma environments (f_N).

No large FPF of ATS 6 41-MHz signals observed at Huancayo in 1975 probably can be attributed to low f_oF_2 in the year of low sunspot numbers and small Δ*N* near the magnetic equator. Indeed, the *L* band amplitude scintillations, which are primarily affected by Δ*N*, show small fluctuations under low sunspot conditions observed at Huancayo [*Basu et al.*, 1980*b*]. It is possible to see large FPF of geostationary 41-MHz beacons at Huancayo during the current solar maximum period. However, if Δ*N* and *N* in the anomaly region are greater than those at the magnetic equator, as *Aarons et al.* [1981] have discussed, the FPF of geostationary 41-MHz beacons recorded at Huancayo will not be as large as those of geostationary 136-MHz beacons measured at Ascension Island.

FPF OF LOW ORBIT SATELLITE BEACON SIGNALS

Since the FPF of geostationary satellite 136-MHz beacons have been observed at Ascension Island, it is natural to speculate that the FPF of low orbit satellite 136-MHz beacons could also be seen at the same location. As shown in Figures 4*a*, 4*b*, and 4*c*, the ionospheric conditions for causing the latter are not very different from those for the former. It also may be explained by small-scale irregularities with power-law spectra.

Kilometer-scale irregularities with low density fluctuations are sufficient to give rise to the FPF of low orbit satellite beacons at 20, 40, and 54 MHz as illustrated in Figures 4*a*–*c*. Except in the case of 20-MHz signals, Gaussian type of irregularities cannot effectively cause the FPF of satellite signals.

Imagining that four polarimeters at Ascension Island are turned on to record low orbit satellite beacons of 20, 40, 54, and 136-MHz separately, one expects to see the FPF of 20-MHz signals for most of the time. Once, all the polarimeters have

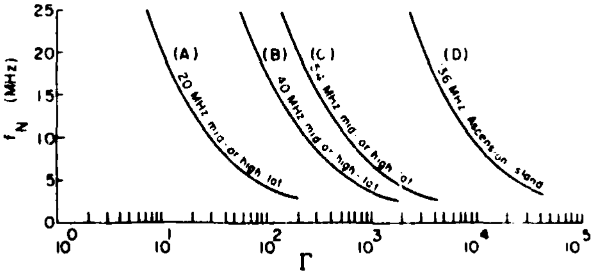

Fig. 4*c*. Γ versus f_N. Curves (A), (B), and (C) for 20, 40, and 54-MHz signals at middle or high latitudes. Curve (D) for 136-MHz signals at Ascension Island.

measured the FPF of 20- to 136-MHz signals, the 136-MHz FPF fades out first with the L band amplitude scintillation; the 54-MHz FPF and then, the 40-MHz FPF die out later on; even in the late phase of irregularities characterized by Gaussian spectra, the 20-MHz FPF can still persist for quite a while.

DISCUSSION

Single wave scattering from ionospheric irregularities has been used to study the FPF of satellite HF to VHF beacon signals in this paper. It shows that weak kilometer-scale density fluctuations are sufficient to cause the FPF of 20- to 54-MHz signals at locations not near the magnetic equator. Its use is questionable for its extension to cases wherein relatively strong density fluctuations are involved, such as the FPF of 41-MHz near the magnetic equator and that of 136-MHz near the anomaly region. The validity of weak (single) scattering theory as applied to the cases concerned is, therefore, briefly discussed as follows.

Let $W(\Phi)$ represent the power of satellite beacon signals scattered per unit solid angle, per unit incident power density, and per unit volume by irregularities; Φ is the angle between the direction of incidence and the direction of scattering. If the wavelength is much shorter than the irregularity scale sizes, the scattering has a sharply directed character, namely, most of the scattered power $W(\Phi)$ is restricted within a small solid angle Φ.

$$W(\Phi) = 8\pi r_e^{\,2} l^3 \langle(\Delta N)^2\rangle [1 + 4\pi^2 l^2 \Phi^2/\lambda^2]^{-2} \tag{8}$$

for scattering by irregularities with power law spectra [*Booker and Gordon*, 1950], and

$$W(\Phi) = \pi^{3/2} r_e^{\,2} l^3 \langle(\Delta N)^2\rangle \exp(-\pi^2 l^2 \Phi^2/\lambda^2) \tag{9}$$

for scattering by irregularities with Gaussian spectra [*Fejer*, 1953].

The power σ removed, per unit length, from a beam of unit power density, incident at a zenith angle γ on the irregularity layer (see Figure 2) is given by

$$\sigma = \int_0^{\pi} d\Phi 2\pi\Phi W(\Phi) \sec \chi \tag{10}$$

After the incident wave traverses the layer of irregularities, the power density of the unscattered wave becomes $P = P_0 \exp(-\int_0^D \sigma\, dz) = P_0 \exp(-\Sigma)$ where P_0 is the incident power density, D the layer thickness of irregularities, and $\Sigma = \int_0^D \sigma\, dz$.

Weak scattering requires that the unscattered power density should not be very much less than the incident power density, namely, Σ has to be small in comparison with 1.

$$\Sigma_p = 2 l r_e^{\,2} \lambda^2 N^2 \langle(\Delta N/N)^2\rangle D \sec \gamma \tag{11}$$

from (8) and (10) corresponding to power law type of irregularities; and

$$\Sigma_G = \pi^{1/2} l r_e^{\,2} \lambda^2 N^2 \langle(\Delta N/N)^2\rangle D \sec \gamma \tag{12}$$

from (9) and (10) corresponding to Gaussian type of irregularities. $\Sigma_p \sim 0.1$ if one substitutes into (11) those relevant ionospheric parameters required for causing appreciable FPF (i.e., $\langle|\Delta\Omega|^2\rangle^{1/2} = 0.1$) of 41-MHz signals at Huancayo as described in Figure 3. $\Sigma_p \sim 0.27$ corresponds to the ionospheric conditions for causing appreciable FPF of 136-MHz signals at Ascension Island. Weak scattering is, therefore, adequate for the description of FPF even in the presence of large density fluctuations. However, since Σ_p can be larger than 1 in cases involving large FPF (e.g., $\langle|\Delta\Omega|^2\rangle^{1/2} > 0.5$), it is interesting to estimate the effect of multiple scattering on the current analyses based on weak (single) scattering theory.

Multi-scattered waves have larger angles of deviation Φ than the singly scattered wave [*Fejer*, 1953]. Consequently, multiple scattering can result in larger phase shifts of ordinary and extraordinary modes. Since the induced Faraday rotation angle is proportional to the differential phase shift between the two modes, multiple scattering is essentially equivalent to the effect of increasing the density fluctuations $\langle(\Delta N/N)^2\rangle^{1/2}$ for causing large FPF *via single scattering. In other words,* $\langle|\Delta\Omega|^2\rangle^{1/2} \propto \langle(\Delta N/N)^2\rangle^{1/2}$ is not true for large FPF. $\langle(\Delta N/N)^2\rangle^{1/2}$, therefore, have been overestimated for large FPF, say, $\langle|\Delta\Omega|^2\rangle^{1/2} = 0.5$, on the basis of single scattering theory. The over-estimation is, however, not serious, since there is just a factor of 5 between the $\langle(\Delta N/N)^2\rangle^{1/2}$ for the appreciable FPF (i.e., $\langle|\Delta\Omega|^2\rangle^{1/2} = 0.1$) and that for large FPF (i.e., $\langle|\Delta\Omega|^2\rangle^{1/2} = 0.5$). No qualitative or significant quantitative changes are expected in the results presented in this paper after multiple scattering is taken into account.

Acknowledgments. The author wishes to thank J. Aarons, Santimay Basu, Sunanda Basu, S. Dasupta, J. A. Klobuchar, J. G. Moore, and E. J. Weber for useful discussions. This work was supported by AFGL contract F19628-80-C0016.

The Editor thanks J. P. McClure and K. Davies for their assistance in evaluating this paper.

REFERENCES

Aarons, J., H. E. Whitney, E. MacKenzie, and S. Basu, Microwave equatorial scintillation intensity during the current solar maximum, *Radio Sci.*, *16*, 939, 1981.

Basu, S., J. P. McClure, S. Basu, W. B. Hanson, and J. Aarons, Coordinated study of equatorial scintillation in situ and radar observations of nightime *F* region irregularities, *J. Geophys. Res.*, *85*, 5119, 1980*a*.

Basu, S., S. Basu, J. P. Mullen, and A. Bushby, Long-term 1.5-GHz amplitude scintillation measurements at the magnetic equator, *Geophys. Res. Lett.*, *7*, 259, 1980*b*.

Booker, H. G., and W. E. Gordon, A theory of radio scattering in the troposphere, *Proc. IRE*, *38*, 401, 1950.

Das Gupta, A., and A. Maitra, VHF satellite signal scintillation near the edge of the equatorial ionospheric irregularity belt, in *Low Latitude Aeronomical Processes*, edited by A. P. Mitra, p. 209, Pergamon, New York, 1980.

Fejer, J. A., The diffraction of waves in passing through an irregular refracting medium, *Proc. R. Soc. London Ser. A*, *220*, 455, 1953.

Kent, G. S., High frequency fading observed on the 40 Mc/s wave radiated from artificial satellite 1957 α, *J. Atmos. Terr. Phys.*, *16*, 10, 1959.

Klobuchar, J. A., and J. Aarons, Studies of equatorial irregularities patches using SIRIO VHF transmissions, *Alta Freq.*, *49*, 345, 1980.

Lee, M. C., A. Das Gupta, J. A. Klobuchar, S. Basu, and S. Basu, Depolarization of VHF geostationary satellite signals near the equatorial anomaly crests, *Radio Sci.*, *17*, in press, 1982.

McClure, J. P., Polarization measurements during scintillation of radio signals from satellites, *J. Geophys. Res.*, *69*, 1445, 1964.

Parthasarathy, R., and G. C. Reid, Signal strength recordings of the satellite 1958 δ2 (Sputnik III) at College, Alaska, *Proc. Inst. Radio Eng.*, *47*, 78, 1959.

Roger, R. S., The effect of scintillation on the polarization of satellite transmissions near 20 Mc/s, *J. Atmos. Terr. Phys.*, *27*, 335, 1965.

Yeh, K. C., and C. H. Liu, Wave propagation in a random medium with anisotropic background, *IEEE Trans. Antennas Propagat.*, *AP-15*, 539, 1967.

Yeh, K. C., and C. W. Swenson, The scintillation of radio signals from satellites, *J. Geophys. Res.*, *64*, 2281, 1959.

(Received September 9, 1981;
accepted September 30, 1981.)

Radio Science, Volume 17, Number 2, pages 399-409, March–April 1982

Depolarization of VHF geostationary satellite signals near the equatorial anomaly crests

M. C. Lee

Regis College Research Center, Weston, Massachusetts 02193

A. Das Gupta[1] *and J. A. Klobuchar*

Air Force Geophysics Laboratory, Hanscom Air Force Base, Massachusetts 01731

S. Basu and S. Basu

Emmanuel College, Boston, Massachusetts 02115

(Received June 24, 1981; revised September 9, 1981; accepted September 9, 1981.)

The nighttime polarization fluctuations of linearly polarized 136 MHz satellite signals received at Ascension Island, located near the southern crest of the equatorial anomaly, have been shown to be the manifestation of depolarization effect due to the diffractive scattering by small-scale (<200 m) density irregularities with power law spectra. The theory can explain its coexistence with *L* band scintillation. The absence of this phenomenon at equatorial locations off the anomaly crests is attributed to two factors: (1) the ambient plasma densities are relatively low, and (2) the propagation angles of satellite signals are more nearly perpendicular to the geomagnetic field.

1. INTRODUCTION

Intense and fast fluctuations in Faraday rotation angles have been observed from low-orbit satellite beacon signals transmitting on 20 MHz by *Parthasarathy and Reid* [1959], *Yeh and Swenson* [1959], and *Roger* [1965], on 40 MHz by *Kent* [1959], and on 54 MHz by *McClure* [1964]. *Kaushika and de Mendonca* [1974] observed that the Faraday rotation angle of the 137-MHz VHF signals from a geostationary satellite sometimes exhibited fluctuations of relatively slower periods, ranging from a few seconds to about an hour, when the local ionosonde showed spread *F* echoes at the low-altitude station of Sao Jose dos Campos (24°S dip), Brazil. Recently, *Klobuchar and Aarons* [1980] and *Das Gupta and Maitra* [1980] have reported intense and fast fluctuations of the Faraday rotation angles, in association with strong and fast amplitude scintillation, respectively, from Ascension Island (31°S dip) and Calcutta (32°N dip), both situated near the crests of the equatorial anomaly. Similar observations of fast fluctuations of Faraday rotation angles associated with strong, fast amplitude scintillation have been observed as far away from the equator as Delhi (44°N dip), India (Y. V. Somayajulu, private communication, 1981), but they have not been seen at Arequipa (7.9°S dip), Peru, located near the geomagnetic equator, nor have they been reported by *Yeh et al.* [1979*a*, *b*], in observations taken at Natal (7.9°S dip), Brazil.

In our observations from Ascension Island, we have noted the coexistence of Faraday polarization fluctuations with strong *L* band amplitude scintillation. They appear together during the postsunset hours and disappear at the same time near or after midnight. Saturated 136 MHz amplitude scintillations with a fast fading rate are always seen during the observations of Faraday polarization fluctuations. A sample record is shown in Figure 1. In an experiment at Ascension Island in December 1979, we separately recorded the amplitude of the left-hand circular and right-hand circular components of 136-MHz signals from the SIRIO geostationary satellite observed at 80° elevation transmitting nominally linearly polarized waves. We found that, during the times of strong, fast amplitude fading when polarization fluctuations occur, there was a loss of correlation of the opposite

---

[1] NAS/NRC Senior Resident Research Associate on leave from the University of Calcutta, India.

Paper number 1S1436.
0048-6604/82/0304-1436$01.00

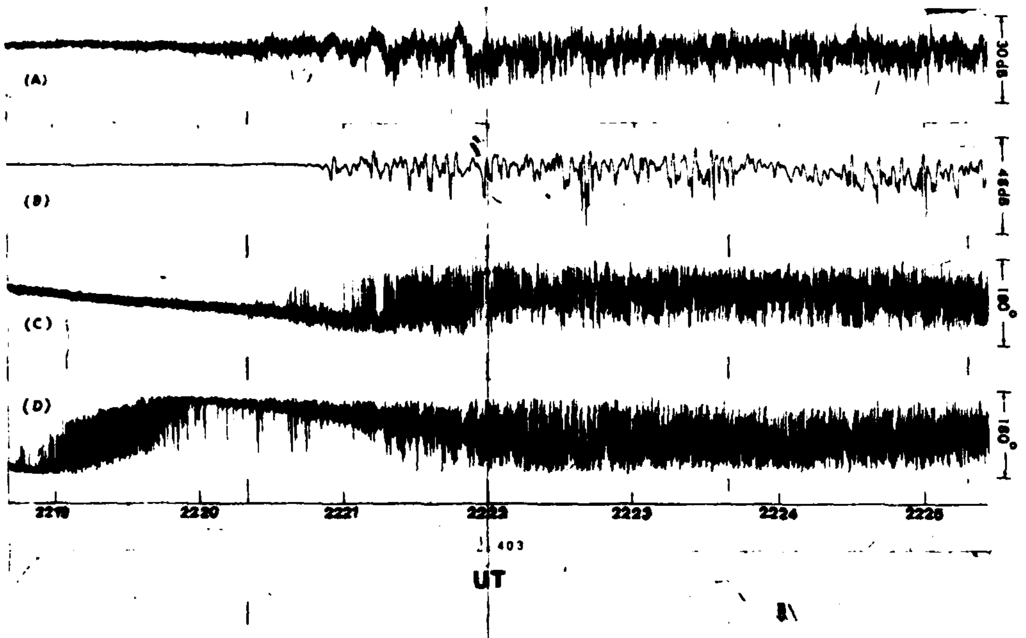

Fig. 1. Sample data of the geostationary satellite signals received at Ascension Island on January 2, 1980. Channels (A) and (B) show the amplitude scintillation of the 136-MHz signals transmitted from SIRIO and that of the *L* band (1.541 GHz) transmitted from MARISAT 1, respectively. Shown in channels (C) and (D) are the Faraday rotation measurements of 136-MHz signals in a ramp format with one channel displaced by 90° relative to the other. Intense and fast polarization fluctuations make the last two channels almost undistinguishable.

sense circularly polarized wave components (i.e., ordinary and extraordinary modes), indicating that, during those times, the concept of simple Faraday rotation was not valid at our observation frequency. It is the purpose of this paper to explain the reasons for those observations and to suggest why polarization fluctuations of VHF radio waves have not been observed very near the magnetic equator.

Ionospheric density irregularities are responsible for the irregular fluctuations in the Faraday rotation angles of satellite signals. We believe that the polarization fluctuations as shown in Figure 1 indicate the depolarization of linearly polarized transionospheric satellite signals. Two mechanisms have been suggested for interpreting the polarization fluctuations of HF satellite signals, specifically, at the frequency of 20 MHz. One concerned the effect of refraction imposed by large spatial inhomogeneities that give rise to large path separation of the ordinary and extraordinary modes, and, consequently, these two characteristic components of a linearly polarized signal can scintillate independently [*Roger*, 1965]. The other one proposed by *Yeh and Liu* [1967] is the process of wave scattering by density irregularities. Induced fluctuations in Faraday rotation angles due to this scattering may cause depolarization effect on the linearly polarized satellite signals.

In Roger's mechanism, it is the ray path separation of the two modes but not the density irregularities that is primarily investigated for the polarization fluctuations of satellite signals. The magnitude of path separation, which is large enough to decorrelate the two modes, is estimated roughly as $\Delta r = l/\langle(\Delta\phi)^2\rangle^{1/2}$, where l is the scale size of density irregularities, and $\langle(\Delta\phi)^2\rangle^{1/2}$ is the rms phase variation of the signals. Roger assumed that $l = 1$ km, $\langle(\Delta\phi)^2\rangle^{1/2} = 2$ rad for 20-MHz signals and obtained $\Delta r = 0.5$ km. The current in situ data, however, indicate a power law type of irregularity power spectrum encompassing scale sizes from meters to tens of kilometers. Moreover, Roger's mechanism cannot be used in the case of concern here to explain the close relationship of polarization fluctuations with *L* band scintillations and others.

By contrast, no significant path separation of ordinary and extraordinary modes is necessary in Yeh and Liu's mechanism. The wave scattering by density irregularities is considered to be the principal process responsible for the polarization fluctuations of satellite signals. Nevertheless, Yeh and Liu's theory cannot be extended to the case of VHF signals concerned, as explained later. As a matter of fact, density irregularities with Gaussian spectra, as assumed in Yeh and Liu's theory, turn out to be ineffective in causing the depolarization of VHF satellite signals.

Along the line of Yeh and Liu's approach, we show that the polarization fluctuations of linearly polarized 136-MHz satellite signals is the manifestation of depolarization effect due to the diffractive scattering by small-scale (<200 m) density irregularities with power law spectra. The absence of this phenomenon at equatorial locations off the anomaly crests is attributed to two factors: (1) the ambient plasma densities are relatively low, and (2) the propagation angles of satellite signals are more nearly perpendicular to the geomagnetic field. It can be shown that these two factors lead to the requirement of rather unrealistically large fractional fluctuations of ionization density for the depolarization of VHF signals to be seen at other equatorial locations.

This paper is organized as follows. The theory of single wave scattering by density irregularities is presented in section 2. In section 3, the variances of phase shift, field amplitude ratio, the Faraday rotation fluctuations, and the induced field component of transionospheric signals are formulated and evaluated for density irregularities of both power law and Gaussian types. Interpretation of observations and discussion are given in section 4.

2. TRANSIONOSPHERIC WAVE SCATTERING BY DENSITY IRREGULARITIES

For simplicity, density irregularities are modeled as a uniform mean square fractional fluctuations of ionization density $\langle(\Delta N/N)^2\rangle$ within a slab of ionization in the *F* region of mean density *N*. A linearly polarized wave transmitted from a geostationary satellite *S* is received on the ground at zenith angle χ.

The center of the coordinate system is chosen to be located at the geostationary satellite *S* as illustrated in Figure 2. In Figure 2, Z_0 represents the distance between the satellite and the receiver, *a* represents that between the satellite and the topside of density irregularities, *b* represents that between the receiver and the bottomside of density irregularities, *D* represents the thickness of the slab, and θ represents the propagation angle. The unscattered ray path within the density irregularities is *D* sec χ. In the case of concern here, Z_0 = 35,000 km, *b* = 500 km, *D* = 200 km, *a* = 34,300 km, θ = 52°, and χ = 10° are assumed.

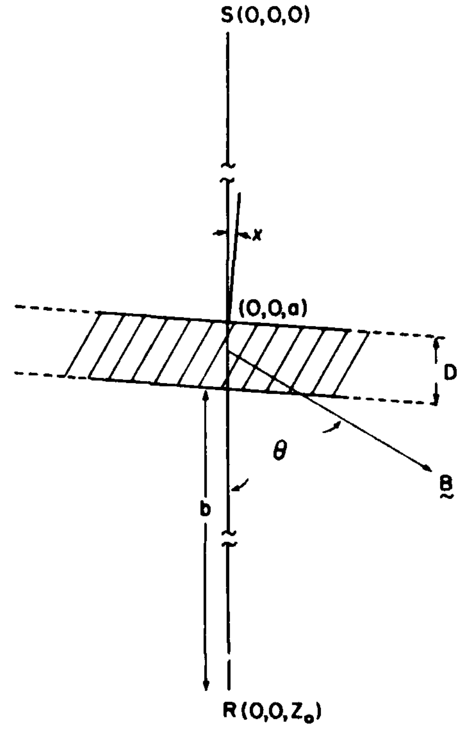

Fig. 2. Geometry of the transionospheric propagation concerned. The center of the coordinate system is located at the geostationary satellite *S*. Z_0 = 35,000 km, *a* = 34,300 km, *b* = 500 km, *D* = 200 km, θ = 52°, and χ = 10°.

For quasi-longitudinal propagation in the ionosphere, the refractive index of electromagnetic waves can be approximated as

$$n^2 \simeq 1 - \bar{f}_N^2(1 \pm \bar{\Omega}_L) \tag{1}$$

at frequencies large compared with the electron gyrofrequency, where $\bar{f}_N^2 = f_N^2/f^2$, i.e., the squared ratio of the ambient plasma frequency to the wave frequency, $\bar{\Omega} = \Omega/f$, i.e., the ratio of the electron gyrofrequency to the wave frequency, and $\bar{\Omega}_L = \bar{\Omega} \cos \theta$. The plus and minus signs in (1) refer, respectively, to the extraordinary and ordinary waves that are the

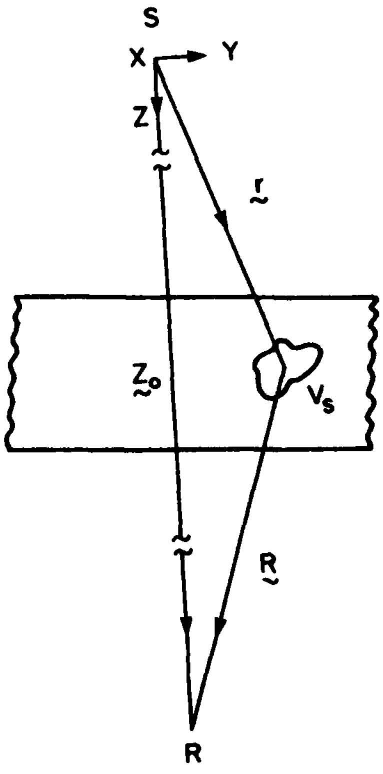

Fig. 3. Geometry of the wave scattering by density irregularities.

two characteristic modes of a linearly polarized wave in the ionosphere.

Since the refractive index n is defined as kc/ω, expression (1) can be written as

$$k_o = k(1 + \varepsilon) \qquad k_x = k(1 - \varepsilon)$$

as the wave numbers of the ordinary and extraordinary waves, respectively, where ε defined as $\bar{f}_N^2 \bar{\Omega}_L / 2(1 - \bar{f}_N^2)$ has a small value ($\sim 10^{-4}$) for the VHF propagation in the ionospheric F region, and $k = (\omega/c)(1 - \bar{f}_N^2)^{1/2}$ is the wave number in an isotropic medium (i.e., $\varepsilon = 0$).

In the far-field approximation, the wave fields of these two modes received at a distance of r from the source are given, respectively, by

$$\mathbf{E}_{io}(r) = (E/r)(\hat{x} + i\hat{y}) \exp [i(\omega t - k_o r)] \tag{2}$$

and

$$\mathbf{E}_{ix}(r) = (E/r)(\hat{x} - i\hat{y}) \exp [i(\omega t - k_x r)] \tag{3}$$

The summation of (2) and (3) yields the field of the linearly polarized spherical wave received at the same location. That is,

$$\mathbf{E}_R(r) = (2E/r)[\hat{x} \cos (\varepsilon k r) + \hat{y} \sin (\varepsilon k r)] \cdot \exp [i(\omega t - kr)] \tag{4}$$

showing that the polarization vector of the linearly polarized wave is rotated by an angle of $\varepsilon k r = (1/2)(k_o - k_x) r$ known as the Faraday rotation.

In the presence of density irregularities, namely $\bar{f}_N^2 = \langle \bar{f}_N^2 \rangle + \Delta \bar{f}_N^2$ (where $\langle \bar{f}_N^2 \rangle$ corresponds to the mean ionization density and $\Delta \bar{f}_N^2$ corresponds to the density irregularities), an additional change of Faraday rotation angle is introduced by wave scattering from density irregularities. Since satellite signals are received at a high elevation angle and the wavelength is assumed to be much shorter than the scale sizes of the most intense density irregularities concerned, wave reflection and the refraction due to horizontal stratification may be neglected. Only the forward scattering is considered here.

Let us first consider the scattering of ordinary waves by density irregularities. The incident electric field at scatterer V_s (see Figure 3) is represented by $\mathbf{E}_{io} = (\mathbf{E}_o/r) \exp [i(\omega t - k_o r)]$. For single forward scattering with small angles of deviation, the resultant field ($\mathbf{E}_s$) of the scattered waves received at $R(O, O, Z_0)$ is approximately given by

$$\mathbf{E}_s \simeq -\frac{Z_0}{4\pi} \frac{\omega^2}{c^2} \left\{ \left(\frac{\mathbf{E}_o}{Z_0} \right) \exp [i(\omega t - k_o Z_0)] \right\} \cdot \int_V d^3 r \, \frac{\Delta \bar{f}_N^2(r) \exp [-i k_o (r + R - Z_0)]}{Rr} \tag{5}$$

where V is the total volume of density irregularities. The total field of ordinary waves received at $R(O, O, Z_0)$ is composed of the unscattered and the scattered parts, i.e.,

$$\mathbf{E}_{RO}(\mathbf{Z}_0) \simeq [\mathbf{E}_o(\mathbf{Z}_0)/\mathbf{Z}_0] \exp [i(\omega t - k_o \mathbf{Z}_0)] \cdot \left\{ 1 - \frac{Z_0}{4\pi} \frac{\omega^2}{c^2} \cdot \int_V d^3 r \, \frac{\Delta \bar{f}_N^2(r) \exp [-i k_o (r + R - Z_0)]}{Rr} \right\} \tag{6}$$

If the scattered waves are weak compared with the unscattered waves, (6) may be also expressed as

$$\mathbf{E}_{RO}(\mathbf{Z}_0) \simeq \mathbf{E}_{io}(\mathbf{Z}_0) \exp (-i\phi_o) \tag{7}$$

This means that weak wave scattering by density irregularities introduces a complex phase shift into the original wave. Expanding the exponential function in

(7) to the first order of ϕ_o and equating it to (6) yields

$$\phi_o = -i\frac{Z_0}{4\pi}\frac{\omega^2}{c^2}\int_V d^3r\,\frac{\Delta\bar{f}_N^2(r)\exp\left[-ik_o(r + R - Z_0)\right]}{Rr} \tag{8}$$

The phase shift (ϕ_x) of extraordinary waves due to weak scattering by density irregularities can be similarly obtained as

$$\phi_x = -i\frac{Z_o}{4\pi}\frac{\omega^2}{c^2}\int_V d^3r\,\frac{\Delta\bar{f}_N^2(r)\exp\left[-ik_x(r + R - Z_0)\right]}{Rr} \tag{9}$$

The field of the linearly polarized waves received at $R(O, O, Z_0)$ is, therefore, given by

$$\mathbf{E}_R' = \mathbf{E}_{io}(\mathrm{Z}_0)\exp(-i\phi_x) + \mathbf{E}_{ix}(\mathrm{Z}_o)\exp(-i\phi_x) \tag{10}$$

which reduces to (4) in the absence of density irregularities.

A new xy coordinate plane is so chosen that the new x axis coincides with the polarization vector of the unscattered linearly polarized wave at $R(O, O, Z_0)$, i.e., (4) is expressed as

$$\mathbf{E}_R(\mathbf{Z}_0) = (2E/Z_0)\exp\left[i(\omega t - kZ_0)\right]\hat{x} \tag{11}$$

In this new system of coordinates, expression (10) assumes the following form

$$\mathbf{E}_R'(\mathbf{Z}_0) = (2E/Z_0)\exp\left[i(\omega t - kZ_0)\right]\exp\left[-i(\phi_o + \phi_x)/2\right]$$

$$\cdot\left[\hat{x}\cos\left(\frac{\phi_o - \phi_x}{2}\right) + \hat{y}\sin\left(\frac{\phi_o - \phi_x}{2}\right)\right] \tag{12}$$

a comparison between (11) and (12) shows that density irregularities cause phase shift, amplitude variation, and Faraday rotation of the linearly polarized waves. An induced field component along the y axis can be visualized to be associated with the induced Faraday rotation and to result in the depolarization of the linearly polarized waves. They are summarized as follows.

Phase shift

$$\Delta\phi = \mathrm{Re}\left(\frac{\phi_o + \phi_x}{2}\right) = -\frac{Z_0}{4\pi}\frac{\omega^2}{c^2}\int_V d^3r\,\frac{\Delta\bar{f}_N^2(r)}{Rr}$$

$$\cdot\cos\left[\epsilon k(r + R - Z_0)\right]\sin\left[k(r + R - Z_0)\right] \tag{13}$$

Amplitude variation

$$\ln\left(\frac{\mathbf{E}_R'}{\mathbf{E}_R}\right) = \mathrm{Im}\left(\frac{\phi_o + \phi_x}{2}\right) = \frac{Z_0}{4\pi}\frac{\omega^2}{c^2}\int_V d^3r\,\frac{\Delta\bar{f}_N^2(r)}{Rr}$$

$$\cdot\cos\left[\epsilon k(r + R - Z_0)\right]\cos\left[k(r + R - Z_0)\right] \tag{14}$$

Faraday rotation

$$\Delta\Omega = \frac{\phi_o - \phi_x}{2} = -\frac{Z_0}{4\pi}\frac{\omega^2}{c^2}\int_V d^3r\,\frac{\Delta\bar{f}_N^2(r)}{Rr}$$

$$\cdot\exp\left[-ik(r + R - Z_0)\right]\sin\left[\epsilon k(r + R - Z_0)\right] \tag{15}$$

Change of polarization vector

$$\frac{E_y}{E_x} = \tan\left(\frac{|\phi_o - \phi_x|}{2}\right) \simeq -\frac{Z_0}{4\pi}\frac{\omega^2}{c^2}\int_V d^3r\,\frac{\Delta\bar{f}_N^2(r)}{Rr}$$

$$\cdot\exp\left[-ik(r + R - Z_0)\right]\sin\left[\epsilon k(r + R - Z_0)\right] \tag{16}$$

for $|\phi_o - \phi_x| < 1$ rad. As noted in (8) and (9), ϕ_o and ϕ_x are in general complex, the real parts of which correspond to phase shifts, and the imaginary parts of which indicate changes in logarithmic amplitudes of wave fields. Therefore, the induced Faraday rotation angles ($\Delta\Omega$) and the polarization vector change (E_y/E_x) have complex values as expressed in (15) and (16), respectively. Physically, it means that $\Delta\Omega$ and (E_y/E_x) result from the differential phase shift (i.e., Re ($\phi_o - \phi_x$)) and the differential changes in logarithmic amplitudes of ordinary and extraordinary modes. The spatial averages of $\Delta\phi$, $\ln(\mathrm{E}_R'/E_R)$, $\Delta\Omega$, and (E_y/E_x) are zeroes; their variances, which are of main physical interest, are not, however.

3. VARIANCES OF $\Delta\phi$, $\ln(E_R'/E_R)$, $\Delta\Omega$, AND (E_y/E_x)

Let us first evaluate the induced Faraday rotation (15) or the change of polarization vector (16) for $|\phi_o - \phi_x| < 1$ rad, i.e.,

$$I = -\frac{Z_0}{4\pi}\frac{\omega^2}{c^2}\int_V d^3r\,\frac{\Delta\bar{f}_N^2(\mathbf{r})}{Rr}\cdot\exp\left[-ik(r + R - Z_0)\right]$$

$$\cdot\sin\left[\epsilon k(r + R - Z_0)\right] \tag{17}$$

In the system of coordinates (see Figure 3) used to evaluate (17), $r = (x^2 + y^2 + z^2)^{1/2}$ and $R = [(Z_0 - z)^2 + x^2 + y^2]^{1/2}$. Since Z_0, $Z_0 - z \gg (x^2 + y^2)^{1/2}$ is assumed, therefore, $r \simeq z + (x^2 + y^2)/2z$ and $R \simeq (Z_0 - z) + (x^2 + y^2)/2(Z_0 - z)$ lead to

$$r + R - Z_0 \simeq (x^2 + y^2)Z_0/2z(Z_0 - z) \tag{18}$$

Equation (18) is used to substitute for $(r + R - Z_0)$ in (17), and Rr in (17) is simply replaced by $z(Z_0 - z)$. These approximations are based on the assumption that the outer scale of density irregularities responsible for the depolarization effect is small compared with the distance between the altitude of density irregularities and the receiver. This assumption also assures forward scattering with small angles of deviation.

The variance of $\Delta\Omega$ or (E_y/E_x) over space can be, therefore, approximated as

$$\langle|I|^2\rangle = \frac{Z_0^2}{16\pi^2}\frac{\omega^2}{c^2}\int_V d^3r_1 \int_V d^3r_2 \frac{\langle(\Delta\bar{f}_N^2(\mathbf{r}_1))(\Delta\bar{f}_N^2(\mathbf{r}_2))^*\rangle}{z_1z_2(Z_0 - z_1)(Z_0 - z_2)}$$

$$\cdot \cos\left[\frac{k(x_1^2 + y_1^2)Z_0}{2z_1(Z_0 - z_1)} - \frac{k(x_2^2 + y_2^2)Z_0}{2z_2(Z_0 - z_2)}\right]$$

$$\cdot \sin\left[\frac{\varepsilon k(x_1^2 + y_1^2)Z_0}{2z_1(Z_0 - z_1)}\right] \sin\left[\frac{\varepsilon k(x_2^2 + y_2^2)Z_0}{2z_2(Z_0 - z_2)}\right] \tag{19}$$

where $\langle(\Delta f_N^2(\mathbf{r}_1))(f_N(\mathbf{r}_2))^*\rangle$ is the autocorrelation function of density irregularities. To carry out the integration in (19), it is convenient to make the following coordinate transformation:

$$\xi = x_1 - x_2 \qquad \eta = y_1 - y_2 \qquad \zeta = z_1 - z_2$$

$$X = 1/2(x_1 + x_2) \qquad Y = 1/2(y_1 + y_2) \tag{20}$$

$$Z = 1/2(z_1 + z_2)$$

Integrating (19) over X and Y from $-\infty$ to $+\infty$ leads to

$$\langle|I|^2\rangle = \frac{k^2}{16\pi(1 - \langle X\rangle)^2} - \int_a^{a+D\sec\chi} dZ \int_{-D\sec\chi}^{D\sec\chi} d\zeta$$

$$\cdot \int_{-\infty}^{\infty} d\eta \int_{-\infty}^{\infty} d\xi \langle(\Delta\bar{f}_N^2(\mathbf{r}_1))(\Delta\bar{f}_N(\mathbf{r}_2))^*\rangle$$

$$\cdot \{2G(0) \sin[G(0)(\xi^2 + \eta^2)] - G(\varepsilon) \sin[G(\varepsilon)(\xi^2 + \eta^2)]$$

$$- G(-\varepsilon) \sin[G(-\varepsilon)(\xi^2 + \eta^2)]\} \tag{21}$$

where

$$G(t) = Z_0k\{2\zeta(2Z - Z_0) + 4t[ZZ_0 - Z^2 - (\zeta/2)^2]\}^{-1}$$

where

$$t = 0, \pm\varepsilon$$

The form of the autocorrelation function has to be determined for the further evaluation of (21). Two types of power spectra are assumed for density irregularities: (1) power law type and (2) Gaussian type, which have been seen to be associated respectively with the early and the late phases of density irregularities in the observation of satellite scintillation [*Basu et al.*, 1980].

For simplicity, density irregularities are assumed to be generated by spatially homogeneous processes. The autocorrelation functions, therefore, depend only on the coordinate differences $\xi = x_1 - x_2$, $\eta = y_1 - y_2$, and $\zeta = z_1 - z_2$. Moreover, only statistically isotropic density irregularities are considered. In this case the autocorrelation functions are only functions of $(\xi^2 + \eta^2 + \zeta^2)^{1/2}$.

3.1. *Density irregularities with power law spectra*

For isotropic density irregularities of power law type, the autocorrelation function is taken to be

$$\langle(\Delta\bar{f}_N^2(\mathbf{r}_1))(\Delta\bar{f}_N^2(\mathbf{r}_2))^*\rangle = \langle(\Delta\bar{f}_N^2)^2\rangle$$

$$\cdot \exp[-l^{-1}(\xi^2 + \eta^2 + \zeta^2)^{1/2}]$$

where $\langle(\Delta\bar{f}_N^2)^2\rangle$ corresponds to the mean square fluctuations of ionization density and l is the correlation length. The integration in (21) over ξ and η can be conveniently evaluated with the transformation of (ξ, η) into the polar coordinates (t, ϕ), namely,

$$\int_{-\infty}^{\infty} d\xi \int_{-\infty}^{\infty} d\eta G \exp[-l^{-1}(\xi^2 + \eta^2 + \zeta^2)^{1/2}]$$

$$\cdot \sin[G(\xi^2 + \eta^2)] = \pi \int_0^{\infty} dt$$

$$\cdot \exp[-l^{-1}(|G|)^{1/2}(t + |G|\zeta^2)^{1/2}] \sin(t) \tag{22}$$

*Although the general analytic solution of (22) can*not be obtained, an approximate form that is appropriate for the case of $kl \gg 1$ is shown in the appendix to be

$$\int_0^{\infty} dt \exp[-l^{-1}(|G|)^{-1/2}(t + |G|\zeta^2)^{1/2}] \sin(t)$$

$$\simeq \exp(-l^{-1}|\zeta|)(1 - l^{-1}|G|^{-1/2}) \tag{23}$$

Since $Gl^2 \sim kl \gg 1$, the second term in parentheses of (23) is less than the first one by an order of $(kl)^{1/2}$. However, if the second term in (23) is neglected, the integration in (21) over ξ and η cancels and thus $\langle|I|^2\rangle = 0$. This indicates that the depolarization of satellite signals, if any, is a second order ionospheric effect.

Using the identity of integration given by (23), (21) yields

$$\langle|I|^2\rangle = \frac{k^2\langle(\Delta\bar{f}_N^2)^2\rangle}{16(1 - \langle\bar{f}_N^2\rangle)^2} \int_a^{a+D\sec\chi} dZ$$

$$\cdot \int_{-D\sec\chi}^{D\sec\chi} d\zeta\, l^{-1}[2(2Z - Z_0)/Z_0k]^{1/2}$$

$$\cdot \{|l|\zeta + \varepsilon 2(ZZ_0 - Z^2 - (\zeta/2)^2)/(2Z - Z_0)|]^{1/2}$$

$$+ \{|\zeta - \varepsilon 2(ZZ_0 - Z^2 - (\zeta/2)^2)/(2Z - Z_0)|\}^{1/2} - 2|\zeta|^{1/2}\} \exp(-l^{-1}|\zeta|) \tag{24}$$

It is quite clear in (24) that $\langle |I|^2 \rangle = 0$ if the terms involving ε in the integrand are much less than ζ. We assume that $\varepsilon 2[ZZ_0 - Z^2 - (\zeta/2)^2]/(2Z - Z_0) \sim 2\varepsilon d$ is comparable to $\zeta \leq l$, where d is the distance between the receiver and the mean altitude of density irregularities. Then

$$l \sim 2\varepsilon d = 2d(f_N/f)^2(\Omega/f)(1 - f_N^2/f^2)^{-1} \cos\theta \tag{25}$$

can be used to determine the outer scales of irregularities that are responsible for the 136-MHz Faraday polarization fluctuations.

Neglecting ζ in the braces of (24) and replacing the limits of integration $\pm D \sec\chi$ by $\pm\infty$, since $D \gg l$, we can easily carry out the integration of (24) over ζ and obtain

$$\langle |I|^2 \rangle = \frac{k^2 \langle (\Delta \bar{f}_N^2)^2 \rangle}{2(1 - \langle \bar{f}_N^2 \rangle)^2} \int_a^{a+D\sec\chi} dZ \left[\frac{\varepsilon Z(Z_0 - Z)}{Z_0 K} \right]^{1/2} \tag{26}$$

Because $a \gg D$, the integral in (26) can be simply represented by the product of the interval of integration and the integrand wherein all Z's are replaced by Z_m, where Z_m is the distance between the satellite and the mean altitude of density irregularities. We finally obtain the following result

$$\langle |I|^2 \rangle = \frac{k \langle (\Delta N/N)^2 \rangle (\bar{f}_N^2)^2}{2(1 - \langle \bar{f}_N^2 \rangle)^2} (\varepsilon k d)^{1/2} D \sec\chi \tag{27}$$

During the current solar maximum period, total electron contents (TEC's) as large as 100 units (1 unit $= 10^{16}$ m^{-2}) have been frequently measured at Ascension Island. This indicates a large F_2 maximum plasma density N_m (= 100 units/250 km ~ 4.1 × 10^{12} m^{-3}, where 250 km is the assumed slab thickness of the ionosphere), namely, a large ambient plasma frequency (~18 MHz). Ionograms obtained at Ascension Island from airborne measurements also indicate large f_0F_2 between 16 MHz and 20 MHz (E. Weber and J. Moore, private communication, 1981).

If f_N = 18 MHz, Ω_e = 1.5 MHz, and d = 600 km are used in (25), the polarization fluctuations of 136-MHz satellite signals received at Ascension Island ($\theta = 52°$) turns out to be caused by density irregularities with an 'outer scale length' of <200 m. It is interesting to note that recent rocket [*Rino et al.*, 1981] and satellite in situ [*Basu et al.*, 1981] measurements at F region heights show a break in spectral slope generally around several hundred meters. Therefore, the outer scale length so termed here may refer to that portion of irregularity power spectrum.

At Ascension Island, the Faraday rotation measurements were made at an elevation angle of 80°, namely, $\chi = 10°$ in (27). If the thickness of density irregularities is taken to be 200 km and the ambient plasma frequency is taken to be 18 MHz, (27) shows that 0.33% rms fractional fluctuations of ionization density can cause appreciable polarization fluctuations of 136-MHz signals, i.e., $\langle |I|^2 \rangle^{1/2} = 0.1$, and that 1.65% ionization density fluctuations may result in large depolarization effect, i.e., $\langle |I|^2 \rangle^{1/2} = 0.5$.

Similarly, $\langle (\Delta\phi)^2 \rangle$ and $\langle 1n(E_y/E_x)^2 \rangle$ can be derived from (13) and (14), respectively, as

$$\langle (\Delta\phi)^2 \rangle = 4r_e^2 N^2 \langle (\Delta N/N)^2 \rangle \lambda^2 l D \sec\chi / (1 - \langle \bar{f}_N^2 \rangle) \tag{28}$$

and

$$\langle |1n(E_R'/E_R)|^2 \rangle = \frac{\langle (\Delta f_N^2)^2 \rangle}{(1 - \langle f_N^2 \rangle)^2} Dk \sec\chi (kd)^{1/2} \tag{29}$$

where l represents the scale sizes of density irregularities that cause the phase fluctuation of VHF satellite signals, r_e(~2.82 × 10^{-15}m) is the classical electron radius, and λ the wavelength of VHF signals.

3.2. *Density irregularities with Gaussian spectra*

$$\langle (\Delta \bar{f}_N^2(\mathbf{r}_1))(\Delta \bar{f}_N^2(\mathbf{r}_2))^* \rangle = \langle (\Delta \bar{f}_N^2) \rangle \exp[-l^{-2}(\xi^2 + \eta^2 + \zeta^2)] \tag{30}$$

is the autocorrelation function used to represent the density irregularities with Gaussian spectra. In situ measurements indicate that Gaussian spectra are associated with the late developed phase of irregularities with a correlation length of 1 km [*Basu et al.*, 1980]. Therefore, l is taken to be 1 km in (30). Substituting (30) into (21) and integrating with respect to ξ and η, we obtain

$$\langle |I|^2 \rangle = \frac{k^2 \langle (\Delta \bar{f}_N^2)^2 \rangle}{16(1 - \langle \bar{f}_N^2 \rangle)^2} \int_a^{a+D\sec\chi} dZ \int_{-\infty}^{\infty} d\zeta \cdot \exp(-l^{-2}\zeta^2)\{2F(0) - F(\varepsilon) - F(-\varepsilon)\} \tag{31}$$

where

$$F(t) = \left\{ 1 + \left[\frac{2\zeta(2Z - Z_0)}{Z_0 k l^2} \pm 4t \frac{(ZZ_0 - Z^2 - (\zeta/2))}{Z_0 k l^2} \right]^2 \right\}^{-1} \tag{32}$$

where $t = 0, \pm\varepsilon$.

Since $2\zeta(2Z - Z_0)/Z_0kl^2$ is of the order of $2/kl \sim 7.0 \times 10^{-4}$ and $4\varepsilon Z(Z_0 - Z)/Zkl^2$ of the order of $4\varepsilon d/kl^2 \sim 5.0 \times 10^{-5}$, $F(0)$ and $F(\pm\varepsilon)$ have the general expression of $(1 + \delta^2)^{-1}$ with $\delta \ll 1$, which can be well approximated as $(1 - \delta^2)$. The expression in the braces of (31) is, consequently, simplified to be $2[4\varepsilon Z(Z_0 - Z)/Zkl^2]^2$. Straightforward integration of (31) over ζ and Z leads to

$$\langle|I|^2\rangle = 4^{-1}\pi^{1/2}\langle(\Delta N/N)^2\rangle(1 - \bar{f}_N^2)^{-2}(\bar{f}_N^2)^4(\bar{\Omega})^2d^2l^{-3}D \cdot \sec\chi \cos^2\theta \tag{33}$$

Substituting into (33) the same parameters as used in the case of power law type irregularities shows that unrealistically large density fluctuations are required for causing the polarization fluctuations of 136-MHz signals, namely $\langle(\Delta N/N)^2\rangle^{1/2} = 843\%$ for $\langle|I|^2\rangle^{1/2} = 0.1$ and $\langle(\Delta N/N)^2\rangle^{1/2} = 4215\%$ for $\langle|I|^2\rangle = 0.5$. A reasonable ionospheric density depletion $(\langle(\Delta N/N)^2\rangle^{1/2})$ with Gaussian spectra is about a few percentage points, say 5%. According to (33), the ambient plasma frequency must be as high as 65 MHz so that the Gaussian type of irregularities is able to cause the appreciable depolarization (i.e., $\langle|I|^2\rangle^{1/2} = 0.1$) of 136-MHz signals. Such a high ionospheric plasma frequency is, however, unrealistic under the normal conditions.

The derivation of $\langle(\Delta\phi)^2\rangle$ and $\langle \ln(E_R'/E_R)^2\rangle$ can be easily done in the case of Gaussian type irregularities. They are

$$\langle(\Delta\phi)^2\rangle = \frac{\pi^{1/2}l\lambda^2r_e^2N^2\langle(\Delta N/N)^2\rangle}{4(1 - \langle\bar{f}_N^2\rangle)^2}\{J(0) + J(1)\} \tag{34}$$

and

$$\langle|\ln(E_R'/E_R)|^2\rangle = \frac{\pi^{1/2}l\lambda^2r_e^2N^2\langle(\Delta N/N)^2\rangle}{4(1 - \langle\bar{f}_N^2\rangle)^2}\{J(0) - J(1)\} \tag{35}$$

where

$$J(x) = \int_a^{a+D\sec\chi} dz\{1 + |x4Z(Z_0 - Z)/Z_0kl^2|^2\}^{-1}$$

where

$$x = 0, 1$$

Equations (34) and (35) can be reduced, respectively, from the (26) and (27) of *Yeh and Liu* [1967], wherein $J(\varepsilon)$ reduces to $J(0)$, since $\varepsilon \sim 10^{-4}$ for the 136-MHz wave propagation.

4. DISCUSSION AND CONCLUSION

In this paper, wave scattering by density irregularities with power law spectra has been proposed as the process for causing the intense and fast fluctuations of the SIRIO 136-MHz signals received at Ascension Island. Based on the above analysis, the following things can be understood: (1) the nature of density irregularities that result in the polarization fluctuations of satellite signals, (2) why the polarization fluctuations of 136-MHz signals has a close correlation with the occurrence of the L band scintillation, (3) why the polarization fluctuations of 136-MHz signals has only been seen at locations near the equatorial anomaly crests, and (4) the frequency limit beyond which density irregularities will not affect significantly the polarization vector of satellite signals.

We have already shown that the polarization fluctuations of 136-MHz satellite signals result from the wave scattering by density irregularities whose power spectra exhibit power law rather than Gaussian distribution. In situ measurements [*Basu et al.*, 1980] show that, while density irregularities have relatively flat power spectra obeying a power law slope in their early phase, density irregularities in their late phase are seen to have a sharp slope essentially characteristic of a Gaussian distribution. This indicates that, during the change of power spectra from power law to Gaussian types, relatively short-scale (say, less than 1 km) density irregularities decay. As shown in (25), the polarization fluctuations of 136-MHz satellite signals turns out to be caused by those short-scale density irregularities with an outer scale length less than about 200 m.

Density irregularities with scale lengths of a few hundreds of meters are responsible for the L band scintillation. Therefore, the L band scintillation is not expected during the late phase of density irregularities characterized with Gaussian spectra, indicating the decaying of short-scale density irregularities. Observations of the 257-MHz scintillation at Ascension Island in the presence and absence of the L band scintillation, indeed, indicate the characteristic increasing of the correlation lengths of the 257-MHz signals [*Basu et al.*, 1981]. That both the L band scintillation and the polarization fluctuations of the 136-MHz signals are caused by relatively short-scale density irregularities is likely to account for the coexistence of these two phenomena.

The ambient plasma density (N) and the propagation angle (θ) are the most location dependent param-

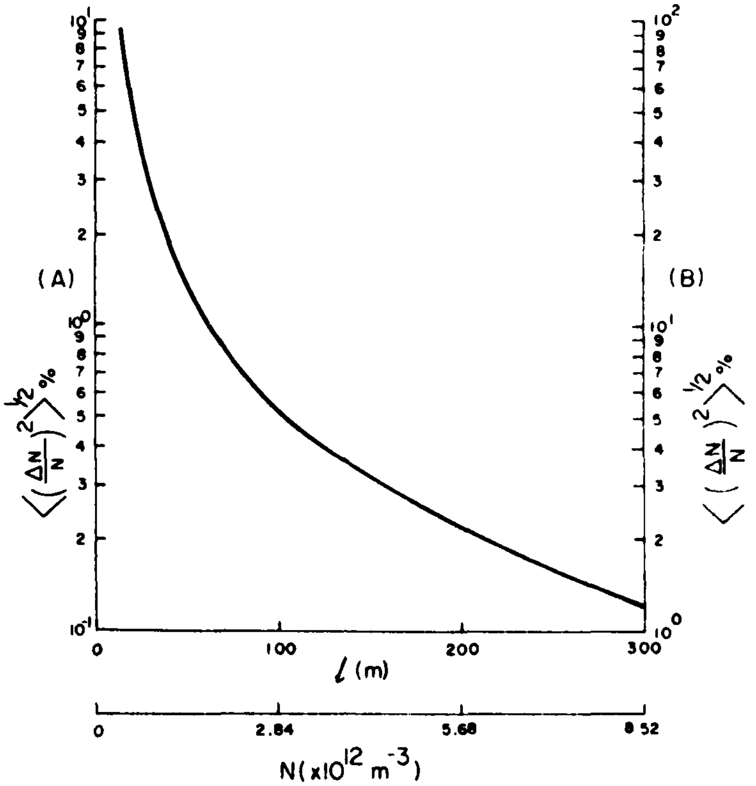

Fig. 4. Fractional fluctuations ($\langle(\Delta N/N)^2\rangle^{1/2}$) of the plasma density N versus the outer scale lengths l of density irregularities or the ambient plasma density N, as required to cause the polarization fluctuations of 136-MHz satellite signals at Ascension Island. Scale (A) for $\langle|l|^2\rangle^{1/2} = 0.1$, scale (B) for $\langle|l|^2\rangle^{1/2} = 1.0$.

eters. As mentioned before, the ambient plasma density measured at locations near the Appleton anomaly crests may be larger than those at other equatorial locations by a factor of 2–4 during the solar maximum period [*Rastogi*, 1966; *Aarons et al.*, 1981]. Let us look at the possibility of observing the 136-MHz polarization fluctuations near the magnetic equator, e.g., Natal, Brazil (geographic coordinate 5.85°S, 35.23°W, 9.6°S dip).

The propagation angle at Natal is about 80° (cf. 52° at Ascension Island). If the ambient plasma frequency at Natal is taken to be 10 MHz (cf. 18 MHz at Ascension Island), $f_N^2 \cos\theta$ obtained at Natal is less than that at Ascension Island by a factor of 11.5. Therefore, according to $l \propto f_N^2 \cos\theta$ in (25), the density irregularities causing the polarization fluctuations of 136 MHz signals at Natal, if any, have an outer scale shorter than 20 m (cf. 200 m at Ascension Island). On the other hand, since the ratio of $f_N^5(\cos\theta)^{1/2}$ at Natal to that at Ascension Island is 35.6, $\langle|l|^2\rangle \propto \langle(\Delta N/N)^2\rangle f_N^5(\cos\theta)^{1/2}$ in (27) requires that $\langle(\Delta N/N)^2\rangle$ at Natal be larger than that at Ascension Island by 35.6 times to cause the same level of 136-MHz polarization fluctuations, i.e., $\langle(\Delta N/N)^2\rangle^{1/2} = 10\%$ for $\langle|l|^2\rangle^{1/2} = 0.5$. This example shows clearly that low ambient plasma densities and large propagation angles at the magnetic equator make it impossible to observe the polarization fluctuations of 136-MHz satellite signals at equatorial locations except near the anomaly crests.

In (25), $l \propto f_N^2 \propto N$ indicates that, in an environment of high ambient plasma density, density irregularities with longer scale lengths can also be involved in producing the polarization fluctuations of satellite signals. Eliminating f_N from (25) and (27) yields

$$\langle(\Delta N/N)^2\rangle^{1/2} = C\langle|l|^2\rangle^{1/2} l^{-5/4} \tag{36}$$

where $C = 4(\Omega/f)dk^{-1/4}(D \sec\chi)^{-1/2} \cos\theta \sim 16.5$ for the assumed ionospheric condition at Ascension

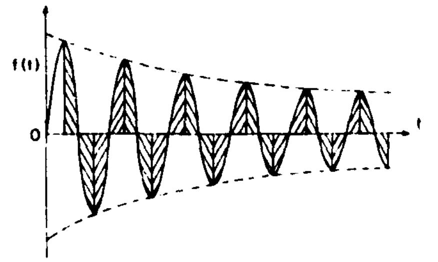

Fig. 5. Plot of $f(t) = \exp[-l^{-1}(|G|)^{-1/2}(t + |G|\zeta^2)^{1/2}] \sin(t)$ for $Gl^2 \gg 1$. The unhatched area represents approximately the integration of $f(t)$ over t from 0 to ∞.

Island: $d = 600$ km, $D = 200$ km, $\Omega = 1.5$ MHz, $f = 136$ MHz, $\theta = 52°$, and $\chi = 10°$. It is clear from the plotting of (36) in Figure 4 that, in the presence of density irregularities, high ambient plasma density provides the favorable environment for the VHF polarization fluctuations to occur. This may explain why the polarization fluctuations of 136-MHz signals has been frequently observed at Ascension Island during the current solar maximum period.

For illustration, the frequency limit beyond which density irregularities cannot cause significant polarization fluctuations of satellite signals is loosely defined as that at which $\langle |J|^2 \rangle^{1/2} = 0.1$ requires 1% of density fluctuation under the aforesaid ionospheric condition. This frequency is determined as 235 MHz from (27), and the outer scale length of density irregularities is determined as 28 m from (25).

It should be pointed out that the theory of single wave scattering discussed in this paper cannot explain the observed saturated amplitude scintillations of 136-MHz signals. It is well known that the saturation of VHF amplitude scintillation is attributed to multiple scattering. Therefore, deductions of the present theory for the amplitude scintillation may not be true. The validity of single scatter approximation as applied to the problem of polarization fluctuations can be justified [*Lee*, 1981]. Multiple scattering is expected to give rise to the saturation of polarization fluctuations in the presence of large density irregularities. However, the effect of multiple scattering does not impose significant quantitative changes in the results derived from the theory of single wave scattering. Simple analyses presented in this paper turn out to be adequate for the understanding of the 136-MHz polarization fluctuations and associated phenomena.

APPENDIX: AN APPROXIMATE SOLUTION OF $\int_0^\infty dt \exp[-l^{-1}(|G|)^{-1/2}(t + |G|\zeta^2)^{1/2}] \sin(t)$

For $Gl^2 \sim kl$, which is much greater than one as assumed, the integrand in (22), i.e., $\exp[-l^{-1}(|G|)^{-1/2}(t + |G|\zeta^2)^{1/2}] \sin(t)$ can oscillate for many cycles before it dies out. As illustrated in Figure 5, only the unhatched area does not vanish and represent the approximate integration of (22).

Integration by parts twice in (22) yields

$$\int_0^\infty dt \exp[-l^{-1}(|G|)^{-1/2}(t + |G|\zeta^2)^{1/2}] \sin(t)$$

$$= \exp(-l^{-1}|\zeta|) - \int_0^\infty dt \sin(t) \frac{\partial^2}{\partial t^2}$$

$$\cdot \exp[-l^{-1}(|G|)^{-1/2}(t + |G|\zeta^2)^{1/2}] \tag{A1}$$

Since $\exp[-l^{-1}(|G|)^{-1/2}(t + |G|\zeta^2)^{1/2}]$ vanishes effectively at distances of the order of the correlation length, the double differentiation of $\exp[-l^{-1}(|G|)^{-1/2}(t + |G|\zeta^2)^{1/2}]$ with respect to t may be approximated by

$$\max\{\exp[-l^{-1}(|G|)^{-1/2}(t + |G|\zeta^2)^{1/2}]\}/G^2l^4$$

$$= \exp(-l^{-1}|\zeta|)/G^2l^4 \tag{A2}$$

Sin (t) in (A1) may be represented approximately by the parabolic function $(t)^{1/2}$. The integral in (A1) can therefore be approximated as

$$\int_0^\infty dt \sin(t) \frac{\partial^2}{\partial t^2} \exp[-l^{-1}(|G|)^{-1/2}(t + |G|\zeta^2)^{1/2}]$$

$$\simeq |G|l^2 \cdot (|G|l^2)^{1/2} \cdot \exp(-l^{-1}|\zeta|)/G^2l^4$$

$$= \exp(-l^{-1}|\zeta|)/(|G|)^{1/2}l \tag{A3}$$

Substituting (A3) into (A1) leads to the approximate form of (22) for $Gl^2 \gg 1$, namely,

$$\int_0^\infty dt \sin(t) \exp[-l^{-1}(|G|)^{-1/2}[t + |G|\zeta^2]^{1/2}$$

$$\simeq \exp(-l^{-1}|\zeta|)[1 - l^{-1}(|G|)^{-1/2}] \tag{A4}$$

Indeed, that the approximate form in (A4) carries the right functional relationship with G and l is confirmed by the exact integration in (22) for $\zeta = 0$.

Acknowledgments. Comments from C. L. Rino and K. C. Yeh are greatly appreciated. This work was supported by AFGL contract F19628-80-C-0016 at Regis College Research Center and by AFGL contract F19628-81-K-0011 at Emmanuel College. This

paper was presented at the AGU 1981 spring meeting held at Baltimore, Maryland, May 25–29, 1981.

REFERENCES

Aarons, J., H. E. Whitney, E. Mackenzie, and S. Basu (1981), Microwave equatorial scintillation intensity during the current solar maximum, *Radio Sci.*, *16*, 939–945.

Basu, S., J. P. McClure, S. Basu, W. B. Hanson, and J. Aarons (1980), Coordinated study of equatorial scintillation and in situ and radar observations of nighttime *F* region irregularities, *J. Geophys. Res.*, *85*, 5119–5130.

Basu, S., S. Basu, J. P. McClure, W. B. Hanson, and H. E. Whitney (1981), Spatially and temporally co-located measurements of GHz/VHF scintillation and in situ irregularities spectra near Ascension Island (abstract), *Eos Trans. AGU*, *62*, 347.

Das Gupta, A., and A. Maitra (1980), VHF satellite signal scintillation near the edge of the equatorial ionospheric irregularity belt, *Adv. Space Explor.*, *8*, 209–212.

Kaushika, N. D., and F. de Mendonca (1974), Nighttime fluctuations (scintillations) in Faraday rotation angle of VHF signals from geostationary satellites, *Planet. Space Sci.*, *22*, 1331–1334.

Kent, G. S. (1959), High frequency fading observed on the 40 Mc/s wave radiated from artificial satellite 1957α, *J. Atmos. Terr. Phys.*, *16*, 10–20.

Klobuchar, J. A., and J. Aarons (1980), Studies of equatorial irregularity patches using SIRIO VHF transmissions, *Alta Freq.*, *49*, 345–349.

Lee, M. C. (1981), Faraday polarization fluctuations of transionospheric propagation, *J. Geophys. Res.*, *86*, in press.

McClure, J. P. (1964), Polarization measurements during scintillation of radio signals from satellites, *J. Geophys. Res.*, *69*, 1445–1447.

Parthasarathy R., and G. C. Reid (1959), Signal strength recordings of the satellite 1958 δ2 (Sputnik III) at College, Alaska, *Proc. Inst. Radio. Eng.*, *47*, 78–79.

Rastogi, R. G. (1966), The equatorial anomaly in the *F*2 region of the ionosphere, *J. Inst. Telecommun. Eng. New Delhi*, *12*, 245–256.

Rino, C. L., R. T. Tsunoda, J. Petriceks, R. C. Livingston, M. C. Kelley, and K. D. Baker (1981), Simultaneous rocket-borne beacon and in situ measurements of equatorial spread *F*. Intermediate wavelength results, *J. Geophys. Res.*, *86*, 2411–2420.

Roger, R. S. (1965), The effect of scintillations on the polarization of satellite transmissions near 20 Mc/s, *J. Atmos. Terr. Phys.*, *27*, 335–348.

Yeh, K. C., and C. H. Liu (1967), Wave propagation in a random medium with anisotropic background, *IEEE Trans. Antennas Propag.*, *AP-15*, 539–542.

Yeh, K. C., and C. W. Swenson (1959), The scintillation of radio signals from satellites, *J. Geophys. Res.*, *64*, 2281–2286.

Yeh, K. C., H. Soicher, and C. H. Liu (1979*a*), Observations of equatorial ionospheric bubbles by the radio propagation method, *J. Geophys. Res.*, *84*, 6589–6594.

Yeh, K. C., H. Soicher, C. H. Liu, and E. Bonelli (1979*b*), Ionospheric bubbles observed by the Faraday rotation method at Natal, Brazil, *Geophys. Res. Lett.*, *6*, 473–475.

Reprinted from Nature, Vol. 298, No. 5872, pp. 354-357, 22 July 1982
Macmillan Journals Ltd, 1982

VHF Faraday polarization fluctuations and strong *L*-band amplitude scintillations near Appleton anomaly crests

A. DasGupta*, M. C. Lee† & J. A. Klobuchar*

* Air Force Geophysics Laboratory, Hanscom AFB,
Massachusetts 01731, USA
† Regis College Research Center, Weston,
Massachusetts 02139, USA

The Faraday rotation angle of a linearly polarized transionospheric very high frequency (VHF) signal near the crests of the Appleton anomaly, around the recent solar maximum period, often exhibits fast and intense fluctuations, when the amplitude of the signal shows saturated and very fast scintillations[1,2]. These fluctuations usually occur during the post-sunset hours and decay around midnight. The occurrence pattern has been found to be similar to that of microwave amplitude scintillations at *L*-band. We present here certain observed characteristics of the fast polarization fluctuations and report the results of an experiment, which shows that there is a loss of correlation between fadings on the two circularly polarized component modes of the signal during the periods of VHF polarization fluctuations. Hence, the usual concept of Faraday rotation is no longer valid during these times. The above features are discussed in terms of our present knowledge of small scale irregularity structures in the equatorial ionosphere.

Equatorial ionospheric irregularities have been extensively investigated during the past decade by techniques such as rocket and satellite *in situ* measurements, radar, airglow and propagation effects on transionospheric signals[3]. It has been shown that the plumes of equatorial irregularities associated with depletions in background electron content can be studied in a very simple and inexpensive manner from simultaneous measurements of amplitude scintillations and Faraday rotation of a VHF signal propagating through the ionosphere[4,5]. While the occurrence of depletions of the integrated electron content is commonly observed with Faraday rotation records obtained near the magnetic equator[6,7], a new feature, fast and intense fluctuations of the Faraday rotation angle, has recently been reported from stations situated near the crests of the Appleton anomaly[1,2], a region characterized by severe amplitude scintillations during solar maximum years[8,9]. Polarization fluctuations of 136-MHz signals have been observed at Ascension Island (31°S dip), which is situated close to the southern crest of the equatorial anomaly in the African zone, and at Calcutta (32°N dip) and Ahmedabad[10] (34°N dip) near the northern crest of the anomaly in the Indian sector. These have sometimes been observed even at Delhi (40°N dip) (Y. V. Somayajulu, personal communication) near the northern edge of the anomaly, but no such phenomenon has been observed at Arequipa (9°S dip), Peru or at Natal (10°S dip), Brazil which are close to the magnetic equator. Kaushika and deMendonca[11] possibly observed the same type of fluctuations in the polarization records of 137-MHz signals recorded at Sao Paulo (26° S dip) which is also situated near the crest of the anomaly, but they had no amplitude scintillation measurements. In their attempt to associate the fluctuations with atmospheric gravity waves, they were concerned with slower fluctuations of period 2 min and longer.

Figure 1 shows a typical polarimeter record obtained during post-sunset hours at Ascension Island (7.9° S, 14.4° W, 31° S dip). The channel at the top is the amplitude of the 136-MHz transmission from the geostationary satellite SIRIO (15° W) and the two bottom channels are the Faraday polarization angle of the signal with one shifted from the other by 90°. The polarization fluctuations are often too intense to render the Faraday data useful. The station also recorded signals from the satellite Marisat (also at 15° W) at 257 MHz and 1.54 GHz for amplitude scintillation measurements. The sub-ionospheric points of the two satellites are essentially identical. The third channel from the top shows amplitude scintillations of the 1.54-GHz signal. Polarization fluctuations are found when the amplitude of the VHF signal shows saturated and very fast scintillations, which generally occur during the pre-midnight hours. We have found during more than 2 yr of observations around the recent solar maximum period that the polarization fluctuations coexist with intense *L*-band scintillations at 1.54 GHz. During the post-midnight period polarization fluctuations decay, even though VHF amplitude scintillation remains saturated, but with slower fading rates.

The change in fading rates of VHF amplitude scintillations, with and without polarization fluctuations, is clearly evident in the power spectra of 136-MHz scintillation measurements as presented in Fig. 2*a* and *b* respectively. The corresponding power spectra obtained at 257 MHz and 1.54 GHz are also shown. The approximate corner frequencies of the power spectra are indicated by arrows. The corner frequency of a power spectrum gives a measure of the fading rate, a higher corner frequency corresponding to a faster fading rate. In the present case, a lowering of the corner frequency is obvious in the late phase, as shown in Fig. 2*b*, when no polarization fluctuations are observed.

Power spectrum analysis of scintillation measurements is generally used to obtain information on the characteristics of

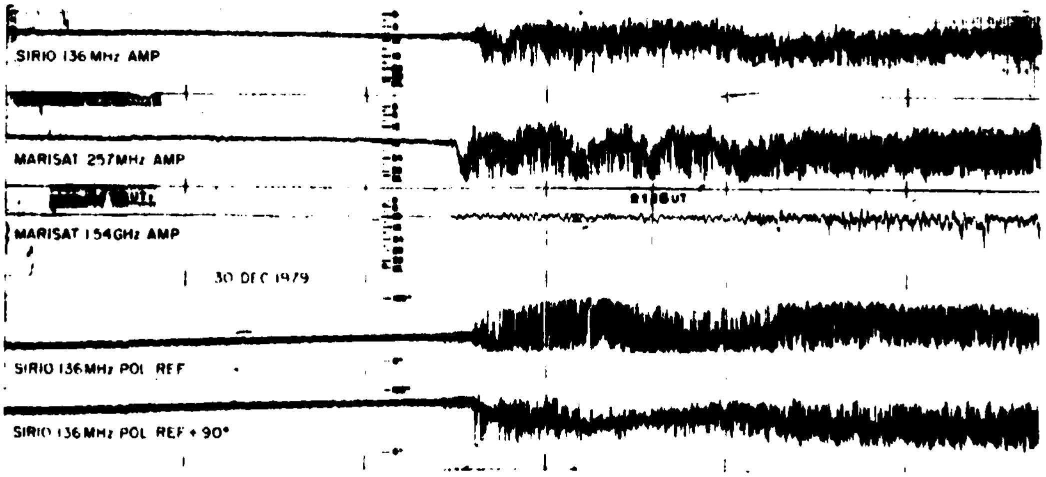

Fig. 1 Sample records of satellite signals obtained at Ascension Island. Time marks shown are in UT. Local time corresponds to UT − 1 h.

the ionospheric irregularities responsible for scintillations. However, the interpretations of the power spectrum in conditions of weak and strong scintillations involve different scattering mechanisms by the ionospheric irregularities. According to the theory of radiowave propagation, for weak scintillation conditions, the amplitude fading rate of a transionospheric signal from a geostationary satellite is proportional to v/l_F, where v is the drift velocity of the irregularities and l_F the Fresnel dimension[6]. Because $l_F \propto \sqrt{\lambda}$ (where λ is the radiowave length), the fading rate should increase with observing frequency in weak scatter conditions. In contrast, in the case of severe scintillations, the wave propagation has to be considered in the framework of multiple scatter theory and the recorded scintillation data pertain to the ground diffraction pattern, which cannot be related to the irregularity pattern in the ionosphere in a simple manner[12]. The fading rate, in severe scintillation conditions, is inversely related to the autocorrelation distance of the ground pattern. The autocorrelation interval is determined by the drift velocity as well as by the strength of scattering. As the strength of scattering (in other words, scintillation index) increases, the autocorrelation distance decreases[13], and an increase in the fading rate is observed[14]. The scintillation index is usually inversely related to the observing frequency. Thus, in the case of severe scintillations, with an increase of the observing frequency the autocorrelation distance should increase and hence, a slowing down of the amplitude fading rate occurs.

In the equatorial region amplitude scintillations observed at 136 MHz and 250 MHz are usually severe (saturated or near saturated) for most of the time the phenomena are observed. Near the crests of the Appleton anomaly, severe scintillations in excess of 20 dB are quite frequent even at *L*-band (such as 1.54-GHz observations at Ascension Island) during the pre-midnight hours, particularly around the recent solar maximum[8]. The power spectra depicted in Fig. 2 are representative of scintillations observed at the corresponding frequencies in the developed and late phases of equatorial night-time ionospheric irregularities respectively.

During an intensive campaign of measurements in December 1979, in order to investigate the nature of fast polarization fluctuations, the left and right circular components of the 136-MHz signal were recorded separately in addition to the routine observations. The data were recorded on a magnetic tape in analog form, which was digitized at an 18 samples s^{-1} rate for later analysis. The cross-correlation between the amplitude fadings of the two component modes was computed over 3-min intervals. The scintillation index S_4 (refs 15, 16), which is a measure of the r.m.s. amplitude fluctuations about the mean level, is also computed for each 3 min interval at different observing frequencies. Figure 3 shows the variation of the cross-correlation coefficient between the amplitude fadings of the two circularly polarized component waves at 136 MHz with changes in the scintillation index S_4 observed at 1.54 GHz.

The correlation coefficient decreases as S_4 increases and attains low values (<0.2) when S_4 is 0.5 or more. The intervals with $S_4 > 0.5$ at 1.54 GHz generally exhibit fast polarization fluctuations at 136 MHz. In other words, the two circularly polarized components undergo quasi-independent fluctuations when strong *L*-band and polarization fluctuations are obtained. If the two modes become quasi-independent, the usual concept of Faraday rotation breaks down. The close correlation of occurrence of 136-MHz polarization fluctuations and the 1.54-GHz scintillation, clearly seen in Fig. 3, implies that either irregularities of nearly the same scale size are responsible for the two phenomena or that the irregularities causing the two phenomena coexist in the ionosphere.

Lee *et al.*[17] have shown that ionospheric power law density irregularities with an outer scale size in the range 50–200 m are responsible for the 136-MHz polarization fluctuations. Faraday polarization fluctuations result from differential phase shift and the differential change in the logarithmic amplitude of the two circularly polarized modes introduced by wave scattering from these short-scale density irregularities. The theory shows that a deviation of ~1–2% in a high ambient ionization density, say, not less than 3.0×10^{12} m^{-3}, corresponding to a plasma frequency of over 15 MHz, is required to provide a favourable environment for the 136-MHz fluctuations to occur. When the r.m.s. differential phase departure exceeds ~0.5 rad, the two circularly polarized modes are expected to become practically uncorrelated. Scintillations at 1.54 GHz are most effectively produced by irregularities with scale sizes of a few hundred metres (~300 m in the present case), which are of the same order as the Fresnel zone dimension. Both the 136-MHz

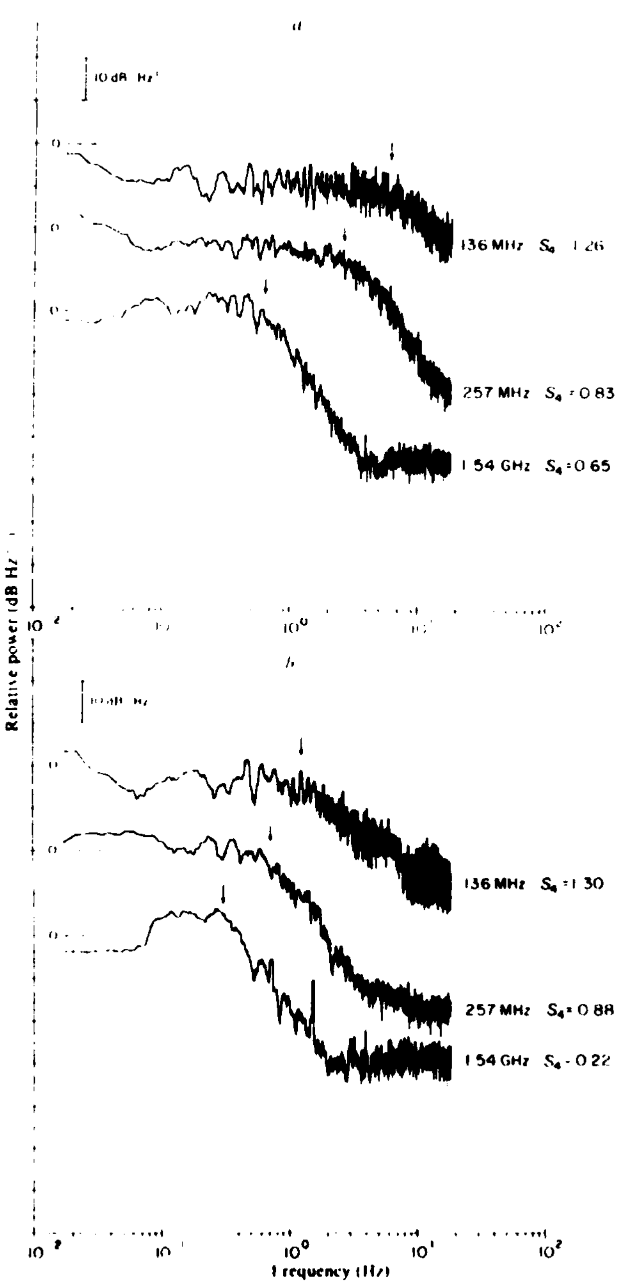

Fig. 2 Power spectra of amplitude scintillations at different frequencies for a 3-min sample centred on the time indicated. *a*, 21 h 46 min 30 s UT; Faraday polarization channels show intense and rapid fluctuations during this period. *b*, 22 h 34 min 30 s UT; no fast polarization fluctuation was observed during this period. The approximate corner frequencies are given by arrows.

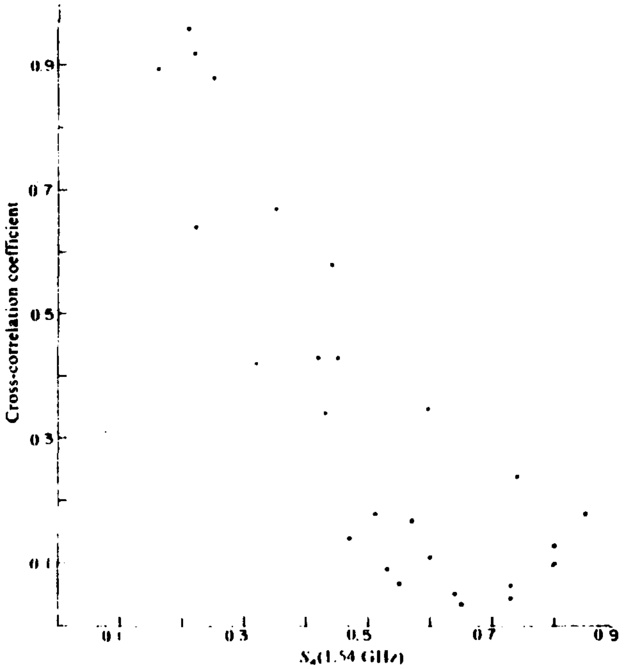

Fig. 3 Variation of cross-correlation coefficients of the fluctuations of the two opposite circularly polarized components of the 136-MHz signal with the amplitude scintillation index S_4 at 1.54 GHz. The intervals $S_4 > 0.5$ correspond to intense and fast Faraday polarization fluctuations.

polarization fluctuations and the 1.54-GHz scintillations involve density irregularities of a few hundred metres scale size. If the irregularity power spectrum follows a power law, with diminishing spectral density at shorter scale lengths, and if the overall strength of the irregularities is high enough to have spectral density in the 50–200 m scale size range sufficient to cause polarization fluctuations at 136 MHz, it is implied that irregularities at a ≥300 m scale size range will also have enough spectral power to produce appreciable amplitude scintillations at 1.54 GHz. Thus, the presence of fast polarization fluctuations at 136 MHz may be taken as an indication of the possible scintillations at *L*-band and lower frequencies. The reverse may not, however, always be true.

From multi-technique observations Basu *et al.*[18] have reported that, while during the pre-midnight period the power spectra of equatorial irregularities follow a power law, during post-midnight hours the overall strength of the irregularities is eroded and there is a transition to a quasi-gaussian type of spectrum indicating the decay of shorter-scale (typically <1 km) irregularities. As the 1.54-GHz scintillation became weak, with the decay of short-scale density irregularities, the two circularly polarized modes were seen to have high cross-correlation coefficients, reflecting no, or very small, polarization fluctuations.

Except in the HF band (for example, 20 MHz), the polarization fluctuations of satellite signals cannot be effectively caused by irregularities with quasi-gaussian spectra[19]. Near the Appleton anomaly crests, in solar maximum conditions, the ambient ionization density (n) is very high and the high level persists during the evening hours. As a result, the absolute value of the irregularity intensity (Δn) is also very high in the anomaly region[8]. In contrast, in regions near the magnetic equator, the relatively small n and Δn and the relatively large angles of propagation with respect to the geomagnetic field make it impossible to give rise to significant polarization fluctuations of 136-MHz signals[17].

We thank S. Basu, Sunanda Basu and C. L. Rino for discussions. The work at the Regis College Research Center was supported by AFGL contract F19628-80-C-0016. A.D.G is a NRC-NAS Senior Resident Research Associate on leave from the University of Calcutta, India.

Received 3 March; accepted 20 May 1982

1. Klobuchar, J. A. & Aarons, J. *Alt. Frequenza* **49**, 345–349 (1980).
2. DasGupta, A. & Maitra, A. *Adv. Space Expl.* (COSPAR Ser.) **8**, 209–212 (1980).
3. Basu, S. & Basu, S. *J. atmos. terr. Phys.* **43**, 473–489 (1981).
4. Klobuchar, J. A., Aarons, J., Weber, E., Lucena, L. & Mendillo, M. *Paper* G.4 (Radio Science Meeting, US National URSI, Boulder, Colorado, 1978).
5. Yeh, K. C., Soicher, H., Liu, C. H. & Bonelli, E. *Geophys. Res. Lett.* **6**, 473–475 (1979).
6. Yeh, K. C., Soicher, H. & Liu, C. H. *J. geophys. Res.* **84**, 6589–6594 (1979).
7. DasGupta, A., Aarons, J., Klobuchar, J. A., Basu, S. & Bushby, A. *Geophys. Res. Lett.* **9**, 147–150 (1982).
8. Aarons, A., Whitney, H. E., MacKenzie, E. & Basu, S. *Radio Sci.* **16**, 939–945 (1981).
9. DasGupta, A., Maitra, A. & Basu, S. *Radio Sci.* **16**, 1455–1458 (1981).
10. Deshpande, M. R. *et al. Curr. Sci.* **50**, 221–222 (1981).
11. Kaushika, N. D. & de Mendonca, F. *Planet. Space Sci.* **22**, 1331–1334 (1974).
12. Yeh, K. C., Liu, C. H. & Youakim, M. Y. *Radio Sci.* **10**, 97–106 (1975).
13. Rino, C. L. & Owen, J. *Radio Sci.* **16**, 31–33 (1981).
14. Umeki, R., Liu, C. H. & Yeh, K. C. *J. geophys. Res.* **82**, 2752–2760 (1977).
15. Briggs, B. H. & Parkin, I. A. *J. atmos. terr. Phys.* **25**, 339–365 (1963).
16. Whitney, H. E., Aarons, J. & Malik, C. *Planet. Space Sci.* **17**, 1069–1073 (1969).
17. Lee, M. C., DasGupta, A., Klobuchar, J. A., Basu, S. & Basu, S. *Radio Sci.* **17**, 399–409 (1982).
18. Basu, S., McClure, J. P., Basu, S., Hanson, W. B. & Aarons, J. *J. geophys. Res.* **85**, 5119–5130 (1980).
19. Lee, M. C. *J. geophys. Res.* **87**, 751–755 (1982).

7-83

DTIC